Summer 8-10-2019

A Quantitative Study of Drug Recrystallization in Drug-In-Adhesive Transdermal Patches Using Vibrational Spectroscopy

Yi Li

A QUANTITATIVE STUDY OF DRUG RECRYSTALLIZATION IN DRUG-IN-ADHESIVE TRANSDERMAL PATCHES USING VIBRATIONAL SPECTROSCOPY

A Dissertation

Submitted to the Graduate School of Pharmaceutical Sciences

Duquesne University

In partial fulfillment of the requirements for

the degree of Doctor of Philosophy

By

Yi Li

May 2019

A QUANTITATIVE STUDY OF DRUG RECRYSTALLIZATION IN DRUG-IN-ADHESIVE TRANSDERMAL PATCHES USING VIBRATIONAL SPECTROSCOPY

By

Yi Li

Approved May 16th, 2019

Carl A. Anderson, Ph.D.
Associate Professor of Pharmaceutics
Division Head, Pharmaceutical, Administrative & Social Sciences
(Committee Chair)

James K. Drennen, III, Ph.D.
Associate Professor of Pharmaceutics
Associate Dean for Research and Graduate Programs
(Committee Member)

Peter L.D. Wildfong, Ph.D.
Associate Professor of Pharmaceutics
Graduate School of Pharmaceutical Sciences
(Committee Member)

Ira S. Buckner, Ph.D.
Associate Professor of Pharmaceutics
Graduate School of Pharmaceutical Sciences
(Committee Member)

Lisa C. Rohan, Ph.D.
Professor of Pharmaceutical Sciences
University of Pittsburgh
(Committee Member)

J. Douglas Bricker, Ph.D.

Dean, School of Pharmacy and Graduate School of Pharmaceutical Sciences

ABSTRACT

A QUANTITATIVE STUDY OF DRUG RECRYSTALLIZATION IN DRUG-IN-ADHESIVE (DIA) TRANSDERMAL PATCHES USING VIBRATIONAL SPECTROSCOPY

By

Yi Li

May 2019

Dissertation supervised by Carl A. Anderson, Ph.D.

Drug-in-adhesive (DIA) transdermal patches are an important type of transdermal drug delivery system (TDDS). The drugs used in the DIA system are frequently present in metastable forms, such as amorphous solids or supercooled liquids. These drug states are thermodynamically unstable and tend to undergo phase changes, such as recrystallization, throughout the lifetime of transdermal products. Recrystallization of the active pharmaceutical ingredient (API) can adversely affect the efficacy (slowdowns of drug release due to low solubility) of transdermal products. The role that the extent of crystallization plays in determining the physiochemical properties and release behavior of DIA patches has not been fully investigated. There are no widely accepted methods for determining crystalline content of API(s) in DIA systems. The DIA patches have distinct mechanical and optical properties that render the existing solid-state phase quantification approaches insufficient. Calibration standards for phase quantification are typically

prepared by thoroughly mixing crystalline API powders with the amorphous API created in solid dispersions. The tackiness of the adhesive polymers prevents the blending and mixing of the crystalline and amorphous API. Moreover, the detection limit of the conventional reference method, X-ray diffraction (XRD), is higher for a semi-solid thin film than for a solid mixture. This dissertation introduces a systematic approach to quantify the crystalline content of the API in DIA systems. This approach uses a novel method of preparing calibration standards and a spectroscopic method to reliably predict crystalline content in DIA patches.

Understanding the variability of the sample system is vital to developing an analytical method. Calibration samples must have the variability of the target samples for which the method is designed. The DIA calibration samples were prepared by spiking patches with crystalline drug to mimic the crystalline distributions in authentically recrystallized patches. The physical stability of the spiked crystals was determined by tracking the size of crystals using microscopic imaging. The uniformity of the spiked crystal was determined at the scale or size at which the spectroscopic tools were used to examine the authentically recrystallized samples.

Spectroscopic tools, including Raman spectroscopy and near-infrared spectroscopy (NIRS), can be used to determine the crystallinity of drug in transdermal patches rapidly and non-destructively with a limit of detection comparable to that of the conventional solid-state characterization techniques. Analytical sensitivity, selectivity, and depth of penetration were determined for the DIA system using the spectroscopic systems. Comparisons between the sensitivity of the developed spectroscopic methods and an XRD method were acquired to determine the sensitivity of the techniques at low levels of crystallinity.

Spectral data collected on calibration samples via NIRS and Raman were related to the crystalline content according to a design of experiment that minimized the correlation between the

crystalline and the solvated API. The spectral features and diagnostic measures of two independent test sets were compared to demonstrate the validity of the calibration samples. One test set was made by spiking crystalline API and the other was made by recrystallization. The suitability of the spectroscopic methods was validated using the fit-for-purpose concept. Sample specific multivariate detection limit (MDL) was calculated. It accounts for variance associated with all possible steps involved in the method development and model testing. An accuracy profile derived from bias and intermediate precision related the method performance to the predefined acceptance criteria.

Development of reliable solid-state quantification methods is a critical component in understanding crystallization processes. In this work, the effect of environmental variability on the physical stability of the DIA patches was evaluated using changing temperature and humidity conditions. The recrystallization profile determined from the Raman method was fit to a Weibull function to generate the recrystallization rate constants. The impacts of temperature and humidity on crystallization rates were used to determine the roles that thermodynamic and kinetic driving forces play in determining the physical stability.

In summary, sample representativeness, analytical capability, and method suitability were integrated to form a systematic approach for crystallization quantification. The results of this work demonstrated that a reliable crystalline content quantification method can be developed using NIR spectroscopy and Raman spectroscopy for DIA transdermal patch delivery systems. The quantitative spectroscopic methods are potential tools for supporting formulation development and physical stability evaluation of transdermal products in the pharmaceutical industry.

DEDICATION

This dissertation is dedicated to my family and friends.

ACKNOWLEDGEMENT

I would like to thank Duquesne Graduate School of Pharmaceutical Sciences and everyone who has contributed to this project.

I cannot overstate my gratitude to my advisor, Dr. Carl Anderson, who has believed in me, enlightened me and guided me since the first day I entered Duquesne. I am grateful for his generosity in sharing his knowledge and expertise as well as his passion for research, which has enabled me to indulge in the pure joy of conducting scientific research. I would also like to express my deep appreciation to Dr. Drennen, my co-advisor, for his vital support and assistance in pursuit of my goals. The unique opportunities he created helped me discover my potential and build confidence.

I would like to convey my special thanks to Dr. Wildfong, who always made time when I needed advice for this project. I would also like to thank Dr. Buckner for his special contributions in every committee meeting and department seminar and I would like to express my gratitude to my Dr. Lisa Rohan (University of Pittsburgh), for her valuable inputs as my committee member.

I am indebted to Dr. Benoît Igne, who has inspired me in so many ways. I can always count on him for practical suggestions and sincere advice. I extend my thanks to my graduate colleagues Ryanne Palermo, Dr. Robert Bondi, and Dr. Sameer Talwar, for their effort in bridging the gap between my undergraduate and graduate studies. I would like to thank Dr. Anik Alam, Shikar Mohan, Dr. Hanzhou Feng, Nayeem Hossain, and Dr. Douglas Steinbach for providing me with important encouragement and support throughout the duration of this dissertation project. I also had the pleasure of working with Yuxiang Zhao, Natasha Velez Rodriguez, Suyang Wu, Adam Rish, Jacob Guess and Eric Pierce in B11.

I am most grateful to my parents who have always trusted me and lent me unconditional support, both financially and emotionally. I cannot thank them enough for helping me overcome moments of self-doubt and hardships. I would like to thank Andrew Wilson, my fiancé, for his love and patience during the last two years of graduate school. He has helped me to find strength and motivation to complete this work.

TABLE OF CONTENTS

LIST OF TABLES

Page

LIST OF FIGURES

Page

LIST OF ABBREVIATIONS

ANOVA	Analysis of Variance
API	Active Pharmaceutical Ingredient
ASD	Amorphous Solid Dispersion
BTEM	Band Target Entropy Minimization
CLS	Classical Least Squares
CQA	Critical Quality Attribute
DIA	Drug-in-Adhesive
DSC	Differential Scanning Calorimetry
DVS	Dynamic Vapor Sorption
DOE	Design of Experiment
DS	Degree of supersaturation
FOM	Figure of Merit
FTIR	Fourier Transform Infrared
ICH	International Conference on Harmonization
IUPAC	International Union of Pure and Applied Chemistry
JMA	Johnson, Mehl, and Avrami Equations
KJMA	Kolmogorov-Johnson-Mehl-Avrami
LOD	Limit of Detection
LV	Latent Variable
MCR	Multivariate Curve Resolution
MDL	Multivariate Detection Limit
NAS	Net Analyte Signal
NIR	Near-Infrared
PAT	Process Analytical Technology
PCA	Principal Component Analysis
PET	Polyethylene

PIB	Polyisobutylene
PLS	Partial Least Regression
PSA	Pressure Sensitive Adhesive
PTFE	Polytetrafluoroethylene
PVP	Polyvinylpyrrolidone
QbD	Quality by Design
RMSE	Root Mean Squared Error
RMSEC	Root Mean Squared Error of Calibration
RMSECV	Root Mean Squared Error of Cross-Validation
RMSEP	Root Mean Squared Error of Prediction
RSD	Relative Standard Deviation
SEP	Standard Error of Prediction
S/N	Signal-to-Noise Ratio (S/N)
SNV	Standard Normal Variate
SSNMR	Solid-State Nuclear Magnetic Resonance
T_g	Glass Transition Temperature
TDDS	Transdermal Drug Delivery System
USP	United States Pharmacopeia
UV-VIS	Ultraviolet - Visible Spectroscopy
XRD	X-Ray Diffraction

Chapter 1 : Introduction

1.1 Statement of the Problem

Transdermal patches represent a convenient alternative to oral delivery.[1] They are placed on the skin to deliver drugs percutaneously into the bloodstream. The benefits of transdermal patches include minimization of first-pass effects, avoidance of gastrointestinal irritation and reduced frequency of dosage.[2-3] Drug-in-adhesive (DIA) and drug-in-reservoir patches are the two main designs of passive transdermal drug delivery systems.[3-4] DIA patches are more frequently manufactured than reservoir-type patches because of their simple and flexible design, which is well suited for mass production. A DIA patch typically contains a liner, a backing, an adhesive and a drug. Delivery of drugs through the skin is challenging because of the excellent barrier properties of the stratum corneum.[5] Improved permeation and release profiles are reported for DIA systems that contain maximized drug concentrations.[6] The increase in the delivery of drug across the skin increases proportionally with the degree of supersaturation of the drug in the polymer.[7] The system becomes supersaturated when the degree of supersaturation is above the solubility of drug in the polymer. Supersaturation can be achieved by combining the drug and the adhesive into a solid dispersion via melt-quenching or solvent casting. However, drugs formed through these manufacturing routes either become amorphous solids or supercooled liquids that readily crystallize over the shelf-life of transdermal products.

The instability of solid-state drugs is one of the most critical problems found in transdermal patches.[8] Crystallization of drugs in supersaturated transdermal patches has significant impacts on patch release. When the amorphous drug recrystallizes from its supersaturated solution, any solute removed from the solution is replenished by the solid phase via dissolution into the solvent. However, the crystallized drug is far less likely to re-dissolve into the solid matrix. The

recrystallized drug remains sequestered in the crystalline phase and cannot be delivered; whereas the drug is delivered from the polymer where the concentration of the drug goes down. Therefore, a lower amount of free drug molecules remain available for absorption as a result of crystallization.[9] The drug must remain dissolved in its amorphous state (or solvated state) to achieve rapid release from the transdermal patch. Crystallization in most transdermal patches is incomplete, meaning that after some time there will be coexisting crystalline and dissolved drug. As a result, significant batch-to-batch variation of the release and physiochemical properties may occur. Meanwhile, patches with increased crystalline content are more likely to undergo hazing, cracking and even sliding from the skin.[10] Furthermore, the adhesive properties of DIA patches, such as viscoelasticity and tack, may also be adversely affected.[11] In addition, factors which affect the kinetics of recrystallization, such as temperature and humidity, can further reduce the physical stability of DIA patches and lead to drug crystallization during storage. Crystal formation testing is mandatory for new transdermal drug product applications. The patch stability study must be conducted over at least six months under varying environmental conditions to study the effect of temperature and humidity on the physical stability of patches. Therefore, the changes in transdermal performance due to the solid-state instability not only pose risks to the patients but also exacerbate the formulation and regulatory burdens.

Reliable analytical techniques are required for stability monitoring of transdermal patches throughout their shelf-life. The degree of crystallinity of drugs can be used as a critical quality attribute (CQA) for non-crystalline DIA formulation development and stability studies. Characterizing the solid-state kinetics of the recrystallization process of amorphous drugs in DIA patches allows establishment of mathematical relationships between physical stability and factors (formulation and process) that give more insight into transformation mechanisms.[12]

Recrystallization kinetics cannot be accomplished without an analytical method that enables the fast and reliable determination of crystalline content. Traditional solid-state quantification techniques have many problems. The quantification of solid phases via differential scanning calorimetry (DSC) requires optimization of parameters (heating rate and heating cycle) and minimizing the influence of the thermal history of samples. The technique also suffers from the problem of sub-sampling. The capabilities of both methods for quantifying crystalline drug in DIA system is adversely influenced by their limit of detection (LOD).

The use of spectroscopic tools may alleviate the above-mentioned problems. Raman spectroscopy and near-infrared spectroscopy (NIRS) have the potential to non-destructively and rapidly determine the crystallinity of drugs in DIA transdermal patches without sample preparation. Differentiation of amorphous and crystalline phases by molecular spectroscopic techniques relies on the absorption and scattering of light at particular wavelengths that reflect molecular vibrations and interactions among functional groups.[13] The spectral differences between amorphous and crystalline materials are caused by the presence or absence of spatial order and long-range translation symmetry.[14] Both NIR and Raman have demonstrated good sensitivity and selectivity to crystalline phases in the presence of amorphous materials.[15] Quantification of low concentrations (<2%) of crystalline drug for pharmaceutical tablets has been achieved previously.[16-18] However, the suitability of Raman and NIRS to determine crystalline drug content in transdermal patches has not been demonstrated.

There are no validated approaches for determining crystalline drug content in DIA systems. The European Medicines Agency (EMA) recommends using microscopic and photometric counts as quantitative measures of crystallization in transdermal products.[19] Compared to the typical solid dosage forms of tablets and powders, DIA patches present distinct mechanical and optical

properties that render the existing solid-state phase quantification approaches insufficient. The general procedure of developing a quantitative spectroscopic method for crystallinity determination includes calibration design, preparation of calibration samples, sample measurements, reference analysis, and multivariate regression analysis. Preparing calibration samples to reach the desired levels of crystallinity is challenging. Calibration samples for phase quantification are usually prepared by thoroughly mixing separately prepared crystalline and amorphous phases into a homogeneous blend.[20] The strong tackiness of the adhesive polymers prevent the blending and mixing of the DIA components. Even if mixing the drug with the adhesive is feasible, the energy imparted during the mixing procedures potentially induces polymorphic transformation and changes in crystallinity. As a result, the assumed crystallinity may no longer be accurate. Alternatively, NIR chemical imaging and Raman mapping can provide spatial information of the amorphous and crystalline components at the surface of transdermal patches without the need to make calibration samples.[21-22] However, determining crystallinity via classifying and counting pixels assigned to crystalline and amorphous components is considered semi-quantitative at best. The quantitative capabilities of these methods are still under debate.

Physical instability is the major hurdle that limits the commercial development of transdermal patches.[23] Controlling the critical factors that led to crystallization is a significant challenge faced by developers. The degree of crystallinity can be used to relate material characteristics and process parameters to the physical stability of amorphous drugs in transdermal patches. For example, the effect of small changes in the polymer molecular weight, solvent type, mixing, drying, or other factors on the drug recrystallization can be ranked according to drug crystallinity. However, no procedure for quantification of crystalline drug in DIA transdermal patches has been reported. The work outlined in this dissertation demonstrates how fast, non-

destructive spectroscopic methods can be used to accurately determine crystallinity of drug in DIA transdermal patches. A systematic approach that considers all relevant aspects of the analytical method (sample system, analytical system and quantitative model) represents a unique opportunity to investigate and control factors governing the recrystallization of drug in transdermal patches.

1.2 Hypothesis and Objectives

This dissertation is based on the central hypothesis that the extent of crystallization in transdermal patches can be quantitatively determined by Raman spectroscopy and Near Infrared spectroscopy. Thus, the quantitative methods for the determination of crystallinity of drug can be used in transdermal formulation development and studies of recrystallization kinetics.

Given the central hypothesis, the objectives of this dissertation were to:

1. Determine the feasibility of using NIR spectroscopy and Raman spectroscopy to determine crystallization of ibuprofen in Duro-Tak® 2052
   - Characterize drug-in-adhesive patches to determine the influence of patch physiochemical properties on NIR and Raman signal
   - Determine instrumental sensitivity and selectivity to two physical forms of drug (crystalline and supercooled)
2. Develop a powder coating-based method to prepare patches with known drug crystallinity
   - Verify the physicochemical properties of the spiked samples meet the requirements (physical stability and coating uniformity) to be used as calibration samples
3. Develop a quantitative calibration using NIR and Raman spectra for accurate crystalline content determination in DIA patches

- Calculate multivariate detection limit based on a total error approach
- Demonstrate method capability in predicting crystalline content in both spiked and naturally recrystallized patches
- Demonstrate a strategy for validation using accuracy profile and validation criteria (specificity, accuracy, precision and robustness).

4. Evaluate physical stability of supersaturated DIA patches via the established quantitative methods
   - Determine crystallization kinetics of the active pharmaceutical ingredient (API) in DIA patches using Raman spectroscopy
   - Quantify the effects of changing temperature and humidity on drug crystallization

The following flow chart demonstrates the topics covered in this document:

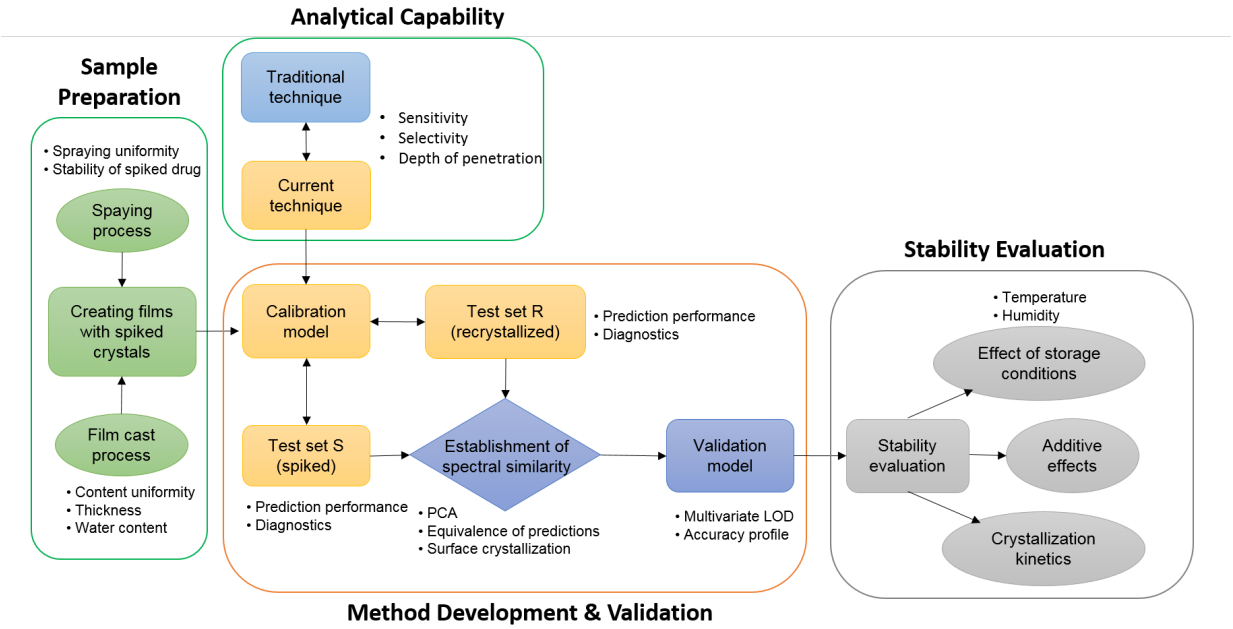

Figure 1.1 Summary of work presented in this dissertation.

Figure 1.1 demonstrates a systematic approach for drug crystalline content determination in DIA patches, covering all aspects of the analytical method including sample preparation and

characterization, analytical feasibility assessments, and multivariate model development and validation. This platform can be used for physical stability evaluation of DIA patches. It also offers a means to study the effects of formulation factors and storage conditions on crystallization in DIA patches.

1.3 Literature Survey

1.3.1 Drug-in-adhesive Transdermal Patches

A transdermal patch is a flexible, multi-layered, pharmaceutical, single dose preparation of varying size containing one or more active pharmaceutical ingredients (APIs) to be applied to intact skin for systemic absorption.[24] The transdermal drug delivery provides a prolonged release for drugs of short biological half-life, avoiding the first-pass effect and allowing removal of the patch conveniently during transdermal administration.[25]

Transdermal drug delivery can be achieved via active or passive systems. Active systems rely on external energy such as heat, electric current, sound waves or transient high-voltage electrical pulses to achieve the transport of the drug through the skin; passive delivery systems rely on chemical potential (concentration gradient). Drug diffusion through the skin into the systemic circulation is driven by the concentration gradient of the drug across the skin and the difference in solubility between the adhesive and skin. Patches for passive drug delivery can be classified into three main types: drug-in-adhesive (DIA) systems, polymer matrix systems and drug-in-reservoir systems.

The drug-in-adhesive system are the simplest form of passive transdermal drug delivery systems with reference to the straightforward design, uncomplicated manufacturing process, and

ease of application.[26] The adhesive polymer fulfills a dual function in DIA systems. One function is providing adhesion and the other is controlling drug release. A drug is directly dispersed into the adhesive polymer via solvent casting or hot melt extrusion. The DIA layer is then supported by an impermeable backing film on one side and is laminated with a removable release liner on the other side. The DIA patch is featured by the lighter, thinner and more flexible design that improve the conformity with skin surface variations.[4, 27] The simple design of the DIA system is favorable with respect to manufacturing, quality control and continuous product improvement.[26] Due to these reasons, the DIA type products have accounted for the largest share of the TDDS market since 2002.[4]

1.3.1.1 Pressure Sensitive Adhesives

Adhesives are a critical component of DIA systems. They are used to maintain close contact between the patch and the skin surface. Among the different classes of adhesives, pressure-sensitive adhesives (PSAs) are preferred. A pressure sensitive adhesives adheres to a substrate with light pressure and leaves insignificant amounts of residual adhesive upon removal from skin.[28]

A pressure-sensitive adhesive must meet several requirements to be an effective component of DIA patches. The adhesives must provide mechanical functions and release properties. Mechanical functions of the PSAs include skin adhesion, peel adhesion and resistance to shear. In terms of drug release, the PSAs govern the partitioning of drug into the skin from the DIA system. Meanwhile, long-term chemical compatibility between the adhesive, the drug, and any excipients is a pre-requisite for the PSAs used in DIA systems.

Among different types of PSAs, three of them are commonly used in transdermal patches. They are polyisobutylenes (PIBs), polysiloxanes (silicones) and polyacrylate copolymers

(acrylics). The selection of a PSA to be used in a TDDS is based on factors such as patch design, intended wear time, wear conditions and processability.[28] Acrylic PSA was selected for this study for its good chemical stability and inherent adhesion properties compared with PIBs and polysiloxane PSAs. In addition, acrylic PSAs provide better solubility and permeability for many drugs.[28]

This section will only discuss the structure and key properties of acrylate PSAs: chemical compatibility and adhesive properties. These topics are most relevant to the techniques that this dissertation covers.

Acrylic PSAs are formed by copolymerization of acrylic ester, acrylic acid and other functional monomers which may contain -OH or -COOH groups. The PSA acrylic monomers used in polymerization are comprised of 50-90% of primary monomers, 10-40% of modifying monomers, and 2-20% of monomers with functional groups.[29] Only four acrylic esters have been commonly used as primary monomers. They are 2-ethylhexyl, butyl, ethyl and iso-octyl acrylate.[30] The modifying monomers typically contain methyl acrylate, methyl methacrylate, vinyl acetate and styrene. Functional groups often added to the monomers include carboxylic, hydroxyl, epoxy, amide and organo-silane.[31]

Acrylic PSAs are highly resistant to oxidation because they only contain saturated hydrocarbon bonds that are hard to break. Stabilizers are frequently added to silicone-type adhesives to inhibit oxidation of the polymer arising from degenerative effects of oxygen, light, heat, and high temperature.[32] Examples of stabilizers are antioxidants and UV absorbers. Antioxidants scavenge free radicals and UV absorbers retard the photolysis of certain types of adhesive polymers. The need to add a stabilizer, which has the potential to cause skin irritation, is reduced because acrylic PSAs are chemically stable.

Types of monomers, cross-linking of functional groups and molecular weight are the three key parameters governing the adhesive properties of acrylic PSAs. The flexibility and tackiness of the adhesive is dependent on the side-chain length of the primary monomers.[30] The primary monomeric component has a low T_g that ensures a soft, tacky film. Therefore, plasticizer or tackifiers are not required in PSA systems. However, primary monomers lack the balance between tackiness and cohesive strength needed to resist an applied shear stress, other components are required to make a useful PSA.[32] A modifying monomer provides a clean removal and resistance to cold flow while a functional monomer is frequently used to improve the solubility or permeability of the acrylic polymers.

1.3.1.2 Skin Structure and Drug Selections

Skin is the most accessible surface for drug delivery. However, it remains a significant barrier to the penetration of drugs. The outmost layer, stratum corneum, is approximately 15 to 20 μm thick. It is composed of non-living corneocyte cells and intercellular lipids. Underneath this layer is the viable epidermis, which measures 130-180 μm.[33] The inner layer of the skin is the 2-3 mm dermis, which contains nerves, sweat glands, sebaceous glands, hair follicles, and abundant capillaries for systemic drug distribution.[34-35] The process of transdermal drug uptake through the skin is governed by passive diffusion into the stratum corneum. The corneocytes are embedded in intercellular lipids, forming a "brick-and-mortar" structure.[36] Drug molecules diffuse through the intercellular lipids via paths winding around corneocytes. The hydrophilic molecules travel through the lipid head group regions and lipophilic molecules travel through the lipid tails.[34]

Drugs suitable for transdermal delivery must possess suitable physiochemical properties, including an aqueous solubility over 1.0 g mL^{-1}, a log P between 1.0 and 2.0, a molecular weight

under 400 Da, and a melting point below 200 °C.[37] A balance between lipophilicity and hydrophilicity is needed to cross the lipophilic stratum corneum and cause absorption into the systemic circulation.[25] Additionally, drugs must not be locally sensitizing or irritating. Because of these criteria, only a limited number of drugs are suitable to transdermal administration.

1.3.1.3 Liner and Backing

A release liner is a thin layer that protects the drug layer until use. It is peeled from the adhesive layer prior to use. Low surface energy coatings are applied on one or both sides of the release liner to facilitate detachment. The coating materials include polyfluorosilicone, polysilicone and polyperfluorocarbons.[28]

Depending on the design and target use of a transdermal patch, backing materials are either permeable or occlusive. Occlusive backings are composed of synthetic polyesters that can cause hydration of the stratum corneum and thereby promote the permeation of drugs.[38-39] However, skin occlusion may cause hydration dermatitis when patches are applied for an extended period.[40] Permeable, or nonocclusive backings are composed of fiber-based materials that are preferred for patient comfort over long patch wear duration.

1.3.1.4 Supersaturation and Permeation Enhancement

The diffusion process can be approximated by Fick's first law of diffusion:[41-42]

$$J = DSK\frac{C_v - C_a}{h} \tag{1.1}$$

where J is the flux (g/s), S is the cross-sectional area(cm^2), D is diffusion coefficient of drug molecules in the skin (cm^2/s), K is stratum corneum-matrix partition coefficient, C_v and C_a are

concentration of drug in the transdermal patch and in the skin(g/cm^3) respectively, and h is the length of the diffusional pathway(cm). If sink conditions hold in the accepting compartment (skin), that is $C_a \approx 0$,

$$J = DSK\frac{C_v}{h} \tag{1.2}$$

Higuchi postulated that:[43]

$$K = \frac{c_a}{c_v} = \frac{c_a^*}{c_v^*} \tag{1.3}$$

where c_a^* and c_v^* are the saturated concentrations in the skin and the transdermal patch. Substitution of Equation (1.3) in to Equation (1.2) leads to:

$$J = DSK\frac{C_v}{h} = DS\frac{c_a^* C_v}{c_v^* h} = DS\frac{C_v c_a^*}{c_v^* h} = \frac{D\hat{a}c_a^*}{h} \tag{1.4}$$

where $\hat{a}$ denotes the thermodynamic activity that equals to $\frac{C_v}{c_v^*}$. Equation (1.4) clearly shows that the permeation rate increases with the drug's activity. Different mathematical equations describing diffusion-controlled systems can be found in the literature depending on whether the initial drug concentration is below or above drug solubility in the adhesive matrix.

If the drug is molecularly dispersed in the adhesive, *i.e.* the initial drug concentration is below the solubility in the adhesive matrix, the system is called a monolithic solution.[44] The drug release from monolithic solution systems can be described by:[45]

$$\frac{M_t}{M_\infty} = 1 - \frac{8}{n^2}\sum_{n=0}^{\infty}\frac{\exp\left[-\frac{D(2n+1)^2\pi^2 t}{l^2}\right]}{(2n+1)^2} \tag{1.5}$$

where M_t and M_∞ denote the cumulative amounts of drug released at time *t* and at infinite time, respectively, *D* is the diffusion coefficient of the drug within the system, and *l* represents the total thickness of the film.

When the drug is homogeneously distributed within an adhesive at an initial concentration that exceeds drug solubility,[44]and the system has reached equilibrium via drug crystallization,. this system is called a monolithic dispersion and the drug release from such a patch follows Higuchi's equation:[46]

$$M_t = A\sqrt{DC_s(2C_{ini} - C_s)t} \tag{1.6}$$

where M_t denotes the cumulative amounts of drug released at time *t*, *D* is the diffusion coefficient of the drug within the system, *A* is the total surface area of the film exposed to the release medium, and C_{ini} and C_s represent the initial drug concentration and drug solubility in the system, respectively.

In equilibrated suspension systems, the steady state flux of formulations with different initial concentration should be very similar if the dissolved drug concentration remains close to drug solubility. However, according to Equation (1.4), the rate of diffusion in a non-equilibrated system changes with thermodynamic activity ($\frac{C_v}{c_v^*}$), or the degree of supersaturation. Transdermal systems are often formulated with the drug supersaturated in the adhesive to achieve maximum thermodynamic driving force for passive diffusion across the skin.

1.3.1.5 Manufacturing Processes

DIA patches can either be manufactured using the solvent casting or the hot-melt technique. The solvent casting technique involves dissolving the API, the adhesive, and excipients in a common, volatile solvent. The homogenized solution is coated onto a release liner or a backing film. The film is dried in to remove the solvent. In the hot-melt technique, the API is added to the adhesive and heated to a temperature that allows the API to be completely melted and uniformly dispersed.[47] The hot-melt mixture is then extruded and laminated with a release liner and a backing under moderate pressure.

Amorphous API can be formed, either intentionally or unintentionally, during either patch manufacturing process. Heat and mechanical energy from the manufacturing may transform the crystalline drug into a metastable state(s). A few additional techniques have been used to produce drug in amorphous films. An inkjet printer was used to deposit a drug solution onto a polymer substrate to attain personalized dosage forms.[48] The method has demonstrated ability to print drug solutions on any porous or non-porous substrates and biodegradable films.[49] Solid-dispersion extrusion is a variant of hot-melt technique. Instead of mixing the powered drug with the molten polymer, a drug is dissolved in a solvent and added to the melt. In this way, material mixing can be performed at a lower temperature to prevent chemical degradation. Another method for making amorphous transdermal patches is electrospinning. A high voltage electric filed is applied to polymeric fluid stream to form solid fibers.[50] The electrospun fibers are then compressed into films. A list of manufacturing techniques is listed in Table. 1.1.

Table 1.1 Transdermal films manufacturing methods

Preparation method	Drug	Dose	Use	Film thickness	Reference
Ink-jet printing	Clonidine	7.6 - 250 µg/strip	Oral	0.1 ± 0.01mm	[51]
Ink-jet printing	Theophylline	7.49 ± 0.13 µg/cm^{-2} per pass of printing	NA	NA	[52]
Drop printing	Naproxan	30 and 70 (%, w/w)	NA	60 - 90 µm	[53]
Flexographic printing	Tadalafil & rasagiline mesylate	0.24 - 1.10 mg/6 cm^2	Oral	54.7± 0.5 µm & 56.8 ± 0.8 µm	[54]
Solvent casting	betamethasone 17-valerate	1.0 (%, w/w)	Prolonged dermal delivery	0.2 ± 0.02 mm	[55]
Solvent casting	Itraconazole	40 (%, w/w)	NA	0.15 ± 0.01 mm	[56]
Electrospun	Peptide P12	0.6 and 6 (%, w/w)	Topical fiber mats for skin burns	0.2 mm	[57]
Electrospun	Caffeine	11 (%, w/w)	NA	NA	[58]
Solvent casting	Betamethasone 17-valerate	1.2(%, w/w)	Topical	10 µm	[59]
Solvent casting	4-ethynyl-2-fluoro-2-deoxyadenosine	0.1 (%, w/w)	Topical vaginal	97 ±7.5 µm	[60]
Coating film	Nicotine	2.41 - 2.63 mg/6.51 cm^2	Oral	NA	[61]
Spin-coating	Felodipine	50 (%, w/w)	NA	5 - 10 µm	[62]
Continuous tape casting	Fenofibrate & Naproxen	FNB 4.7 - 26.0 NPX 2.8 – 23 (%, w/w)	Oral	500 – 1000 µm (wet thickness)	[60]
Hot-melt extrusion with flex-lip film die	Clotrimazole & nystatin	10 (%, w/w)	Antifungal denture adhesives	0.34 ± 0.02 mm	[63]
Hot-melt extrusion – injection molding	Felodipine	10, 20, and 30 (%, w/w)	Buccal patches	NA	[64]

1.3.2 Drug Crystallization in DIA Systems

The crystalline drug must dissolve into the polymer to permeate into skin. An effective way to improve drug delivery is to use amorphous solid dispersion (ASD).[65] The drug in an amorphous solid dispersion is preferably in the molecularly dispersed state.[66] Transdermal systems are frequently formulated with the drug supersaturated in the adhesive to achieve maximum thermodynamic driving force. However, recrystallization is spontaneous with the high internal energy. Different approaches for explaining the drug crystallization in polymer matrix have been postulated, but most of the methods only apply to systems where the storage temperature is lower than the glass transition temperature (T_g) of the drug-polymer system. Although the drug-in-adhesive systems do not fall into this category (T_g <0 °C), an overview of the current views on factors contributing to the crystallization in solid state would still be of great value to the understanding and minimization of the unwanted drug crystallization in transdermal patches.

Crystallization from supersaturated solid systems is a multi-step process that include amorphous phase separation, nucleation and crystal growth. Amorphous phase separation and nucleation usually precede crystal growth; however, in most cases, the three events are concurrent.

1.3.2.1 Amorphous Solid Dispersion

A solid dispersion is defined as a formulation where one (or more) active ingredient(s) is(are) dispersed in an inert carrier or matrix.[67-68] A solid dispersion in which drug and carrier are both amorphous is termed amorphous solid dispersion (ASD). An ASD can be classified as either a molecularly dispersed system or a phase-separated system depending on the number of amorphous phases. In amorphous molecular dispersions the drug(s) and the polymer(s) are mixed at the molecular level;[69-71] whereas in phases-separated ASDs drug(s) and polymer(s) develop

separate sub domains. Figure 1.2 demonstrates the structures of these two sub categories. Molecularly dispersed ASDs are reported to have many preferred properties over phase-separated ASDs. They have greater dissolution rates than the phase-separated systems for a number of poorly soluble drugs[72-73]. The physical stability is improved significantly by bringing drug and polymer molecules to the closest proximity in molecularly dispersed ASDs in which there are strong inter molecular interactions *i.e.* ionic, H-bond and electrostatic forces.[74-78]

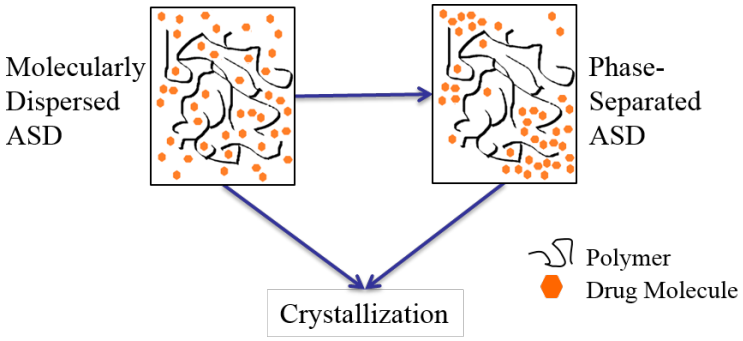

Figure 1.2 Schematic demonstration of two types of amorphous solid dispersions

1.3.2.2 Amorphous Phase Separation

Prior to phase separation, a drug is molecularly dispersed in an amorphous polymer matrix. If the drug concentration is lower than the equilibrium solubility of drug in polymer, the system is thermodynamically stable. However, the equilibrium solubility of drug in polymers may be relatively low at pharmaceutically relevant temperatures. Most molecularly dispersed amorphous solid dispersions become supersaturated as temperature is decreased from processing to storage. This can result in amorphous drug aggregates and potentially crystallization of drug. Compared to drug crystallization, a lower energy barrier is required to form a metastable structure of amorphous drug aggregates.[66]

1.3.2.3 Nucleation

Nucleation can be classified as either primary or secondary processes. Primary nucleation happens in a system that does not contain any nuclei, while secondary nucleation refers to nucleation occurring in the vicinity of preexisting crystals.[79] Primary nucleation may occur spontaneously (homogeneous) or can be induced by the foreign surfaces (heterogeneous). The overall kinetics of nucleation follow:[79]

$$J = A \exp\left(-\frac{\Delta G}{kT}\right) \tag{1.7}$$

where J is the rate of nucleation, *i.e.* the number of nuclei formed per unit time per unit volume, ΔG is the overall excess free energy between a small solid particle of solute and the solute in solution, k is the Boltzmann constant, A is the pre-exponential factor and T is temperature in Kelvin. ΔG is equal to the sum of the surface excess free energy, ΔG_S, i.e. the excess free energy between the surface of the particle and the bulk of the particle, and the volume excess free energy, ΔG_V, i.e. the excess free energy between a very large particle and the solute in solution.[79]

$$\Delta G = \Delta G_S + \Delta G_V \tag{1.8}$$

where ΔG_S is a positive quantity and is proportional to interfacial tension (γ) between the developing crystalline surface and the supersaturated solution in which it is located. ΔG_V is a negative quantity proportional to r^3.

$$\Delta G_S = 4\pi r^2 \gamma + \frac{4}{3}\pi r^3 \Delta G_v \tag{1.9}$$

The maximum value of ΔG corresponds to the critical nucleus, r_c is:

$$\Delta G_{crit} = \frac{16\pi\gamma^3}{3(\Delta G_v)^2} \tag{1.10}$$

where ΔG_v is the free energy change of the transformation per unit volume. The ΔG_v can be estimated from the basic Gibbs-Thomson relationship for a non-electrolyte:

$$\Delta G_v = -\frac{2\gamma}{r} = \frac{kT \ln S}{v} \tag{1.11}$$

where S is the degree of supersaturation (c/c*) and v is the molecular volume. The rate of nucleation can be derived from Equation (1.10), Equation (1.11):

$$J = Ae^{-\frac{16\pi\gamma^3 v^2}{3k^3T^3(\ln S)^2}} \tag{1.12}$$

Several variables that are important for the rate of nucleation are temperature, degree of supersaturation, and interfacial energy. In a study that evaluated the impact of interfacial energy on the crystallization tendencies in a series of Pentitols (xylitol, adonitol, 1-arabitol and d-arabitol), the crystallization processes of the pentitols were dominated by the interfacial energy rather than by a competition between the thermodynamic driving force and the molecular mobility.[80] However, since the liquid-crystal surface energy is difficult to determine independently, its relative intensity were reflected by the compound specific molecular conformations.

Other thermodynamic properties such as configurational entropy (S_c) and entropy of fusion (ΔS_m) have been measured and correlated to the crystallization tendency. The configurational entropy for a material can be expressed as:

$$S_{conf}(T) = \Delta S_m - \int_T^{T_m} \frac{C_{p,conf}}{T} dT \tag{1.13}$$

where $C_{p,conf}$ is configurational heat capacity, the difference in the heat capacity between the amorphous and crystalline states. Zhou relates S_c, and molecular mobility of five structurally diverse amorphous compounds to their crystallization behavior. Compounds with the highest S_c and lowest mobility were the most difficult to crystalize.[81] The molecules with higher

configurational entropies have more configurations thus it takes longer for the compounds to find the proper orientation to nucleate.[82]

1.3.2.4 Crystal Growth

Nucleation and crystal growth are two separate but concurrent processes. Molecules continue to transfer from the undercooled liquid to the surface of the nuclei during crystal growth. The mathematical equation proposed by Jackson to explain the dependence of growth rate ν on thermodynamic and kinetic factors is:[83-84]

$$\nu = \frac{6aD}{\Lambda^2} f \exp\left(-\frac{\Delta S}{k}\right)\left[1 - \exp\left(-\frac{\Delta G}{kT}\right)\right] \quad (1.14)$$

where a is the molecular diameter, D is the diffusion coefficient, Λ is the diffusion jump distance, f is the fraction of interface sites that are active growth sites, ΔS and ΔG are the entropy and the free energy difference between the crystalline and the supercooled liquid, k is the Boltzmann's constant, and T is the temperature. Equation (1.14) describes an opposite temperature dependence of the molecular mobility (diffusion coefficient) and thermodynamic driving forces (ΔS and ΔG). A maximum crystallization rate often shows up between T_m and T_g. The crystal growth rate is small at both high and low temperatures because molecular mobility is small below T_g and thermodynamic driving force is small as temperature approaches T_m.

The molecular mobility has a strong effect on the rate of crystallization. An effective strategy to slow down drug crystallization is to make amorphous solid dispersions. In these solid dispersions, a polymer with high viscosity is used to trap the molecules thus sustaining the supersaturation of drug for an extended period. Glass transition temperature (T_g) has been used to indicate molecular mobility. The difference between storage temperature and the T_g is frequently

used as an approximate measure of physical stability of an amorphous solid dispersion.[82] The T_g of the PSAs are usually much lower than the storage temperature, allowing the DIA system to be elastic but prone to drug recrystallization.

Among the many factors that influence molecular mobility, temperature and humidity have been shown to have practical influence on the physical stability of drug in transdermal systems.

1.3.2.5 Effect of Temperature on Crystallization

Both nucleation and crystal growth are temperature dependent. However, the influence temperature has on nucleation is different from that on crystal growth. That is because the driving force for crystallization has complex dependence on molecular mobility and on thermodynamic parameters. The relationship between temperature and nucleation, crystal growth and overall crystallization rates is illustrated in Figure 1.3.

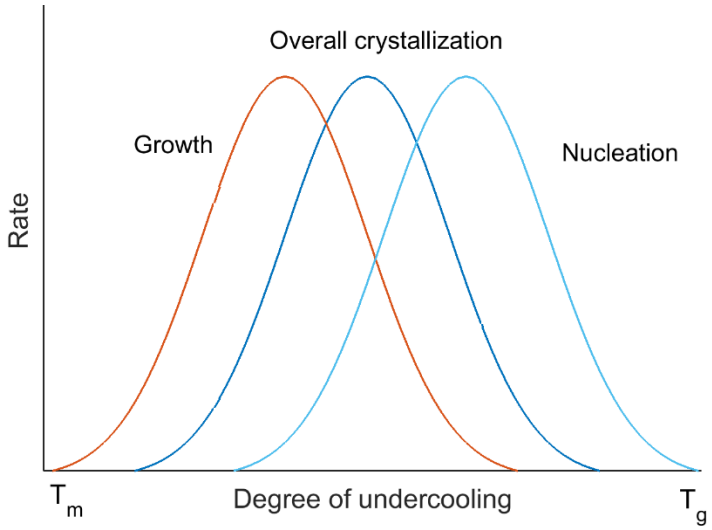

Figure 1.3 Reproduced from Newman and Taylor.[85] Schematic demonstrating temperature dependence of the nucleation, growth, and overall crystallization rates for undercooled melts.

The overall temperature-crystallization rate curve is influenced by both nucleation and growth rates. The nucleation rate increases with the degree of undercooling. It reaches a maximum

and then decreases as the temperature increases. The crystal growth rate, on the other side, show a maximum at a higher temperature than that for the nucleation. However, the extent of impact the crystal growth and the nucleation have on the overall crystallization process vary from one drug to another. As a result, the temperature dependence of crystallization rate is determined by the dominating process. A two-phase temperature dependence was observed for crystallization of lidocaine in a Duro-Tak® 87-2287 transdermal patch.[86] The temperature dependence is shown in Figure 1.3. The crystallization induction time τ of lidocaine was used to express the rate of nucleation J[87]. The longer the induction time, the smaller the rate of nucleation.

$$J = K/\tau \tag{1.15}$$

where *K* is a constant and that the induction time is inversely proportional to the nucleation rate. According to Arrhenius reaction velocity equation:[79]

$$J = A \exp\left(-\frac{\Delta G_c}{kT}\right) \exp\left(-\frac{\Delta G_d}{kT}\right) \tag{1.16}$$

where *A* is the pre-exponential factor, *k* is Boltzmann's constant, ΔG_c and ΔG_d are the activation energies to develop stable nuclei and for molecular diffusion, respectively. In Figure 1.4, the temperature dependence of the nucleation rate at various drug concentrations (40 to 70 %) exhibits a two-phase log linear dependence below and above a transition temperature. The transition temperature was correlation with the magnitude of ΔG_c and ΔG_d. Throughout the temperature evaluated, ΔG_d is much greater than ΔG_c, suggesting the crystallization is dominated by diffusion-controlled nucleation. However, there was a sharp jump in ΔG_c at the transition temperature, marking the potential changes in crystallization mechanisms. A discrepancy between the experimental results and the classical theory of nucleation is that the observed ΔG_c is not

dependent on degree of supersaturation. What caused the sharp transition in the temperature dependence needs further investigation.

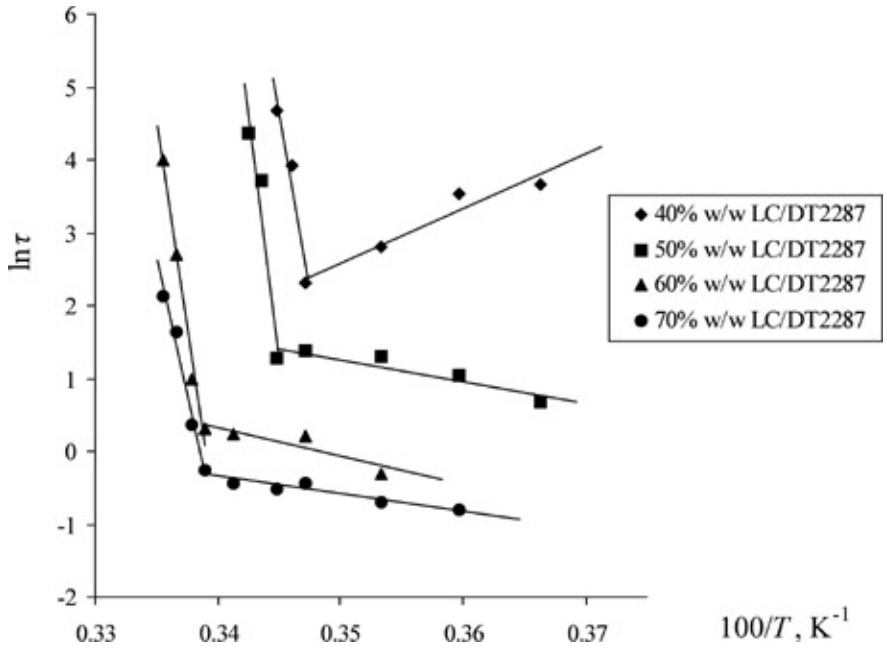

Figure 1.4 Reproduced from Cui and Frank.[86] A plot of $ln\tau$ and T^{-1} for lidocaine crystallization from Duro-Tak® 87-2287.[a]

Temperature can also influence where crystals appear throughout the thickness of the patches. The growth of estradiol in Duro-Tak® 87-2196 was monitored through optical microscopy and the crystals were only found in the middle third of the polymer.[10] J.Zeng simulated the location of nuclei and crystal growth in a PSA with a uniform 10% estradiol with a low and high temperature parameter k_bT (0.3 and 0.9, respectively).[88] With a high temperature parameter, the crystallization started in the middle of matrix and with a low temperature parameter, the grains were shown to evenly distribute throughout the thickness of the transdermal patch. At the beginning of the simulation, fluctuation of grains resulted in a few nuclei of critical size. These nuclei grew rapidly, accompanied by a drastic reduction in the solution concentration of the drug

[a] Reprinted from Isothermal crystallization kinetics of lidocaine in supersaturated lidocaine/polyacrylate pressure sensitive adhesive systems, 94(9), Cui Y, Frank SG, 2039-2048., Copyright (2005), with permission from Elsevier.

and Ostwald ripening of the grains. At low temperature, diffusion was too slow to sustain crystal growth; while only a few grains kept growing at a high temperature. One of the limitations of the study is that the drug molecule and the matrix polymer were assumed to be equal-sized. The molecular weight of polymer is usually 100-1000 times greater than the drug molecule. Another limitation of the study is that only 10% drug load was considered so no inference was given as to how drug load would influence the distribution of the crystals within the matrix.

The typical Arrhenius relationship does not hold as temperature increases. The most common model to describe the temperature dependence of structural relaxations (or viscosity) above T_g is Vogel-Tamman-Fulcher (VTF):

$$\tau = \tau_0 e^{\frac{DT_0}{T-T_0}} \quad (1.17)$$

where τ is the mean molecular relaxation time, τ_0 is the relaxation time consistent for the unrestricted material, D is the strength parameter, and T_0 is the zero mobility or Kauzmann temperature. The equation demonstrates the strong dependence of relaxation time on temperature.

1.3.2.6 Effect of Humidity on Crystallization

The impact of environmental humidity on the crystallization of amorphous systems is manifested as increases in both rates and the overall extent of crystallization. The presence of water usually reduces the glass transition temperature (T_g) of amorphous systems, which may lead to increased molecular mobility. The nucleation rates and crystal growth rates of felodipine from amorphous PVP films increased with storage relative humidity.[89-90] In these systems, the T_g of the polymer is much higher than that of the drug, so the T_g depression of these films was pronounced in the presence of moisture.

In another study, the physical stability of medicated (ibuprofen, salicylic acid and aspirin) acrylic adhesive transdermal films were found to decrease with the relative humidity. It was postulated that the absorbed water would decrease the solubility of drug in polyacrylate pressure sensitive adhesive Duro-Tak® 87-4287.[91] The dependence of drug solubility on humidity was explained by a change in the equilibrium between dissolved drug, drug bound to polymer via H-bonding and crystalline drug, as is shown in Figure.1.5. During dynamic vapor sorption (DVS) experiments, water molecules replaced drug molecules that ware bound to polymers and thus increased the portion of free dissolved drug available for forming drug crystals. Even though this study proposed a method to calculate drug solubility based on the water sorption isotherm, no direct quantitative measure of the drug solubility/crystalline content was provided. Experimentally, the maximum drug concentration where no crystal was observed over a 4-month period was used as the apparent solubility.

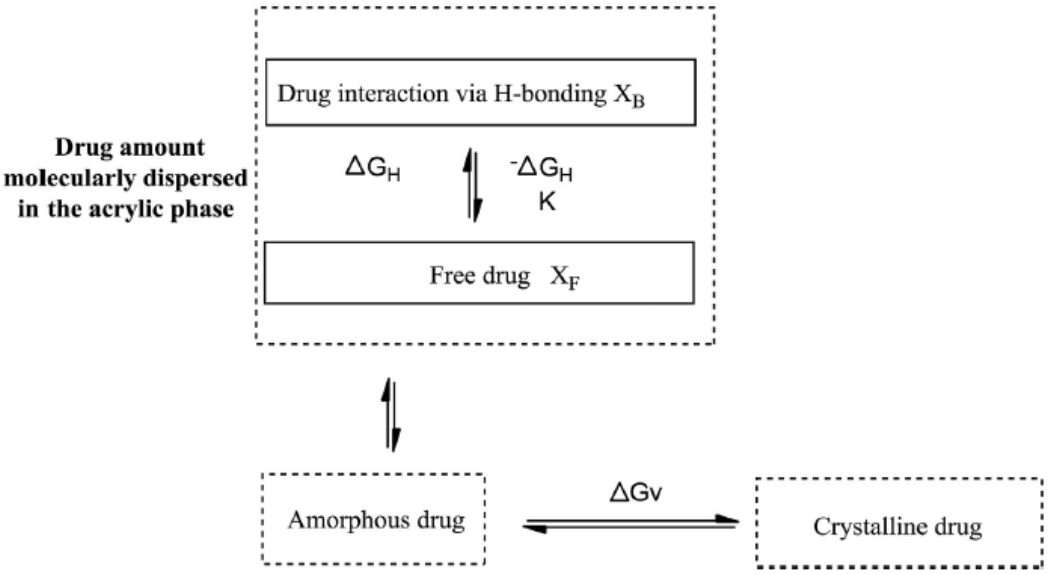

Figure 1.5 Reproduced from Chenevas-Paule and Dodou.[91] Different states of the drug in the acrylic matrix.[b]

[b] Reprinted from Development of a Predictive Model for the Long-Term Stability Assessment of Drug-In-Adhesive Transdermal Films Using Polar Pressure-Sensitive Adhesives as Carrier/Matrix, 165(3), Chenevas-Paule C, Wolff H-M, Ashton M, Schubert M, Dodou K, 1293-1301., Copyright (2017), with permission from Elsevier.

1.3.2.7 Surface and Bulk Crystallization

The surface profile of amorphous solids is particularly important for transdermal drug delivery.[92] Transdermal patches possess a relatively large contact area with the site of delivery. Therefore, the rate and extent of crystallization of the solid surfaces can have significant impacts on the application of a patch onto the skin and thereby influencing the efficacy of medication. The rate and the extent of crystallization at the solid surfaces is influenced by the physical and chemical properties of the surrounding environment, thermal history and processing conditions.[93]

Surface mobility,[94-95] surface energy and surface tension[96-97] are among a number of physiochemical properties that are key to the instability of amorphous solids on the patch-air surfaces. The crystallization is often faster at the free surface than in the interior[98] due to molecular mobility of the glassy materials.[99-101] The surface diffusion of small organic molecules were used to infer molecular mobility. C. W. Brian and L. Yu used surface grating to study the surface diffusion of glass Nifedipine.[102] They found the surface diffusion of Nifedipine is at least an order faster than bulk diffusion at 12K below glass transition temperature. In addition, the crystallization is dominated by surface kinetics. A good correlation was found between the surface crystal growth rates and surface diffusion rates.

The effects of a range of thermodynamic, kinetic and molecular parameters on the bulk and surface stabilities of amorphous films were evaluated in another study.[103] Molecular mobility was found to have the greatest influence among all the proposed parameters. The commonly used indicator T_g, fragility of the amorphous drug and the theoretically predicted drug-polymer solubility showed very limited influence on the bulk and surface stability. The order of bulk crystallization tendency of the four model drugs were the same with that of surface crystallization tendency. However, direct comparison between surface and bulk crystallization was not available

because different preparation methods were used for the two crystallization modes: melt quenching was used to study bulk crystallization while spin-coating produced films where the surface profile was measured. Inclusion of heat and solvents in the two preparation methods can have large impacts on the thermal history and molecular mobility of the samples.

Polymers were widely used to stabilize amorphous solids. The inhibition effect of polymers on drug crystallization at the surface is different from that in the bulk. Tian and coworkers tracked the growth of felodipine crystals detected from a filmy solid dispersion with PVP prepared on glass slips.[104] Co-milled API and PVP were melted on a glass slide covered with a top slip. The cover slip was later removed in the case of cover-free samples to observe surface growth; while the bulk crystal growth was observed without removing the cover slip. The onset time for crystallization was recorded. Crystallization was very fast at high drug concentrations (>90% w/w) and the onset times were similar between the surface crystallization and bulk crystallization. The polymer was reported to have a limited ability to slow down crystallization no matter it is on the surface or in the bulk when the concentration of polymer is low. The observation was consistent with Kestur's study in which 3% PVP had a slight impact on reducing the rate of crystallization of felodipine.[105] Nevertheless, the cover-free samples showed a faster onset compared to that of the double-sided samples at lower drug loadings (35 to 80 % w/w). Tian and coworkers pointed out that the faster rate of crystallization on the surface was attributed to the greater molecular mobility at the surface. In a similar study, Felodipine migration towards the PVP film surface was observed when the solid dispersions were stored in high humidity environment.[62] A substantial increase in the percentage of drug in the surface may promote to faster onset of surface crystallization in transdermal patches. Drug migration process of the thin films is illustrated in Figure 1.6.

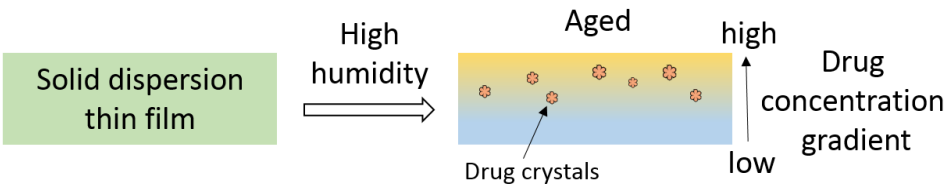

Figure 1.6 Reproduced from Qi, Moffat and Yang.[62] Schematic illustration of drug migration process of the thin films.[c]

1.3.2.8 Morphology and Polymorphism of Crystals

Crystals may present diverse morphology and have modified chemical composition within the transdermal patches. Optical microscopy revealed that β-estradiol crystals formed two distinctly different morphologies in a single layer inside the Duro-Tak® adhesive matrix: needle-like crystals and aggregates around the needles.[106] A Raman microscopic study showed the needle-like crystals contain the adhesive component and the aggregates are modified crystal form of estradiol. It was proposed that the crystallites of the polymer act as nucleation sites for growth of drug crystals in the aggregates and therefore the Raman spectra of the aggregates contain signatures of both the crystalline β-estradiol and the adhesive. A study further investigated the physical form of the estradiol aggregates. A splitting of the C-O peak at 1284 and 1294 cm^{-1} was attributed to the existence of at least two types of crystal forms: an anhydrous form and a hemihydrate form.[107]

[c] Adapted with permission from Early Stage Phase Separation in Pharmaceutical Solid Dispersion Thin Films under High Humidity: Improved Spatial Understanding Using Probe-Based Thermal and Spectroscopic Nanocharacterization Methods, 10(3), Qi S, Moffat JG, Yang Z, 918-930., Copyright (2013), American Chemical Society.

1.3.3 Analytical Techniques for the Quantification of Drug Crystallization in Pharmaceutical Films

The physical constituents of drug in the transdermal patches have impacts on the release of drug to the skin. The crystallization in pharmaceutical films needs to be measured to inform the efficacy and long-term stability of the products. An accurate and reliable analytical method is very useful in formulation development. The formation of crystalline drug can be visually observed by optical or polarized microscopy. However, the quantification of the crystalline API is very challenging because the development of a calibration requires the amorphous and crystalline phases to be separately prepared and weighed. Nevertheless, complete separation of the adhesive from the crystals is extremely difficult.[108] Therefore, only a few reported the quantitative method development for transdermal systems[109] whereas the quantification of crystalline drug in amorphous solid dispersions have been demonstrated for powders[110-111] and tablets.[18, 112-113] An overview of application of multiple analytical techniques, focusing on Near-infrared and Raman spectroscopy for the quantification of crystalline drug content in pharmaceutical film is presented in this section.

1.3.3.1 Optical Microscopy

Polarized light microscopy (PLM) is frequently used to determine the presence or absence of crystalline components in amorphous systems. This technology is based on the idea that an isotropic crystalline material refracts a light beam into two perpendicular rays as a result of changes in the refractive index along the optic axes of the crystal. This phenomenon is called double refraction or birefringence. As amorphous materials do not exhibit birefringence behavior, this technology is very sensitive to the presence of crystalline materials in amorphous solid dispersions. This technique can detect single particles, which makes it suitable for initial screening for

crystallization. Tian and coworkers tracked the growth of felodipine crystals detected from a filmy solid dispersion prepared on glass slips using PLM.[114] The growth rate was calculated from the change in distance from the edge of felodipine crystal to a fixed center point on a 2D image. However, a drawback of this method is that PLM does not account for crystals distributed vertically to the glass slide. Another limitation of qualitative or quantitative optical microscopy analysis is the problem of sub-sampling. In order to provide a quantitative measure of crystalline drug in a transdermal patch, a large number of images need to be acquired. Therefore, PLM is more appropriate for qualitative purposes.

1.3.3.2 Dynamic Vaper Sorption

Dynamic vapor sorption (DVS) provides information about location and speed of solvent sorption.[115] These information can then be related to amorphous content in solid dispersion, crystallization and specific API-polymer interaction in solid dispersion.[116] It is equipped with a microbalance capable of measuring changes in sample mass lower than 1 part per million.[117] Amorphous materials have a greater affinity for water than crystalline materials because both adsorption onto the surface as well as absorption into the bulk occurs in an amorphous material .[118] The amount of water taken up during adsorption is dependent on the available surface area whereas the amount of absorption is determined by the total mass of amorphous solids.[119] Once the amorphous content is determined from adsorption, the crystalline content can be calculated by subtracting the amorphous content from the total drug content.

The extent of crystallization can also be measured directly by DVS. A weight loss can be recorded during crystallization as the absorbed water is expelled from the amorphous materials. However, crystallization of APIs is not always accompanied by water loss. One exception is hydrate formation and another example is secondary absorption of the expelled water by

hydrophilic polymer in a solid dispersion.[120] Additionally, water sorption is proportional to the surface area of non-reactive components.[121] Thus, the moisture sorption is not specific to the amorphous component. Another conflicting factor is the formation of hydrogen bonds between APIs and polymers. It can reduce the number of water binding sites available during dynamic water sorption experiment and thus the sorption isotherm. Considering these factors, DVS is a semi-quantitative technique for crystalline content quantification and it is usually used in combination with other analytical techniques that are sensitive to phase changes.

1.3.3.3 X-ray Diffraction

Among several significant tools for solid-state characterization, powder X-ray diffraction is the most definitive technique for detecting crystalline drug(s) in ASDs. This technique probes the periodicities in molecular structures, thus implying the amorphous state by the absence of order.[122] The diffraction patterns of the crystalline solids are more distinctive compared to the halo diffraction patterns of the amorphous solids. The incident beam is diffracted by multiple layers of atoms creating constructive and destructive interference of the X-ray beams. Constructive interference is formed when the path difference between diffracted beams is equal to an integer multiple of the wavelength. This is described by Bragg's law:[123]

$$n\lambda = 2dsin\theta \tag{1.18}$$

where *d* is the distance between the planes in a crystal, expressed in angstrom, *n* is the order of reflection, and λ is the wavelength of X-rays. Assuming the experimentally measured signal intensities attributed to the crystalline and amorphous materials are proportional to the crystalline and amorphous fractions of the sample, the percent crystallinity (X_{cr}) of SDs in the sample can be estimated:[124]

$$X_{cr} = \frac{I_c \times 100}{I_c + I_a} \quad (1.19)$$

where I_c and I_a are the crystalline and amorphous intensities, or area contributions. Quantification of crystalline components in ASDs can be achieved by measuring the characteristic crystalline peak intensities, or the integrated peak area of the principal crystalline peaks[125] or the whole spectrum. An internal standard (IS) is often mixed with the sample before the diffraction pattern is recorded. The peak intensities of lines unique to the crystalline drug and to IS peak are used to calculate a ratio, which relates to the degree of crystallinity. Using an IS helps to solve the problems of peak overlap and background scattering.[126] Although this quantitative approach has been successfully applied on pharmaceutical powders, the solid-state evaluation of pharmaceutical films via XRD is largely qualitative.[127-130]

The determination of low quantities of crystalline API in ASD is not trivial. The dependence of signal on particle size is a confounding factor in the quantification of crystalline contents in powder samples. The diffraction line shape is also affected by the crystallite size and sample packing. Microcrystalline and nanocrystalline materials typically generate broadened peaks. Sometimes multiple peaks merge into a single broad peak that is easily confused with the amorphous halo. The influence of variations in the lattice strain and particle size on the integrated peak intensities is significantly reduced compared to that on the line shape; thus, the integrated peak intensities are more appropriate for quantitative analysis.[131] As to quantitative analysis of crystalline content in transdermal films, changes in particle size and porosity accompanying drug crystallization can cause variations in the signal. Other issues related with XRD, such as preferred orientation and micro-absorption,[132] could also present in transdermal patch systems.

In addition to quantitative analysis of crystalline materials, the XRD can be used to characterize the structure and miscibility of amorphous compounds via a method termed atomic pair distribution function (PDF).[133-135] This method has been suggested to provide finger-printing patterns for amorphous APIs and local packing information of APIs in the disordered solid states.[136] Powder X-ray diffraction spectra of ASDs are Fourier transformed into PDFs and then compared to the theoretical PDF profiles calculated from the amorphous polymer and amorphous API. PDF is the weighted probability of finding two atoms separated by their distance r:

$$g(r) = 4\pi r^2[\rho(r) - \rho_0] \tag{1.20}$$

where ρ_0 is the average atom number density of the structure, $\rho(r)$ the atom pair density for X-ray scattering, and *g(r)* represents the characteristic inter- and intramolecular distances found in a given material. It is calculated by Fourier transform of the reciprocal space structure function S(Q):

$$G(r) = \frac{2}{\pi}\int_0^{Q\ max} Q[S(Q) - 1]\sin(Qr)\,dQ \tag{1.21}$$

where *S(Q)* is the structure factor and *Q* is the magnitude of the scattering vector. The Q_{max} is the momentum transfer resolution of the diffraction experiment.

The PDF patterns of two different types ASDs are plotted as a function of r in Figure 1.7. If the PDF pattern in the dispersion is well described by the characteristic distances in the API and polymer, the dispersion contains isolated single components, *i.e.* there is a phase separation as shown in Figure 1.7(B). If a clear deviation of sample PDF from the theoretical profile is observed, the components in the solid dispersion are miscible.[137] Likewise, drawing a plot of residuals between the theoretical and measured PDFs helps to provide information about the drug-polymer miscibility. The relative contribution of API and polymer to the overall PDF is correlated to their relative weight percentages. A statistical interval can be drawn around the residuals to determine miscibility. Alternatively, a fitting algorithm can be used to determine the goodness of fit for the

same purpose. However, there is a lack of consensus on the threshold for determining the degree of fitting.[137]

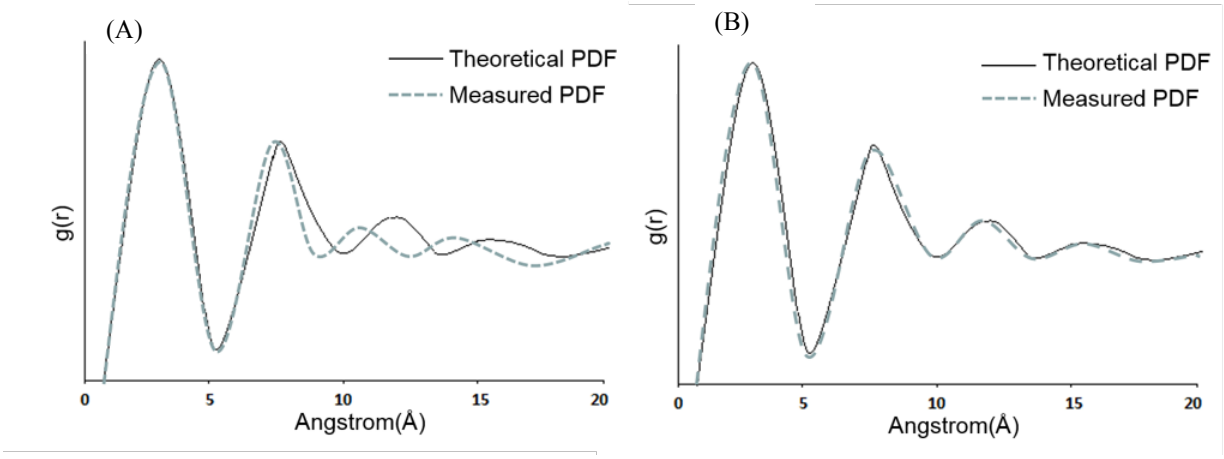

Figure 1.7 Theoretical and measured PDF profiles of a (A) molecularly dispersed ASD; (B) phase separated ASD.

M.D. Moore developed a method for drawing statistical inferences from the differences between experimental PDF transforms of PXRD data. The experimental error was estimated and passed along through the mathematical transformation. Specifically, the experimental errors comprised experimental imprecision and sample inhomogeneities. Meanwhile, there were uncertainties due to data corrections, as well as artifacts incurred from Fourier transformation. The resulting estimates of propagated errors for individual PDFs were combined to define uncertainty intervals surrounding the residuals. It helped to distinguish differences between PDF patterns arising from structure sources rather than from random error.[138]

1.3.3.4 Differential Scattering Calorimetry

Differential scanning calorimetry (DSC) is a powerful technique for understanding the miscibility and crystallinity of chemical components in amorphous systems. The sample is heated at a linear rate through its melting point in the conventional DSC. A pure crystalline material shows a single sharp endothermic peak at the melting temperature. Amorphous materials are

characterized by an endothermic event called glass transition. Recrystallization of the amorphous phase sometimes takes place during a DSC measurement resulting in an exothermic peak. The exothermic recrystallization peak and endothermic melting peaks are often used to calculate the crystalline fraction of the drug.[139] The crystalline content in a given sample can be estimated from the heat of crystallization or enthalpy of fusion:[140]

$$X_{cr} = \frac{\Delta H}{\Delta H_0} \times 100\% \quad (1.22)$$

where ΔH is the enthalpy of fusion of the sample and ΔH_0 is the enthalpy of fusion of the 100% crystalline standard. The calibration samples consist a series of physical mixtures of amorphous API, crystalline API, and excipients.[131]

Differential scanning calorimetry is very useful for understanding crystallization kinetics and the influence of environmental factors on physical stability of solid dispersions. The recrystallization kinetics of amorphous solid dispersion of efavirenz-polyvinylpyrrolidone was measured by DSC. Melting enthalpy of the solid dispersions were used to calculate relative crystallinity. An improved Avrami equation was taken to describe the recrystallization kinetics of fenofibrate in hot-melt extruded solid dispersion containing hydroxypropyl cellulose and HPC.[141] This equation assumes the nucleation rate decreases as the available nucleation sites are consumed.[142] In another study, differential scanning calorimetry analysis was performed to quantify the crystallinity of naproxen in a solid dispersion formulated with glycol. Such solid dispersions were coated by different grades of PEG to study the effect of coating on the rate of crystallization. The crystallinity after storage in 75% RH decreased as the molecular weight of the PEG coatings was increased.[143]

Samples in the form of films are particularly suitable for DSC measurement because close contact between a film and the sample holder is achieved with a flat film. In this way, effective

heat conduction between the pan and the material can be ensured. However, films need to be folded when multiple pieces are used in a single pan; loose packing may result in poor heat transfer. In the case of particle bearing films, the effect of sample heterogeneity on DSC measurement must not be ignored.

1.3.3.5 Near Infrared and Infrared Spectroscopy

Spectroscopic methods such as near-infrared and infrared spectroscopy have been used for crystalline phase quantification in pharmaceutical solid dosage forms. IR bands of most pharmaceutical ingredients, such as O-H stretching vibration, C=O stretching vibration and OH vibration, are highly specific and they are associated with the chemical structure and inter molecular interactions of samples. The absorption bands in the NIR region include overtones and combinations of fundamental vibrations of the- CH, -OH, C-O, -NH and S-H functional groups present in most active pharmaceutical ingredients. Near infrared spectroscopy has been used to quantify amorphous content in a crystalline matrix[144] and physical mixtures of crystalline and amorphous drug in the presence of excipients.[145] Vibrational spectroscopy based techniques have been demonstrated to have equal or better sensitivity than XRD for crystalline content quantification in powders.[146] Other advantages of IR based techniques include non-destructiveness and rapid analysis.

Despite the benefits that NIRS may bring, NIR spectra contain board and overlapping peaks that are difficult to resolve. Additional challenges are associated with the unexpected signal variations caused by physical variations such as density, particle size, and sample presentation.[147-149] Therefore, qualitative and quantitative analyses are often performed with multivariate methods

including principle component analysis (PCA), multivariate curve resolution (MCR), classical least squares (CLS), and partial least squares (PLS).

The penetration depth of NIR light determines the sampling volume obtainable by a NIR instrument. If the sampling volume is too small compared to the unit dosage form, there is a sub-sampling problem. The typical penetration depth of NIR radiation in powders is between 0.1 and 2.0 mm.[150-151] The actual penetration depth strongly dependents on the chemical composition, particle size, powder density and wavelength. The refractive index in transdermal patches is more uniform than that in a turbid medium(powders, tablets and suspensions).[152]

NIR imaging serves as a versatile adjunct to the NIRS for studying the spatial distribution of components in a formulation, including crystalline components. The distribution of crystalline tulobuterol in a reservoir-type transdermal film was investigated by T. Sakamoto and coworkers.[153] The second derivative peaks were used to probe the presence of the crystals in transdermal films. A time-course NIRS measurement showed the intensities of the peaks corresponding to the crystalline drug increased from zero to maxima in six weeks.

1.3.3.6 Raman Spectroscopy

Raman spectroscopy is one of the most common techniques for probing solid phase transformations.[154] A monochromatic laser beam interacts with molecular vibration, phonons or other excitations in the sample, resulting in energy changes of the laser photons.[155-156] The molecular vibration, rotation or phonon mode of the irradiated material shifts the energy (or frequency) of the incident photon. The vibrational modes of Raman spectra are useful for probing changes in molecular structure, molecular conformation and packing changes during crystallization. Molecules in crystals are arranged in a repetitive structure and thus bonding environment of Raman-active bands is the same in each molecule.[157] The Raman peaks of

amorphous phases are less intense than peaks from crystalline forms. Additionally, peak shifts are often observed upon crystallization. These phase changes are often used in quantitative analysis to assess the physical stability of amorphous solid dispersions.

Both Raman spectroscopy and Raman imaging have been used to detect crystallization from amorphous solid dispersions.[158-159] An confocal Raman microscope is capable of focusing an excitation laser beam to an area as small as 50 um[160] in diameter. providing images revealing the spatial distributions of API and polymers in ASD films. Tian and coworkers employed Raman imaging to examine the phase compatibility felodipine and a polymer at various compositions.[160] The polymer is either HPMCAS, Soluplus®, or PVP. The drug weight fraction varied from 35 to 90 %. The solid dispersions were prepared by co-milling powders of the drug and the polymer into homogeneous mixtures. The mixtures were melted and cast onto glass slips. The distributions of the components in the formed film were monitoring by a Raman imaging system. A phase map was obtained during an annealing process. The spectral features at 1750 – 1450 cm^{-1} were used to correlate Raman spectra to the crystalline form of felodipine. In the first few days a uniform phase map showed a poor correlation with the crystalline form, suggesting the film was mostly amorphous. This is followed by an increase in the amount of crystalline felodipine from the edges to the entire film.

The applications of Raman spectroscopy for solid state analysis within polymeric films have been increasing over recent years. Changes in the crystallinity of drug in hot-melt extrudates can be monitored by Raman spectroscopy to identify out-of-spec products.[161-162] Solid dispersion coupled with 3-D printing were proposed to produce films containing amorphous paracetamol and Eudragit L100-55.[162] Crystalline particles were found on films by a confocal Raman microscope.

The crystalline API was not from recrystallization of the amorphous form but was the residual, un-sintered drug powder that had not been effectively cleared away after the previous batch.

In-line monitoring of crystallization has been implemented in batch crystallizations. However, the applicability of Raman for physical stability assessment in film samples is limited by several drawbacks including interference due to fluorescence, sample heating and presence of strong peaks in Raman spectra from organic solvents. These drawbacks may adversely influence the quantitative capability of Raman instruments for crystalline content determination in transdermal patches.

Spectral preprocessing helps to reveal the spectral differences between different forms of drugs. The residual drug crystallinity in a melt-extruded spironolactone-Eudragit E solid dispersion was estimated using confocal Raman imaging and transmission Raman spectroscopy.[157] Classical least squares (CLS) scores were computed based on the spectra of pure Eudragit E, amorphous spironolactone, and crystalline spironolactone. Samples made with different extrusion temperature, screw speed, residence time and drug loading, were produced to ensure a varying degree of crystallinity. All the samples were screened by XRD and DSC. Nevertheless, no reference value of crystallinity was obtained because the pure amorphous drug was too unstable under the storage condition. Due to a lack of reference methods, the author pointed out that crystallinity determined are only suitable for preliminary comparisons.

Quantification of crystalline content in amorphous systems is challenging since the physical mixtures used to build calibration are either unavailable or too unstable.[21] A method that does not require calibration would be advantageous. Classical least squared (CLS), multivariate curve resolution (MCR) and band target entropy minimization (BTEM) are among the most common multivariate methods for estimating crystallinity. Band target entropy minimization is a

self-modeling curve resolution technique for elucidating phase compositions. E. Widjaja found trace crystalline griseofulvin particles in Kollidon VA64 dispersions via this technique.[22] The goal of BTEM method is to reconstruct the underlying spectral shape of amorphous and crystalline drug in the absence of priori knowledge of crystallinity. This method not only enabled minor crystalline domains of griseofulvin to be detected, it also differentiated the two polymorphic forms of the drug.

1.3.3.7 Other Analytical Considerations

The conventional approach to characterize the physical states in transdermal patches involves applying multiple complementary analytical techniques. Using multiple techniques for accurate identification of crystalline phase in the presence of amorphous or dissolved phase is often necessary because it is very challenging to obtain specific differences in long-range order using a single technique. Despite the many successful examples of accurate phase identifications, drawing information from multiple instruments has many limitations. The destructiveness and time-consuming nature of one or more conventional techniques reduce the reliability of test results. As the destructive method needs to be the last step of the analyses, a sample has waited for a long time before the final test. Conflicting results generated from different analytical techniques may occur as the amorphous drug continues to recrystallize over the time frame of the analyses. Additionally, interpretation of phase information is generally complicated because different analytical techniques demonstrate diverse degrees of sensitivity to the crystalline and amorphous phases.

Accurate determination of crystallinity in transdermal films with low dose APIs is limited by the detection limit of conventional techniques. The detection limits of XRD for crystalline APIs

is typically 2.0 – 5.0 %.[163-164] The detection limit of solid-state nuclear magnetic resonance spectroscopy (SSNMR) is less than 0.5 %. By far the highest sensitivity for crystal drug determination was reported for second-harmonic generation microscopy. Second-harmonic generation guided analysis exhibited a detection limit as low as parts per trillion.[165]

Amorphous phase separation is considered one of the events preceding crystallization of amorphous drugs from ASDs. The detection of phase separation in ASD requires high spatial resolution. The size of separated domains detectable by DSC measurements is about 30 nm.[134, 166] The diffraction limit of traditional microscopy is about 1 to 10 microns. The birefringence microscopy is very sensitive to crystals, but it cannot differentiate different amorphous components. It was postulated that pair-wise distribution function coupled with XRD has the capability to distinguish nano-size phase separations. The use of time of flight-secondary ion mass spectrometry (TOF-SIMS) to characterize ASDs is limited to the 1-2 nm exterior layer of a film.[167] Therefore, the volume of interrogation only constitutes a tiny fraction of the sample. The detection limit of second harmonic generation microscopy is about 5 orders of magnitude lower than that of optical microscopy.[168] A solid-state nuclear magnetic resonance spectrometer is able to detect molecular-level movements down to the angstrom scale.

1.3.3.8 In-line PAT Applications

The incorporation of PAT tools into continuous film manufacturing processes is clearly preferred by PAT guidelines as it exhibits tremendous advantages for process monitoring and automation.[152] Advantages include rapid and non-destructive measurements, and the ability to detect multiple properties. Physical stability is an important quality attributes that can be analyzed by several spectroscopic methods, as described in previous sections. Near-infrared spectroscopy

and Raman spectroscopy have been increasingly used to determine the critical product quality attributes in pharmaceutical film products such as hot-extruded transdermal films.

F. Hammes implemented a reflectance infrared spectrometer for in-line monitoring of an nicotine oral thin film during coating process for an oral thin film production.[61] M.T.Isam presented a transmission NIR method for the monitoring of indomethacin transformation from the crystalline state to the amorphous state during hot-melt extrusion. J. Zhang used Raman spectroscopy to monitor drug content in strip film manufacturing. The Raman method developed by J.Zhang et.al. was robust to sensing location, substrate speed, and film thickness.[169] The crystalline content of hot-extruded samples can be related to multiple product properties and process variables. These variables include zone temperatures of the barrel, screw speed and residence time.[170] The relationship between the residual drug crystallinty[157] and the process variables, such as zone temperature of the barrel, screw speed and residence time, can be acquired by an in-line spectroscopic tool to ensure the product quality.

1.4 Stability Testing of Transdermal Patches

The purpose of the stability testing of a drug product is to help select adequate formulation and primary packaging material, and to determine shelf life and storage conditions for the drug.[171] The attributes of the drug products that are susceptible to change during storage and are likely to influence quality, safety, and efficacy should be included in stability studies.[172] The stability testing of transdermal patches can be conducted at three conditions: long term (12 months), intermediate (6 months), and accelerated storage conditions (6 months) according to ICH guidelines.[172] The accelerated stability studies are conducted at 40 °C ± 2 °C and 75 % RH ± 5% RH representing an elevated temperature and a high relative humidity.

Physical stability testing is an integral part of the stability studies for DIA transdermal patches. The detection of crystallization of drug in PSA patches are only done with qualitative analytical methods. Appearance of crystals were monitored visually and microscopically as an indicator of physical instability. The process of crystallization was generally described by the classical theory of nucleation theory,[86, 173-174] using data generated from DSC, XRD and isothermal calorimetery.[86, 175-176]

Chapter 2 : Preparation and Characterization of Drug-in-adhesive Transdermal Patches

2.1 Background and Introduction

The phase composition of the API exerts a profound effect on the solid-state properties of the DIA system. Thus, characterization of the active pharmaceutical ingredients in the solid state is critical to the development of useful transdermal formulations. To ensure the physical integrity and consistent release of a DIA system containing a metastable form of API, the physical properties of the drug, excipients and their mixtures must be thoroughly evaluated.

The quality tests for transdermal systems are outlined in USP <3> 'Product Quality Tests'.[177] Among a dozen frequently tested product quality attributes, visual examination of crystallization by conventional optical or polarized microscopy remains the primary method for physical stability evaluation in transdermal patches. The visual examinations of crystalline components are subjective to the judgement of the individuals. Additionally, crystallization has been known to negatively impact the in-vitro and in-vivo drug release. Therefore, the crystallization must be monitored throughout the development of transdermal formulation. A quantitative spectroscopic method for crystalline content determination of the API offers tremendous advantages over the traditional solid-state characterization methods. These advantages include rapid and non-destructive analyses, low detection limits for crystalline APIs, and simultaneous analyses of all chemical components in a formulation.

Practical investigations of a spectroscopic method for solid-state quantification in pharmaceutical solids were required in the early-stage development. They include a comprehensive understanding of the pharmaceutical system, a thorough investigation of potential effects of formulation variables on a calibration model, and quantification of analytical capability

of the instrument.[178] The second chapter addresses the first two aspects by introducing the DIA system and laying out the experimental methods used to test the physiochemical properties of the DIA system. These pieces of information regarding an analytical procedure is of particular importance to the understanding of the variability of the sample system, the dynamic range, the regression model, and limits(s) of quantification.[179] Ibuprofen and the adhesive were mixed at different concentrations and prepared at changing thickness levels. Samples were tested in terms of the quality attributes and physical stability. The quality attributes include thickness and thickness variations, weight and weight variations, drug content and content uniformity. The solubility of the API in the adhesive was calculated to determine the physical stability of the DIA patches. This chapter also investigated the influence of the thickness on the NIR signal or the Raman signal. This study helps to determine whether the patch thickness need to be controlled prior to crystalline content quantification.

2.2 Experimental Methods

2.2.1 Materials

The proposed drug-in-adhesive transdermal patch is composed of three layers: a liner (3M Scotchpak™ 9755 release liner, 3M, St. Paul, MN, USA), a drug-bearing adhesive layer and a backing layer (3M Scotchpak™ 1012 backing, 3M, St.Paul, MN, USA). The model API is (RS)-ibuprofen (Thermo Fisher Scientific, Waltham, MA, USA), a nonsteroidal anti-inflammatory analgesic that reduces fever and treats pain. The adhesive Duro-Tak® 2052 (Henkel Corporation, Stanford, CT, USA) is an acrylates copolymer with free -COOH groups. The target formulation contains ibuprofen (23.5% w/w) and Duro-Tak® 2052 (76.5% w/w). Four batches were made on different days to determine the intra and inter batch variations in API content and thickness.

DIA patches were prepared at predefined levels (Table 2.1) to evaluate the effect of patch thickness on the signal. The API content was calculated from the dry mass of the adhesive solution (determined from non-volatile content). Prepared transdermal patches were cut to a size of 1.5 cm by 1.5 cm for physical and chemical evaluations.

Table 2.1 Composition and thickness of DIA patches used to evaluate the influence of thickness on Raman and NIR signal

Batch number	Drug load (%, w/w)	Adhesive load (%, w/w)	Thickness (mm)
P1	23.5	76.5	0.40
P2	23.5	76.5	0.50
P3	23.5	76.5	0.55
P4	23.5	76.5	0.60
Blank	0.0	100.0	0.55

2.2.2 Preparation of DIA Patches by Solvent Casting

Ibuprofen powder was dissolved in ethyl acetate to produce a 40% w/w solution. The solution was stirred until the drug was fully dissolved. Duro-Tak 2052® was added into this solution and homogenized overnight. The solution was cast onto a release liner when the solvent content of the solution was approximately 12 % w/w. The final solvent content was estimated based on mass of the final solution. A gardener knife was used to achieve consistent thickness. Casting was followed by drying in the hood at 25 °C for 2 hours. Then they were further dried at 55 °C for 24 hours until weight changes were less than 1 % w/w. The oven temperature was kept below the melting temperature of the drug (76 °C) but above the glass transition temperature of the drug (-42 °C). The adhesive layer was laminated with a backing film. The prepared patches were equilibrated at 25 °C and 32 ± 2 % RH for 24 hr prior to physical characterization.

2.2.3 Characterization of DIA Patches

2.2.3.1 Non-volatile Content of PSA

The non-volatile content (NVC) of the adhesive solution was determined gravimetrically. Accurately weighed aliquots (1.0 g) of adhesive solutions were dried at 75 °C for 24h and weighed to determine non-volatile content.

$$NVC(\%, w/w) = \frac{(a-b)-(c-b)}{a-b} \quad (2.1)$$

where a is the mass of an adhesive solution plus a weighing pan prior to drying, b is the mass of the same weighing pan, c is the mass of the dried adhesive plus the weighing pan.

2.2.3.2 Thickness and Weight Variation

Each patch was measured with a digital micrometer (Micromaster IP54, BROWN & SHARPE TESA, North Kingstown, RI, USA) and a digital balance (AX504 Delta Range, Mettler-Toledo, LLC, Columbus, OH, USA) across three locations to determine the thickness variations within a single patch. Six patches from each batch were characterized in terms of thickness and weight variation within each batch. Four batches of DIA films were prepared on three separate days to determine the thickness and weight variations across batches.

2.2.3.3 Drug Content

Samples were weighed after release liners were peeled off. The mean weight of the backing was determined by weighing 10 backings of the same size (1.5 by 1.5 cm) and was subtracted from the mass of each DIA patch. Each DIA patch sample was placed in a 50 mL beaker and 20 mL

PBS 7.4 solution was added. The sealed beaker was homogenized in a shaker (Branson 8210 Ultrasonic Cleaner, Branson Ultrasonics Corp., Danbury, CT, USA) for 24h. The shaker speed and temperature were set at 30 rpm and 40 °C, respectively. The resulting solution was added to a 100 mL volumetric disk. A 1:20 dilution was performed by adding 5mL of solution to 100mL volumetric disk. Filtered solution was analyzed at 223 nm by an ultraviolet-visible (UV-vis) spectrometer (Hewlett Packard 8453 UV-Visible, Agilent Technologies, Santa Clara, CA, USA). The drug content was expressed as the solid weight fractions of drug/DIA layer (%, w/w).

2.2.3.4 Drug-adhesive Interactions

The compatibility of the drug and the adhesive was evaluated using Fourier-transform infrared (FTIR) spectroscopy. The appearance of new absorption bands, changes in peak positions and alterations in peak intensities indicate interactions between the chemical components.[180] The samples were dried and measured using a Spectrum BX FTIR Spectrometer (Perkin Elmer, Waltham, MA, USA) with an attenuated total reflectance sampling accessory. Measured samples included: ibuprofen powder as received, Duro-Tak® 2052 films prepared using the procedure described in 2.2.2, and DIA patches with a drug-adhesive weight ratio of 1:1. The samples were measured with three replicates. A background scan was collected and subtracted from each sample spectrum. Absorbance spectra were recorded in the transmission model in the mid-IR region (4000-400 cm^{-1}) with 64 scans and a 4 cm^{-1} spectral resolution.

2.2.3.5 Solubility of the drug in the Adhesive

The equilibrium solubility of ibuprofen in Duro-Tak® 2052 was calculated using two methods. The first method was based on the limiting form of the Flory equation:[181]

$$\phi_1 = e^{-(1+\chi_1)} = e^{-(1.34+\frac{v_1}{RT}\times(\delta_1-\delta_2)^2)} \quad (2.2)$$

where ϕ_1 is the volume fraction of the solute (can be used to estimate mass fraction), χ_1 is the interaction parameter, v_1 is the molar volume of the drug, δ_1 is the solubility parameter of the drug, δ_2 is the solubility parameter of the acrylate-vinyl acetate copolymer, *R* is the gas constant (8.314 $JK^{-1}mol^{-1}$), and *T* is the temperature (298K).

The second method for calculating the solubility of ibuprofen in Duro-Tak® 2052 was the regular solution theory equation. [182] Scatchard-Hildebrand equation relates the activity of a drug to the solubility parameters of the polymer and the supercooled liquid of drug:

$$\ln\left(\frac{a_1}{x_1}\right) = \frac{v_1\phi_2^2}{RT}(\delta_1 - \delta_2)^2 \quad (2.3)$$

where a_2 is the drug activity, x_1 is the drug molar fraction and ϕ_2 is the polymer volume fraction. Assuming the heat capacity of the drug is constant, the drug activity can be approximated by:

$$lna_2 = -\frac{\Delta H_{fus}(T_m - T)}{RTT_m} \quad (2.4)$$

where ΔH_{fus} is the enthalpy of fusion ($J.mol^{-1}$) of the drug and T_m is the melting temperature (K). The drug mass fraction in PSA can be estimated by x_1 based on Equation (2.3) and (2.4), assuming $\phi_2 \approx 1$:

$$lnx_1 = -\frac{\Delta H_{fus}(T_m - T)}{RTT_m} - \frac{v_1\phi_2^2}{RT}(\delta_1 - \delta_2)^2 \quad (2.5)$$

Solubility parameter values were determined based on Hoftyzer and van Krevelen's group contribution method:

$$\delta_d = \frac{\sum F_{di}}{v} \quad (2.6)$$

$$\delta_p = \frac{\sqrt{\sum F_{pi}^2}}{v} \tag{2.7}$$

$$\delta_h = \sqrt{\frac{\sum E_{hi}}{v}} \tag{2.8}$$

where δ_d δ_p, and δ_h are the solubility parameter contribution of dispersion, polar and hydrogen bonding components, $F_{di}$and F_{pi} are group contribution to the dispersion and polar components, E_{hi} is the hydrogen bonding energy, and V is the molar volume. δ_t is the total solubility parameter estimated from the three solubility parameter contributions:

$$\delta_t = \sqrt{\delta_d^2 + \delta_p^2 + \delta_h^2} \tag{2.9}$$

Patches used to experimentally verify the calculated solubility were prepared with varying mass fractions (11,13,15,17,19% w/w) of drug. The patches were stored at 32 ± 2% RH and 25 °C for six months to determine the maximum concentration at which no crystallization was detected by a polarized light microscope (Olympus BX-51 light microscopy). This storage condition represented the center design point used in Chapter 5. The degree of supersaturation of drug in the adhesive was calculated by taking the ratio between the target drug concentration and the equilibrium solubility.

2.2.3.6 Absence of Crystalline Drug in Freshly Prepared DIA Patches

A polarized light microscope (Olympus BX-51 light microscopy, Tokyo, Japan) was used to confirm the absence of crystallinity in freshly prepared DIA patches. Additionally, the absence of crystalline API was determined by an X-ray diffractometer (XRD) (X'Pert Pro MPD system,

PANalytical B.V., Almelo, Netherlands). The step size was 0.017 ^{o} 2θ over a range of 2-100 ^{o} 2θ and the irradiation time per step was 51.04 s.

2.2.3.7 Distribution of the Crystalline Drug

Transdermal patches made according to design point P2 (Table 2.1) were stored at 25 °C Crystallization of ibuprofen was monitored by a microscope. The samples were cut, and the cross-section areas were observed to determine the distribution of crystallized drug.

2.2.4 Effect of DIA Patch Thickness on Spectral Signal

2.2.4.1 Spectral Data Collection

a. Near-infrared

DIA patches were measured using a diffuse transflectance setup shown in Figure 2.1. A white Teflon plate was used as a reflector. Eight detectors were displaced at 45 degrees from normal relative to the plane of the sample, as is shown in Figure 2.1(B). The liner side of the patch was placed towards the measurement window while the backing layer was placed towards the Teflon plate. Each patch was positioned at the center of the widow of a NIR spectrometer (XDS Rapid Content Analyzer, Metrohm, Eden Prairie, MN, USA). The spot size of the instrument was 17.25 mm, and 32 spectra were averaged to produce one spectrum. The loss in absorbance due to scattering of light from the particles inside the patches was corrected by subtracting a spectrum of the sample measured using a black tape. The NIR absorbance of a patch sample is calculated taking account of the patch thickness:

$$A_c = [-\log\left(\frac{I_S - I_D}{I_W - I_D}\right) + \log\left(\frac{I_B - I_D}{I_W - I_D}\right)] \times \frac{1}{2l} \quad (2.10)$$

where I_S is the intensity of a sample, I_W is the intensity of the sample measured on a Teflon plate, I_D is the intensity of a dark measurement and I_B is the intensity of the sample measured with a black tape. l is the thickness of each transdermal patch.

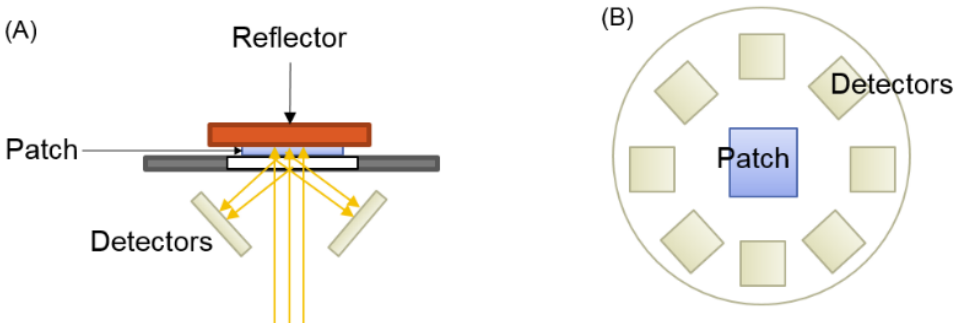

Figure 2.1 NIR measurement setup. A: side view; B: top view.

b. Raman

Raman spectra of the samples was carried out with the Kaiser RXN2®-Hybrid Raman system (Kaiser Optical System, Ann Arbor, MI, U.S.). The light backscattered from the sample was collimated by an objective lens to achieve a 1.5 mm diameter laser spot size. The spectra in the range of 150-1890 cm^{-1} were acquired with a resolution of 4 cm^{-1}. The acquisition time was set at 5 s with 8 co-adds to provide adequate signal compared to noise. Multiple spectra were collected on every patch: four collected on the corners and one taken in the center. Two linear stages driven by a motion controller (Ensemble®, Aerotech Inc., Pittsburgh, PA, USA) and two brushless motors (BMS60, Aerotech Inc., Pittsburgh, PA, USA) accurately located the sampling locations for each sample. Figure 2.2 demonstrates the Raman setup for patch measurements.

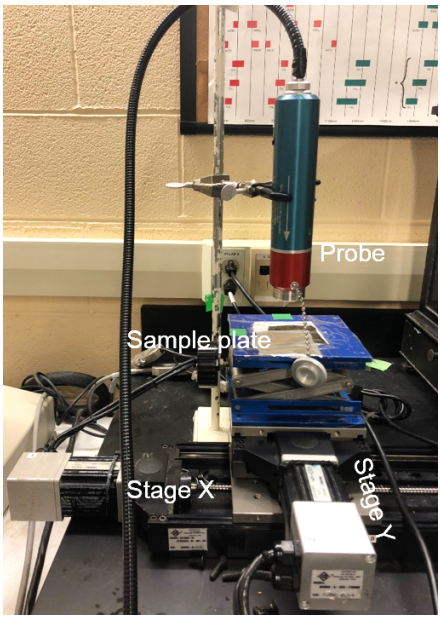

Figure 2.2 Experimental setup of a Raman spectrometer for DIA transdermal patch measurements.

2.2.4.2 Data Preprocessing

Spectral data of both instruments were treated by several preprocessing methods including standard normal variate (SNV), normalization to film thickness and normalization to unit area. The correlation coefficients between the spectra (raw and preprocessed) and patch thickness were compared. A suitable preprocessing method was selected based on the ability of the method to reduce the influence of patch thickness on signal.

2.3 Results and Discussion

2.3.1 Appearance, Thickness and Weight Variation

The non-volatile content of adhesive Duro-Tak® 2052 was 49.60 ± 0.83 % w/w, which was used to determine the amount of drug needed for the calibration design (Chapter 5). All the patches made according to the target formulation were transparent and colorless. The thickness and weight

of patches at the target formulation (23.5% w/w API and 0.55 mm, or P3 in Table 2.1) are shown in Figure 2.3. The variations were within ± 10% of the nominal values.

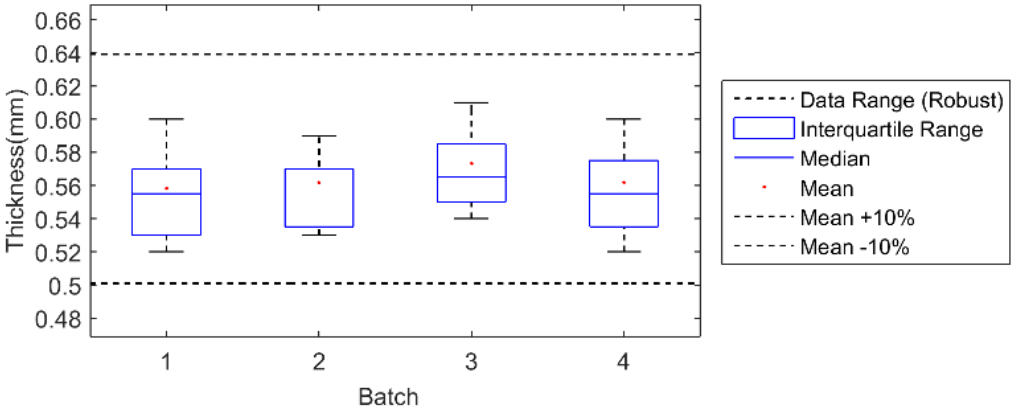

Figure 2.3 Intra and inter batch thickness variations of DIA patches.

2.3.2 Drug Content and Uniformity

The drug content and content uniformity are shown in Table 2.2. Relative standard deviations of the drug contents were below the acceptable values (15 %) specified in USP <905> for uniformity of dosage units in single-unit containers, indicating dose uniformity of the patches was reached.

Table 2.2 A summary of the content uniformity of four batches of DIA patches

Batch	Drug content (%, w/w)	Content uniformity (RSD %) n =10
1	25.9 ± 1.24	4.77
2	23.4 ± 1.16	4.96
3	24.3 ± 1.09	4.49
4	23.9 ± 1.28	5.36

2.3.3 Drug-adhesive Compatibility

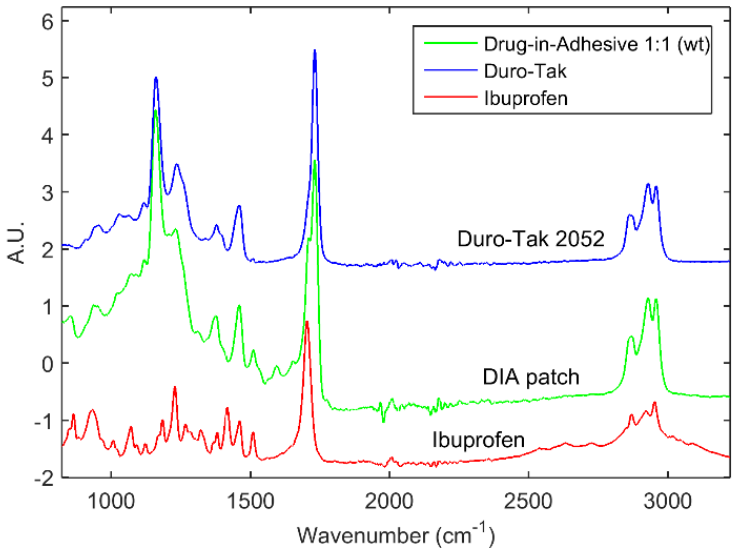

Figure 2.4 FTIR spectra of ibuprofen powder, blank adhesive (Duro-Tak® 2052) and DIA patch composed of 50% w/w ibuprofen. Spectra were scaled to assist visual comparisons.

The FTIR spectra of ibuprofen and Duro-Tak® 2052 are shown in Figure 2.4. The characteristic IR absorption bands of ibuprofen at 1708, 1512, 1452, 1420, 1268 cm^{-1} indicate the presence of C=O stretching, C-C ring vibration, C-H asymmetric bending and C-H scissoring, CH-CO deformation, and C-O stretching.[183] These peaks were all observed without shifts in the presence of adhesive, suggesting ibuprofen is compatible with the adhesive.

2.3.4 Equilibrium Saturation Solubility of Ibuprofen in Duro-Tak® 2052

Table 2.3 Solubility parameters for ibuprofen in a Duro-Tak® system

Model drug	Molecular weight (g/mol)	Density (g/cm^3)	Molar volume (cm^3/g)	Total δ of drug[184]	Total δ of polymer[185]	Estimated drug solubility (%, w/w) [a]	Estimated drug solubility (%, w/w) [b]
Ibuprofen	206.30	1.18	174.83	19.36	21.51	18.89	16.17

a. Calculated using the limiting form of Flory's equation (Equation 2.2)
b. Calculated using regular solution equation (Equation 2.5)

The physicochemical properties and solubility parameter values for the model drug are listed in Table 2.3. Drug solubility in the adhesive patch was dependent on the difference in solubility parameters between the drug and the polymer. The patches loaded with the drug at a

concentration above the equilibrium solubility will recrystallize. The estimated solubility of ibuprofen (+/-) in Duro-Tak® 2052 was 18.89% w/w based on Flory's equation and was 16.17% w/w using the regular solution equation. The solubility calculated using the Flory equation was over-estimated and 16.17% was used moving forward. The Flory equation is not valid when there are specific molecular interactions between drug and polymer.

The crystallization of ibuprofen in patches loaded with varying drug concentrations were observed after six months of storage at 25 °C and 32 % RH. In Figure 2.5, white crystalline drug particles were observed in patches with a drug load equal or greater than 15% w/w. This result was consistent with the solubility estimated from the regular solution equation. However, at concentration greater than 19% w/w, there is a noticeable increase in the amount of the crystals.

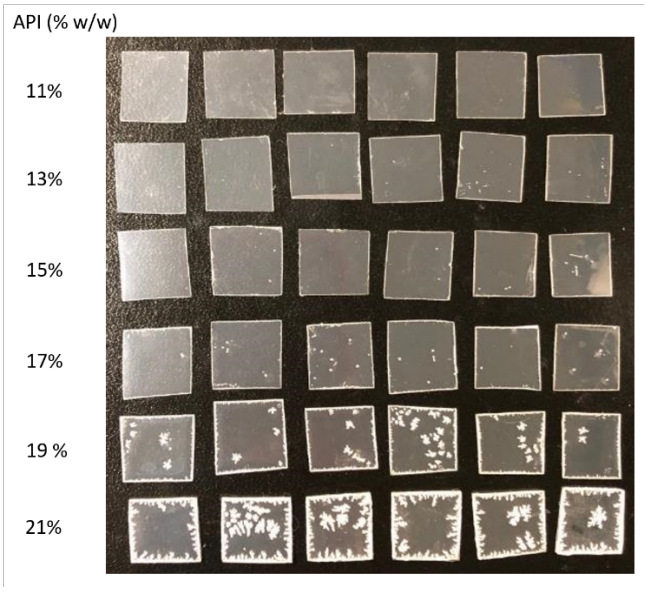

Figure 2.5 A photo of ibuprofen DIA patches with varying drug concentrations. The drug concentrations of the patches from the top row to the bottom row are 11, 13, 15, 17, 19 and 23.5% w/w.

2.3.5 Absence of Crystalline Drug in Freshly Prepared DIA Patches

All the patches freshly prepared according to the target formulation were transparent and colorless. There was no birefringence via a polarized microscope. The XRD diffractogram of a freshly prepared DIA patch is shown in Figure 2.6, along with the XRD pattern of ibuprofen powder. The signal of the freshly prepared DIA patch at 12.4 2θ was also observed in the diffraction patterns of the liner and the backing. The signature XRD pattern of ibuprofen was absent in the diffractogram of the DIA patch, suggesting that either the drug did not crystallize, or the amount of crystallized drug was below the detection limit of the XRD diffractometer. The signal of the patch is very similar to the pattern of the liner. The liner is made of a semi-crystalline material, polyethylene terephthalate (PET).[186]

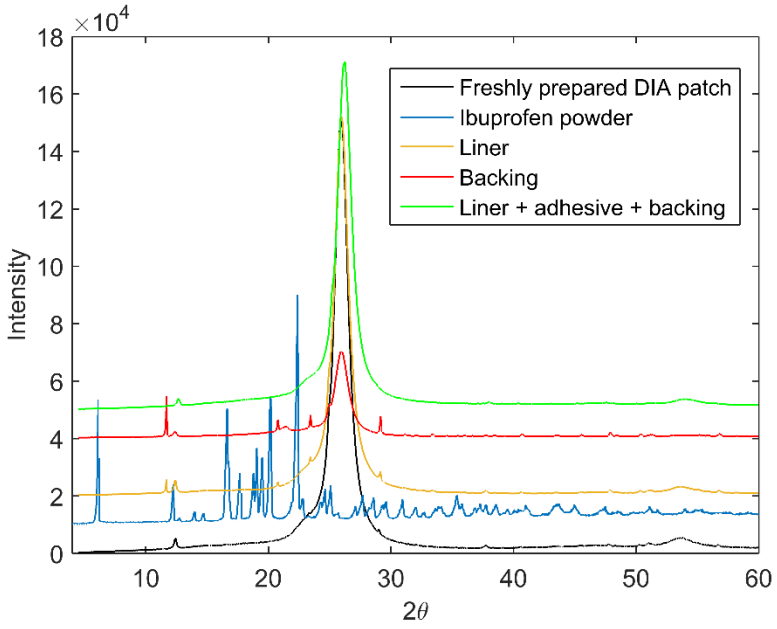

Figure 2.6 XRD diffraction patterns of a freshly prepared DIA patch, ibuprofen powder and patch components.

2.3.6 Distribution of Crystalline Drug

Cross-sections of crystallized transdermal patches were checked under the microscope. Note that the liners were removed from the patches prior to microscopic examination. The

photomicrographs were taken at a magnification level of ×40. In Figure 2.7 (B) and (C), the crystallized drug, shown as the bright areas under the polarized light, were found near the surface of the drug-in-adhesive layer and around the edges of the patches. Inside the patch, the crystallization occurred primarily at the liner-adhesive interface. The bright line is the backing layer of the patch. Along the edges, the irregular surfaces caused by cutting can serve as heterogeneous nucleation sites.

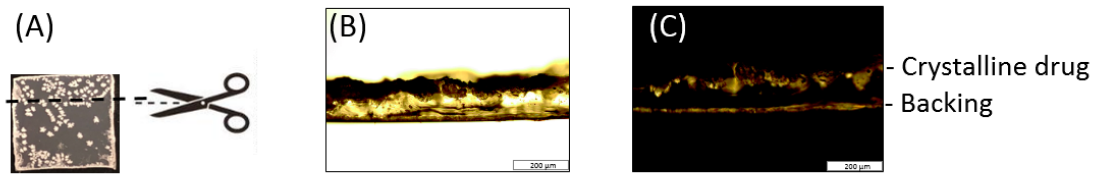

Figure 2.7 A: Schematic illustrating where a film was trimmed for microscopic observation; B: An optical image of the cross-section of a crystallized DIA patch ; C: A polarized light microscopic image of the cross-section of a crystallized DIA patch.

2.3.7 Effect of Thickness on Spectral Signal

2.3.7.1 Effect of Thickness on NIR Signal

The effect of light scattering appears to be less significant in DIA patches comparing to that in turbid media. This is because patches composed of a continuous phase of drug and adhesive contained fewer scattering centers such as crystals and pores. Therefore, Beer's law was used to explain the relationship between the NIR absorbance and thickness of DIA patches:

$$A_i = \epsilon b_i c_i \tag{2.11}$$

where $A_i$and b_i are the absorbance and thickness of i-th sample, ϵ the absorptivity of the analyte, which is wavelength dependent, and c_i is the concentration of the analyte in that sample. Figure 2.8 shows the NIR spectra of patches with thickness varied between 0.40 and 0.60 mm. Based on

Beer's law, the NIR absorbance should increase linearly with the sample thickness. The correlation between the raw NIR spectra and patch thickness is illustrated by the blue curve in Figure 2.9.

An abrupt change in the correlation coefficient at 1100 nm is due to the transitioning of signal recorded from a silicon (400-1100 nm) detector to a lead sulfide (1100-2500 nm) detector in the NIR spectrometer. The correlation between the raw spectra and thickness was greater than 0.7 at most places above 1100 nm.

Several preprocessing methods were explored to reduce the correlation between thickness and NIR spectra. The green curve represents the correlation calculated after the spectra were corrected by the measured patch thickness. The correction involves dividing each spectrum by the thickness value of the corresponding sample. It reduced the correlation to 0.6 from 0.8 at regions above 1100 nm. However, the thickness correction increased the correlation in the spectral region of 600-1100 nm. Normalization to unit area is a preprocessing that divides each spectrum by its norm so that the sum of the absorbance at all wavelength equals to 1. Standard normal variate (SNV) reduces the overall intensity differences between spectra by removing the mean followed by dividing the standard deviation of each spectrum. Normalization and SNV both reduced the correlation between thickness and the NIR signal. The SNV gave a slightly lower correlation (<0.5). The difference across the NIR spectra shown in Figure 2.8 (A) was effectively removed after SNV was applied (see Figure 2.8(B)).

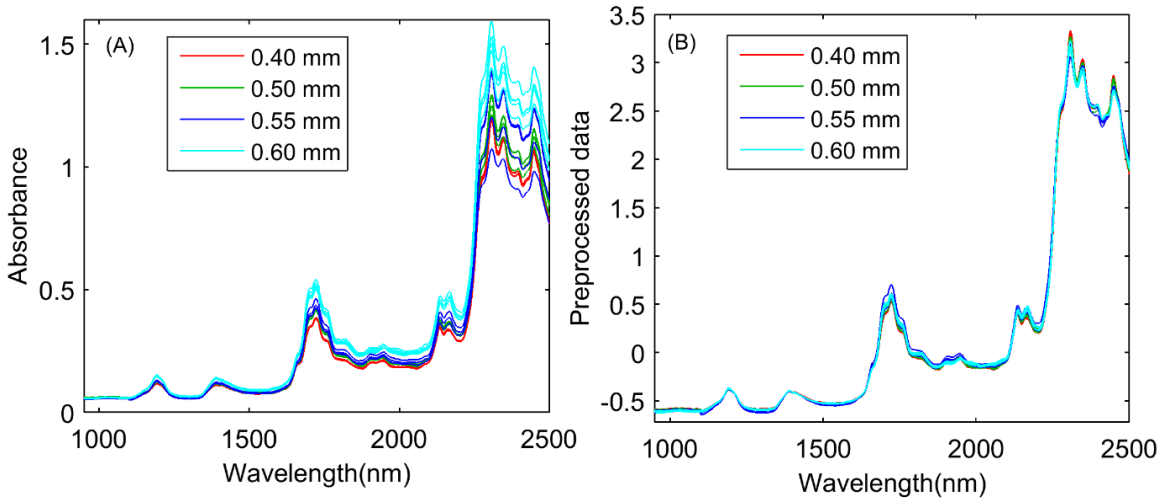

Figure 2.8 NIR spectra of DIA patches with changing thickness. A: raw spectra; B: spectra preprocessed by SNV.

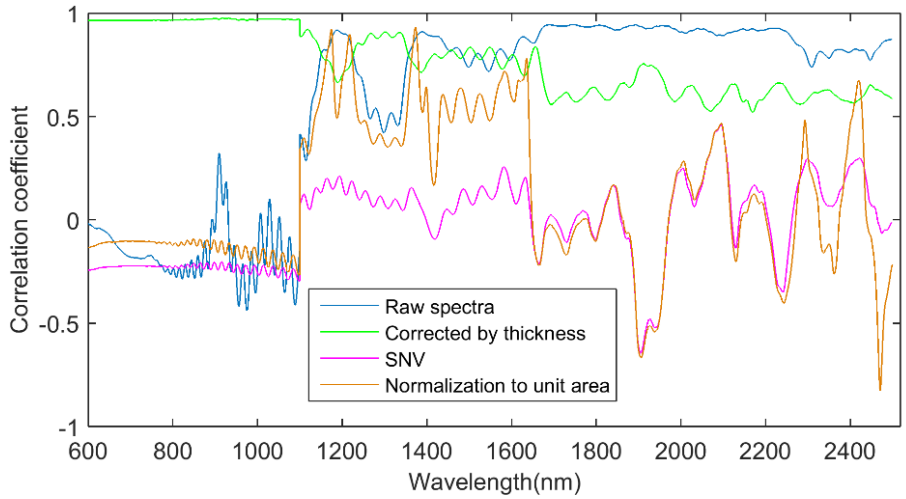

Figure 2.9 Correlation coefficients calculated between the patch thickness and raw or preprocessed NIR spectra.

2.3.7.2 Effect of Thickness on Raman Signal

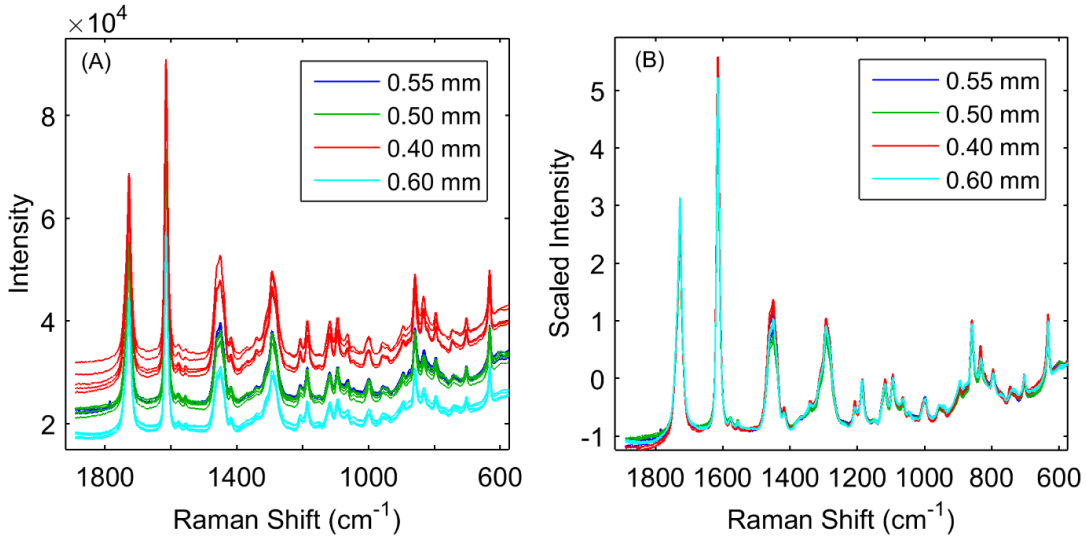

Figure 2.10 Raman spectra of DIA patches with changing thickness. A: raw spectra; B: spectra preprocessed by SNV.

Baseline changes were observed as patch thickness changed. Figure. 2.10 (A) shows the Raman spectra of patches(Table 2.1) with a thickness varying between 0.44 and 0.60 mm. An explanation for the phenomenon is that the sample surface was shifted from the focal plane as the thickness was increased. However, the differences in the intensity were effectively removed by applying spectral preprocessing. Figure 2.10 (B) showed the spectra of patches of different thickness were overlapped after SNV was applied.

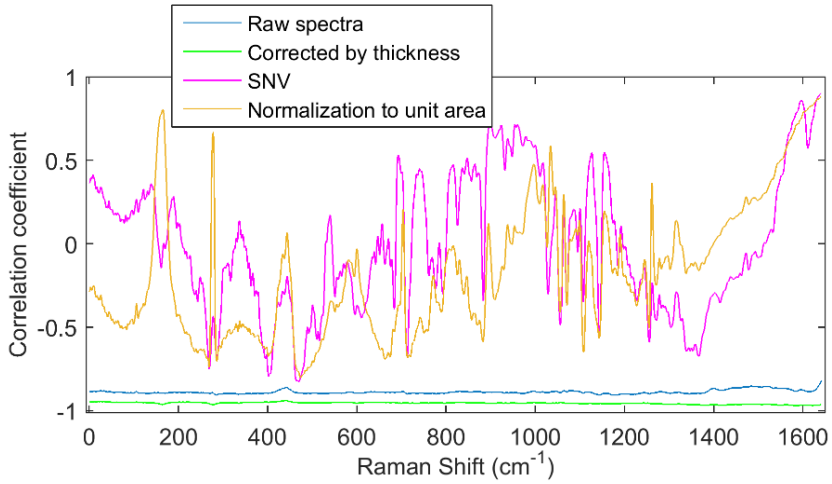

Figure 2.11 Correlation coefficients calculated between patch thickness and raw or preprocessed Raman spectra.

The raw spectra of the patches showed negative correlations with the patch thickness. This observation is illustrated in Figure 2.11. Spectral correction by dividing thickness values did not reduce the spectra-thickness correlation. It enhanced the correlation, which suggests the spectral variation associated with the thickness changes is not a simple linear function of the path length. Normalization to unit area and SNV were used to minimize the scale and baseline differences. The two preprocessing methods led to very similar amounts of reduction in the correlation coefficients. These methods were used for reducing the influence of thickness on signal during the calibration development.

2.4 Conclusions

Ibuprofen transdermal patches were prepared using Duro-Tak® 2052. The prepared transdermal patches were evaluated for drug-excipient compatibility (FTIR), drug content uniformity, weight variations, and distribution of crystalline drug in the patches. The developed formulation demonstrated consistent quality attributes within and between batches. The DIA patches prepared were initially free of crystals, as was confirmed by XRD results. After crystallization reached equilibrium, the crystalline drug was found primarily at the interface between the liner and the DIA layer. The results of these preliminary experiments revealed ibuprofen is supersaturated at 23.5% w/w in the DIA system with a drug solubility of approximately 16% w/w. Both NIR and Raman signal of the transdermal patches were highly correlated with the patch thickness. Proper data preprocessing is required to reduce the influence of thickness on the spectral signal.

Chapter 3 : Determination of Analytical Feasibility for Crystalline Content Quantification in DIA Patches.

3.1 Background and Introduction

Physical mixtures of crystalline and amorphous drug are frequently used to build quantitative calibrations to determine crystalline content of APIs in solid dispersions. Unlike powder samples that can be prepared by blending, the adhesive polymer is very tacky, making the blending of adhesive and drug difficult and unlikely to result in appropriate dispersion of the drug particles. Mixing the crystalline drug and the adhesive polymer requires additional mechanical force or heat to blend the materials, which are likely to change the physical state of the solids.

The problems described above can be solved by a method that separately prepares film layers containing different phases of the API and combines them. This preparation method helps to achieve a known percent crystallinity that is needed for calibration, because the quantities of the crystalline and the amorphous drug are known at the time of preparation.

This chapter describes a coating-based method for spiking crystalline API into DIA patches. The suitability of spiked samples to be used as calibration samples for crystalline content quantification was demonstrated. The samples spiked with drug crystals and the samples naturally recrystallized must have similar physiochemical properties as well spectral responses. Spiked samples were made by spraying accurately measured amounts of crystalline drug onto liners via spray coating of an aqueous drug suspension. Samples with naturally formed crystals were prepared by dissolving ibuprofen in the Duro-Tak® adhesive at a concentration above the equilibrium solubility and allowing the ibuprofen to recrystallize.

The geometric distribution of the spiked crystals in the spiked samples was characterized and compared with the naturally crystallized samples in Chapter 2. In addition to having similar

physiochemical properties, the spiked samples must remain physically stable over a period long enough for solid-state characterization. The crystal growth (or dissolution) of the spiked crystals in DIA patches were observed by optical microscopy to determine the length of time during which recrystallization (or dissolution) of drug was insignificant. The spectral similarity between the spectra of spiked and naturally recrystallized samples was demonstrated in Chapter 4.

The coating uniformity of calibration samples is always important, but it is particularly important when the analytical technique samples only a fraction of the available patch area. When the spot size of analytical tool is larger than the size of a patch and the thickness of the patch is less than the path length of the light beam, the sampled volume is limited by the size of the patch. However, when the spot size is smaller than a patch, a lack of coating uniformity may increase the measurement uncertainty. Therefore, a study to determine the coating uniformity of spiked crystals was conducted.

Both NIR spectroscopy and Raman spectroscopy are potential techniques for quantitative characterization of crystalline phase in transdermal patches. However, a comparison of the techniques for TDDS, based on figures of merits such as sensitivity, specificity and suitability of such methods has not been reported. This chapter demonstrates the analytical feasibility of vibrational spectroscopy (NIR and Raman) for quantitative study of ibuprofen crystallization in Duro-Tak® 2052. Instrumental sensitivity towards the two physical forms (supercooled liquid and crystalline solid) of the drug were measured. The sensitivity was defined as the change in signal intensity per unit change of concentration. The depth of penetration of the excitation laser beam in DIA patches was measured. Adequate sampling volume must be ensured for representative sampling. Optimization of measurement settings was performed. The goal was to find the best measurement scheme that maximizes signal intensity while retaining a relatively short

measurement time. The chapter develops the analytical foundations that are used in the next chapter.

3.2 Experimental Methods

3.2.1 Preparation and Characterization of Spiked Samples

3.2.1.1 Materials

The drug and adhesive were dissolved and cast onto backing layers according to the method described in Chapter 2. Crystalline drug particles were coated onto liners. Patches from the three levels of crystalline contents (3 replicates per batch) were selected to represent the low, medium and high levels of crystallinity. The backing layer coated with dissolved drug and the liners spiked with crystals were combined to prepare patches with desired crystallinities (Table 3.1).

Table 3.1 Composition of calibration and test sets using a full factorial design

Sample	Crystallinity (%)	Crystalline-Sprayed API (%, w/w)	Solvated API (%, w/w)	Adhesive Dry Weight (%, w/w)
C1	4.0	1.0	23.5	75.5
C2	17.5	5.0	23.5	71.5
C3	25.4	8.0	23.5	58.5
A1	0.0	0.0	17.0	83.0
A2	0.0	0.0	23.5	76.5
A3	0.0	0.0	30.0	70.0

3.2.1.2 Preparation of Liners Coated by Crystalline Drug

Ibuprofen powders were passed through a sieve with openings of 250 μm. Agglomerates were removed to reduce the risk of blocking the spraying nozzle during coating of the suspension. A 1.5% w/w ibuprofen aqueous suspension was prepared using de-ionized water. The suspension

was homogenized on a magnetic stirrer overnight. The suspension was sprayed onto pre-weighed 3cm-by-3cm liners to achieve desirable coating weights using a fluidized bed spraying gun and a peristaltic pump. The nozzle of the spraying gun has an opening of 1.5 mm to allow for the passage of drug suspension. The air pressure was set at 1.0 bar, or 10^5 Pascal. The spraying rate was set at 3 g of suspension per min. A hot plate (45 °C) was placed at the bottom of the liner to facilitate the drying of water. The distance between the spraying nozzle and the hot plate was 36 cm. The setup of the spraying station is demonstrated in Figure 3.1. The amount of drug sprayed increased linearly with the coating time. The empirical relationship is:

$$m = 0.050t \tag{3.1}$$

where m is the mass (mg) of the drug sprayed and t is the coating time in seconds. The relationship was used to determine the coating time used for coating a crystalline content on a liner. The mass of the drug sprayed is dependent on the actual spraying settings such as air pressure, pump rate and homogeneity of the drug suspension. During coating, all these settings were kept constant.

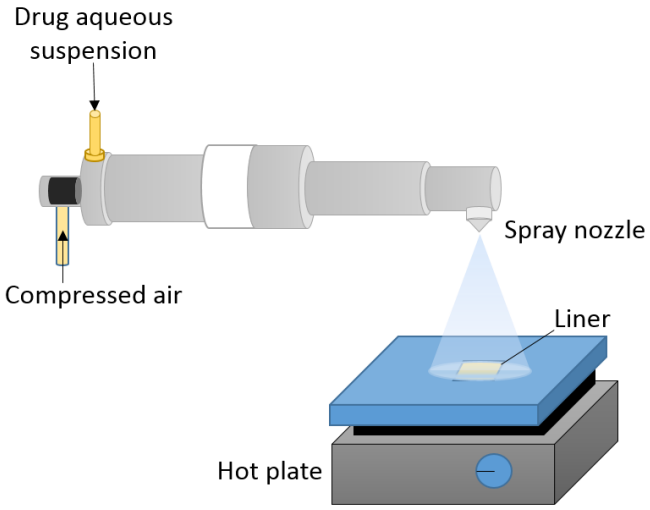

Figure 3.1 Schematic demonstrating the powder coating process. A drug suspension containing 1.5% w/w ibuprofen in water was sprayed onto liners. The water was dried by compressed air and a hot plate set at 45 °C.

3.2.1.3 Physical Stability of Spiked Crystalline API

A drug-bearing adhesive was coated onto the powder coated side of a liner to form a drug-in-adhesive patch. The crystal growth of the spiked crystalline particles was monitored by an optical microscope every 10 min over a period of 150 min following the lamination. The procedure to determine the induced crystal growth rate is illustrated in Figure 3.2. The optical image shown in Figure 3.2 (A) was converted to a gray image shown in Figure 3.2 (B). The histogram demonstrating the distribution of the pixels in the grayscale image was used to select the cutoff value for converting the gray image to a binary image. The cutoff value is indicated by the arrow in Figure 3.2 (D). The cutoff value marks the maximum change in the slope of the frequency distribution of the grey image. In the binary image of Figure 3.2 (C), the white and the black pixels represent crystals and the background, respectively. The void spaces within each particle were switched to white pixels (Figure 3.2 (E)) as the pixels within the circumstances of each particle is a part of the crystal. The conversion from an optical image to a binary image allows the number of pixels occupied by the crystalline drug to be counted. T-tests (α=0.05) were used to test the statistical significance between mean areas of crystals at two successive time points. The time point at which projected area was significantly larger than that of the picture taken at the initial time point was the crystallization induction time (t_{ind}). The spectroscopic measurements were performed within the time window of 0-t_{ind}.

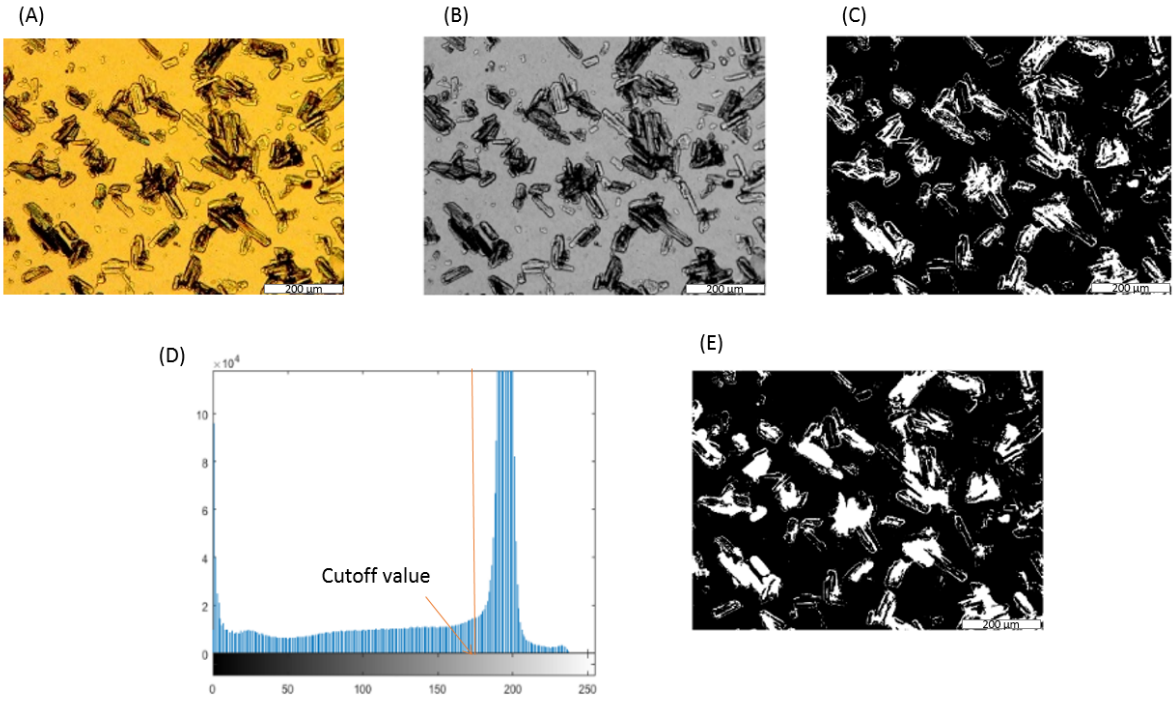

Figure 3.2 Conversion of an optical image to a binary image for calculating the area representing the drug crystals. A: An optical image; B: A grey image; C: A binary image; D: The frequency distribution of pixel intensity of the binary image; E: Black pixels inside the crystalline particles were switched to white pixels.

3.2.1.4 Coating Uniformity

The coating uniformity of the sprayed crystalline particles was evaluated by an optical microscope using a magnification of 40×. This magnification was selected because the size imaged was the same as the size probed by the Raman system. Binarization was conducted using the same procedure described in 3.2.1.3 to calculate the area representing the crystalline drug. The RSDs of the crystalline drug areas were calculated from four replicates at each concentration. Only liners with RSDs less than 10% were selected moving forward.

3.2.2 Determination of Analytical Feasibility

3.2.2.1 Determination of Penetration Depth of the Raman System

The penetration depth of the laser beam in the sample is a determinant of the sampling volume. Raman spectroscopy have been shown to have limited penetration in solid turbid media.[187] However, in transparent samples such as DIA transdermal patches, the light will penetrate into deeper layers without significant elastic scattering. The feasibility of the Raman analyzer to probe the whole sample volume was established experimentally by observing the signal change in a 10-layer patch system. This method keeps the sample thickness and focal distant constant.[188] A polytetrafluoroethylene (PTFE) film was sandwiched between 10 layers of DIA patches containing 23.5% w/w of ibuprofen in Duro-Tak® 2052. The signal from the PTFE was tracked as the PTFE film was moved from the top to the bottom of the pile (see Figure 3.3).

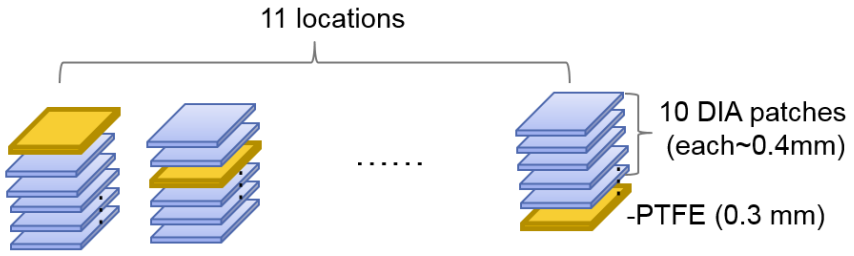

Figure 3.3 Schematic demonstrating samples used for depth of penetration determination.

3.2.2.2 Determination of Instrument Sensitivity

a. Instrument Sensitivity

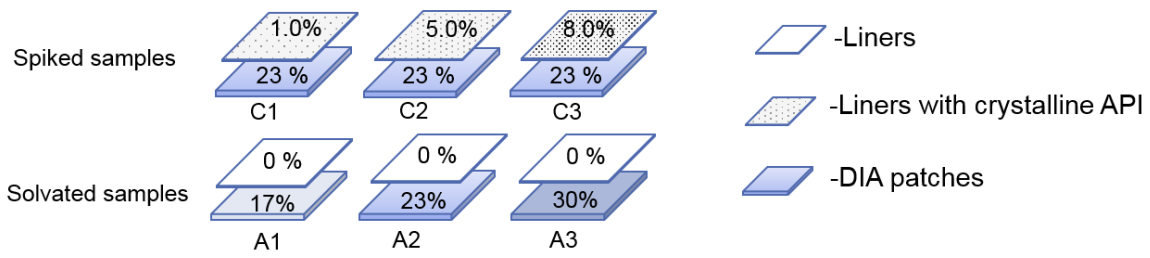

Figure 3.4 Schematic demonstrating the contents of crystalline and solvated drug of spiked patches used to determine instrumental sensitivity.

Analytical sensitivity was calculated as the signal change per unit change of analyte concentration. The crystalline content was varied by 1.0, 5.0 and 8.0% w/w based on a 120 mg patch. The crystalline drug was coated according to the method described in 3.2.1.2. Three replicates were made at each crystallinity level. To determine the sensitivity of the instruments for detecting changes of crystallinity when drug was dissolved in the adhesive matrix, the solvated API contents were kept constant (23.5% w/w). The composition of spiked samples is illustrated in the upper panel of Figure 3.4. The three crystalline levels are designated in Figure 3.4 by samples C1, C2 and C3. The spectral responses were recorded by the NIR and the Raman systems. The sensitivity was determined as the mean spectrum difference between samples with changing crystallinity divided by the difference in crystalline contents:

$$Sensitivity\ to\ crystal = mean\left(\frac{|X_{c2}-X_{c1}|}{\Delta Y_{C21}} + \frac{|X_{c3}-X_{c2}|}{\Delta Y_{C32}} + \frac{|X_{c3}-X_{c1}|}{\Delta Y_{C31}} \right) \quad (3.2)$$

where X_{ci} is the mean spectrum of a sample with a crystallinity of C_i, e.g. X_{c2} represents the mean spectrum of samples with a crystallinity of 5.0% w/w. ΔY_{Cij} is the difference in the crystalline content of drug between the ith sample and the jth sample.

Similarly, the sensitivity of analytical tools to changes in the solvated drug (metastable form) was determined by measuring DIA patches with drug dissolved in the adhesive at

concentrations varying from 17.0 to 30.0% w/w. The compositions of samples A1, A2 and A3 are illustrated in the bottom panel of Figure 3.4. The sensitivity for the solvated API is calculated as follows:

$$Sensitivity\ to\ solvated\ API = mean(\ \frac{|X_{A2}-X_{A1}|}{\Delta Y_{A21}} + \frac{|X_{A3}-X_{A2}|}{\Delta Y_{A32}} + \frac{|X_{A3}-X_{A1}|}{\Delta Y_{A31}}) \qquad (3.3)$$

where X_{Ai} is the mean spectrum of a sample with a particular solvated API content A_i, e.g. X_{A1} represents the mean spectrum of samples with a drug content of 17 % w/w. ΔY_{Aij} is the difference in the solvated drug content between the ith and the jth samples.

A univariate sensitivity was calculated as the sum of sensitivity across a certain wavenumber or wavelength region. Univariate sensitivity of the Raman system or the NIR system to two forms of ibuprofen were calculated. The results were compared with the sensitivity of an XRD method.

b. Effective Resolution

Effective resolution (γ) is another useful measure of relative sensitivity of dissimilar analytical techniques. It is the ratio between the vector of sensitivity and the vector of noise:

$$\gamma = (\frac{SEN}{Noise})^{-1} \qquad (3.4)$$

The effective resolution has a unit of concentration. It represents the minimum discernible concentration attained by the analytical system. It allows the comparison of analytical methods regardless of the specific technique, equipment and scale. [189] The noise of the measurements is calculated from the standard deviations of repeated scans of the same sample. Experiments were repeated for all concentration levels (A1-A3, C1-C3).

3.2.2.3 Instrument Selectivity

PCA analysis was used as a discriminant tool to visualize the separation of the spiked and solvated samples in PC space. All the samples shown in Figure 3.4 were measured by the NIR system and the Raman system. The wavenumber region 676-1225 cm^{-1} was selected for Raman and 1550-2250 nm was selected for NIR because these regions contain the signature peaks of the API. NIR and Raman data were both preprocessed with SNV and mean-centering. For each analytical technique, a PCA model was constructed. The number of PCs were determined from the percent variance explained by the PCA models. The incorporation of appropriate number of PCs allowed the PCA models to explain more than 95% of the spectral variance for each technique. The angle between the center planes of the two clusters that separately contain A1-A3 and C1-C3 expressed the orthogonality between the two sample sets in the PC space. The two clusters were fitted by 95% confidence ellipsoids. More specifically, the angles between the normal vectors of the confidence ellipsoids were calculated and used to express the degree of independence between the samples A1-A3 and samples C1-C3.

Selectivity expresses the extent to which a particular method can be used to determine a particular analyte in mixtures or matrices without interferences from other components of similar behavior.[190] A PLS model was developed from the spectra of the spiked samples (C1, C2 and C3) to predict the crystalline contents of samples with varying solvated API contents (17, 23 and 30% w/w). If the PLS model accurately determines the crystalline content in the presence of variations of solvated drug content, the model is selective to the crystalline component. The samples used in this part of study is shown in Figure 3.5.

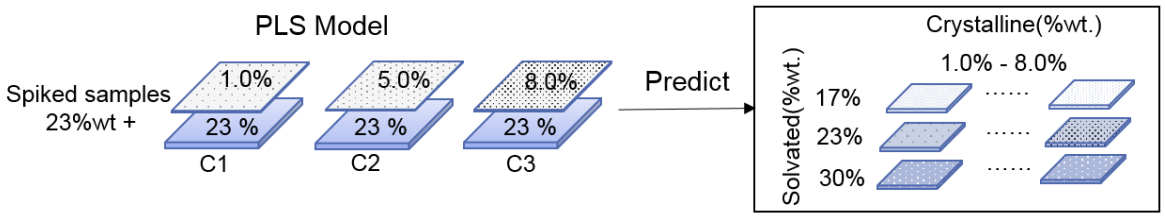

Figure 3.5 Schematic demonstrating the compositions of patches used to determine instrument selectivity.

One-way ANOVA was used to determine if there is any statistical difference between the predicted crystalline contents of the patches with different solvated API contents. The statistical tests used a P-value of 0.14 for drawing statistical significance using multiple t tests. The type I error rate for multiple t-tests is inflated as the number of comparisons increases. Therefore, a corrected type I error was used instead:

$$\bar{\alpha} = 1-(1-\alpha)^m \tag{3.5}$$

where α is type I error for an independent comparison and α=0.05, m is the number of comparisons.

3.2.2.4 Sample Measurements

a. Raman and NIR measurements

The NIR and Raman measurements of transdermal patches were carried out using the setups demonstrated in Section 2.2.4.1. Each sample was repeatedly scanned for three times with and without repositioning to estimate the reproducibility and repeatability of the method. One NIR spectrum was collected for each patch. The spot size of the NIR system (17.5 mm) was larger than the size of a patch. The Raman system has a spot size of 1.5 mm, which is smaller than the size of a sample. Therefore, five spectra were collected on one patch: four collected on the four corners and one taken in the center. The obtained spectra were averaged to give one spectrum per sample.

b. XRD measurement

Diffraction data of transdermal films were collected using an X'Pert Pro MPD system (PANalytical B.V., Almelo, the Netherlands) in Bragg-Brentano reflection mode, equipped with a Cu anode ($\lambda = 1.5406$ Å), an elliptical mirror, and an X'Celerator^{TM} detector. The operating voltage and amperage were 45 kV and 40 mA. Samples were mounted flat on a ring holder. Samples were rotated throughout the experiment to allow for full volume interrogation. Irradiation time was set to 60.05 s per step with an angular step size of 0.017 °2θ over a range of 2 to 60 °2θ.

3.3 Results and Discussion

3.3.1 Coating Uniformity

The homogeneity of the coated crystalline drug particles was examined. Images of patches with crystalline content of 1.0, 2.5, and 5.0% w/w are shown in Figure 3.6. The relative standard deviation was 6.72, 5.37, and 6.79% for patches with crystalline level of 1.0, 2.5, and 5.0% w/w, suggesting uniform coating of the crystalline particles was achieved.

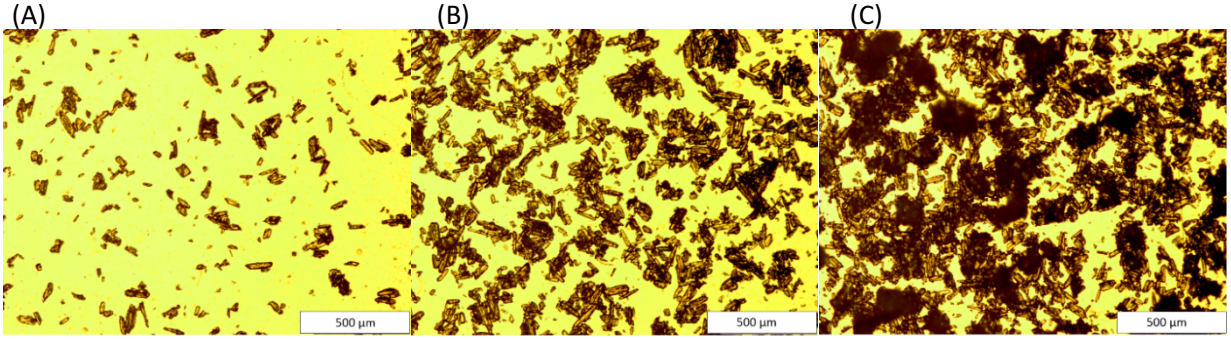

Figure 3.6 Microscopic photos of patches with A: 1.0% w/w; B: 2.5% w/w; C: 5.0% w/w sprayed crystalline API.

3.3.2 Physical Stability of Coated Patches

The crystal growth induced by the spiked crystalline API in the 23.5% w/w DIA patches was revealed by image analysis. The change of area taken up by the crystals as a function of time post lamination is illustrated in Figure 3.7. In the first 40 mins, there was a minimum change of the area attributed to the crystalline API. From 40-150 min, the area of the crystals increased. The crystallization induction time was determined to be about 50 min. The area after this time point was significantly greater than that of the initial time point. The result suggested all analytical measurements should be conducted within the crystallization induction time, which is about 40-50 min.

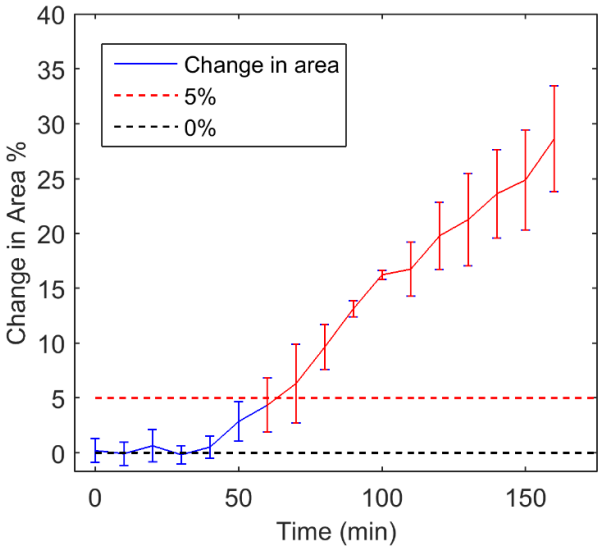

Figure 3.7 Crystal growth of spiked drug represented by a change in the area of the crystalline particles.

3.3.3 Penetration depth of the Raman System

Depth of penetration is a measure of how deep an electromagnetic wave penetrates a sample. It is critical for determining where the information is generated from the sample. Penetration depth helps to select the appropriate sampling strategy. If penetration depth is large, whole volume sampling can be achieved without sampling from both sides of the samples.

Polytetrafluoroethylene (PTFE) was used to measure the penetration depth of laser beam in DIA patches. Polytetrafluoroethylene has a few sharp and resolved peaks that are not overlapped with the components of the DIA patches. The signal intensity of PTFE reduces with an increasing number of patches placed between the PTFE and the probe. The Raman spectra of PTFE and stacked films are illustrated in Figure 3.8. Peaks of the PTFE film at 734 and 1381 cm^{-1} were selected for their high intensities. Additionally, the DIA patches do not present any interference in these regions.

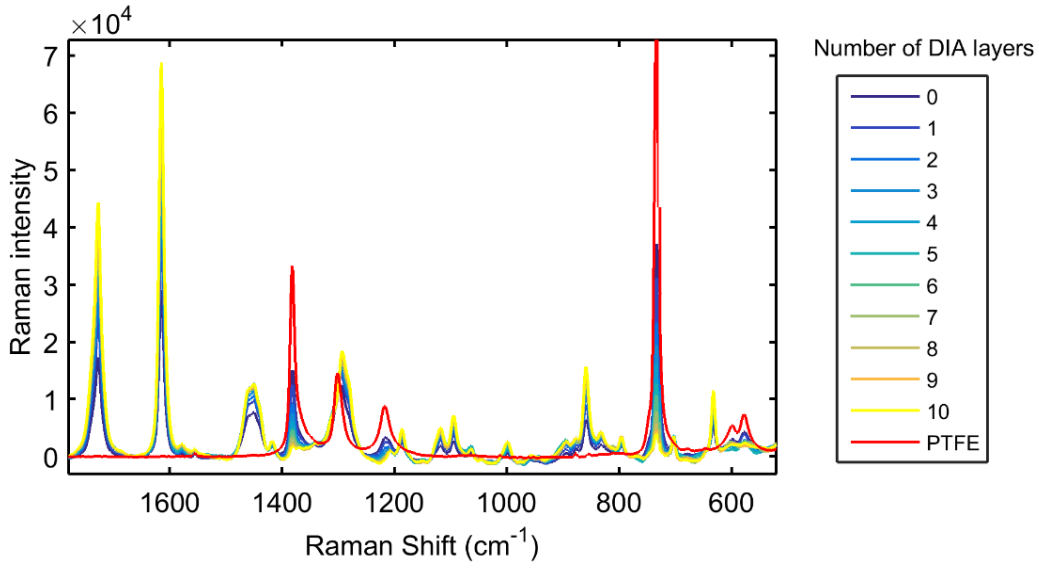

Figure 3.8 Raman signal of a PTFE film overplayed with 10 DIA patches.

The signal of the PTFE film decreased when more DIA layers were added. The intensities of peaks at 734 and 1381 cm^{-1} were normalized by the maximum intensities of the peaks, i.e. when the PTFE was on the top of the pile. The resulting ratios shown in Figure 3.9 decreases with the thickness. In depth of penetration studies, the signal intensity is often found to decrease with the thickness of the sample until it reaches a plateau, which signify the light can no longer penetrate the sample. However, the ratio has not reached a plateau in Figure 3.9; whereas the normalized intensity is close to zero at the highest overlayer thickens (10 layers). Adding DIA layers would

not further reduce the signal from the PTFE film. The Raman signal can be detected through 8-9 layers of DIA films. The information depth was evaluated using the point where the substrate signal was reduced to 1/e or 37%. The information depth was estimated to be about 1.6-2.0 mm for the Raman system, which is much greater than the thickness of a DIA patch (0.4-0.6mm). Therefore, it was concluded that the Raman system can be used to probe an entire patch.

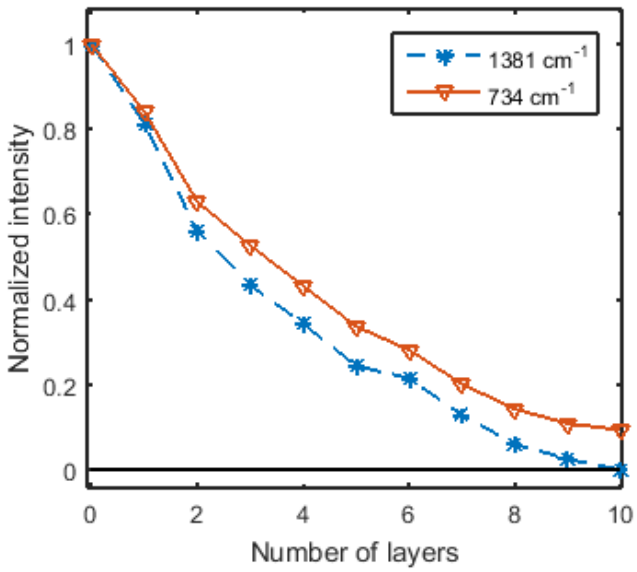

Figure 3.9 Intensity of PTFE at 734 and 1381 cm^{-1}. The intensity was normalized to the spectra of films when the PTFE was placed on top of 10 layers of DIA films.

3.3.4 Analytical Sensitivity

3.3.4.1 NIR System

a. Sensitivity to crystalline and solvated API

The NIR spectra of DIA patches with 17 to 30% w/w of dissolved ibuprofen (samples A1-A3) can be found in Figure 3.10 (A). There was an increase in the overall NIR absorbance due to the increase of API concentration in DIA patches. This increase is consistent with the Beer's law. The difference spectra of patches with different solvated API contents, along with the spectrum of

supercooled ibuprofen, are displayed in Figure 3.11 (A). Similarities between the difference spectra and the spectrum of the supercooled liquid of ibuprofen can be observed. Meanwhile, increases in the crystallized API content not only increased the NIR absorbance around the peaks at 2200 nm, it also led to a decrease in the baseline near 1900-2100 nm. The baseline decrease was possibly caused by the increased backscatter from the crystals, causing the absorbance to decrease. However, it is not clear why the phenomenon was most pronounced in this wavelength region. The baseline decrease is shown in Figure 3.10 (B).

The change in NIR signal per 1% w/w change of crystalline or solvated API is demonstrated in Figure 3.12 as a function of wavelength. The extent of variation of NIR signal due to the crystalline API content is greater than that due to the solvated API. The univariate sensitivity, or the sum of sensitivities across all wavelength, for the solvated and the crystalline API are listed in Table 3.2. Note that the sensitivity to crystalline API is partially negative due to the baseline variations. The absolute values were used to calculate the univariate sensitivity. The ratio of the sensitivity between the two phases is about 2.66. Overall, the NIR system is more sensitive to the crystalline drug compared to the solvated drug.

Table 3.2 A summary of univariate sensitivity and effective resolution for the NIR, Raman and the XRD systems

	NIR		**Raman**		**XRD**	
	Sensitivity $\times 10^4$	γ (%, w/w)	Sensitivity $\times 10^4$	γ (%, w/w)	Sensitivity $\times 10^4$	γ (%, w/w)
Variables	2085-2225 nm (280)		667-946 cm^{-1}(280)		16-20 ° (280)	
Solvated	2.77	0.41	1.56	1.86	NA	
Crystalline	7.36	0.31	5.34	0.69	1.20	5.27

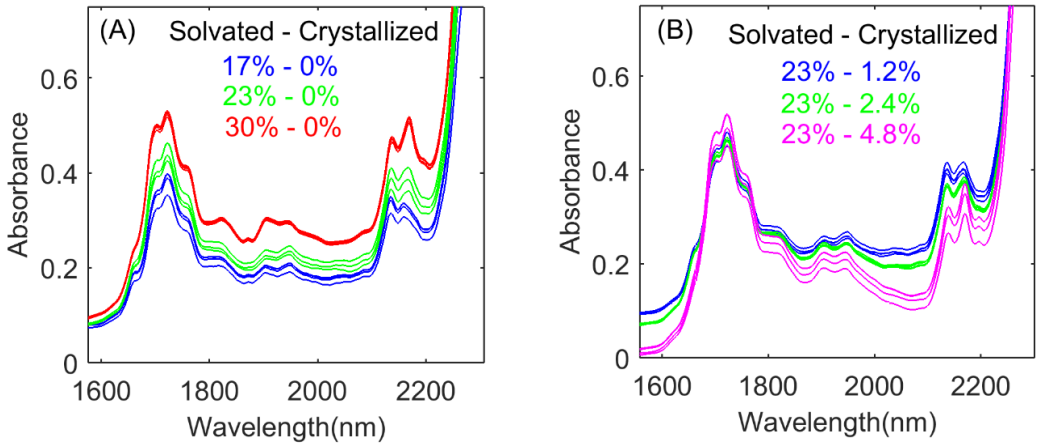

Figure 3.10 NIR spectra of DIA patches with A: solvated API; B: crystalline API. Concentrations on the left column indicate the solvated drug contents and concentrations on the right column are the crystalline drug contents.

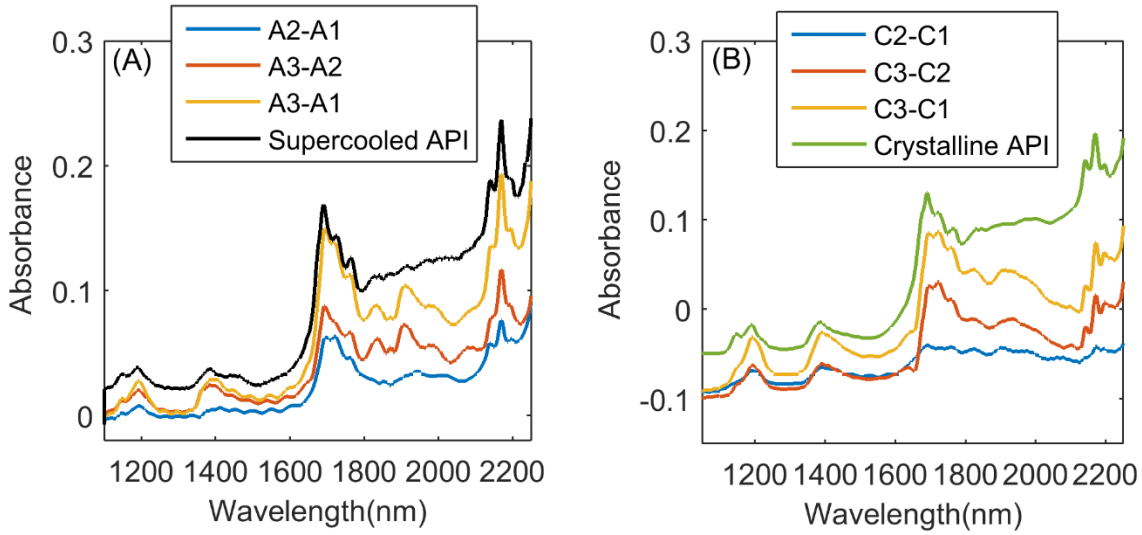

Figure 3.11 A: Difference between NIR spectra of samples A1, A2 and A3; B: Difference between the NIR spectra of samples C1, C2 and C3.

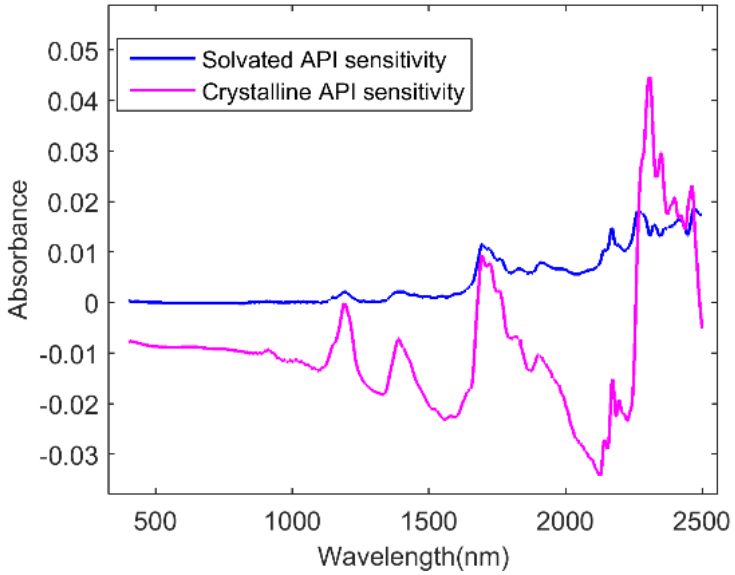

Figure 3.12 Sensitivity vectors of the solvated API and the crystalline API determined from difference spectra shown in Figure 3.11.

b. Effective Resolution

The NIR system has shown good repeatability. This is demonstrated as a low spectral noise obtained by measuring patch samples repeatedly without repositioning. The standard deviations of the repeated scans were plotted for the patches with solvated API and the crystalline API in Figure 3.13. The noise level of the samples with spiked crystalline API is a little higher than that for with solvated API, probably because the presence of the crystalline particles caused a greater extent of variations in the light scattering. The noise was particularly inflated at the wavelength region of 2200 to 2500 nm.

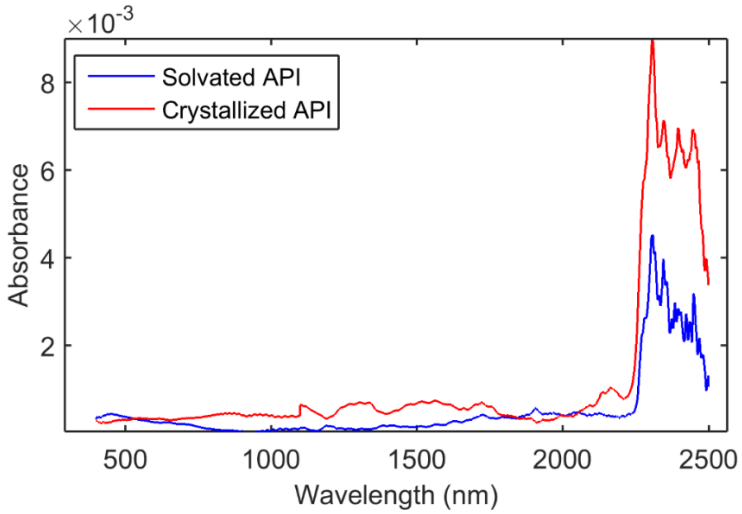

Figure 3.13 Standard deviations of NIR spectra collected from patches with solvated API (23% w/w) and crystalline API (5.0% w/w).

The ratios between the sensitivity (Figure 3.12) and the noise vectors (Figure 3.13) are illustrated in Figure 3.14. The effective resolution is the inverse of the sensitivity-to-noise ratio. The wavelength with sensitivity to noise ratio lower than 0.5 were excluded because the inverse approaches infinity as the sensitivity to noise becomes increasingly small. The effective resolution of the NIR system is lower than 1% w/w for the entire wavelength range. Therefore, the NIR system is sensitive to both the crystalline and the solvated API.

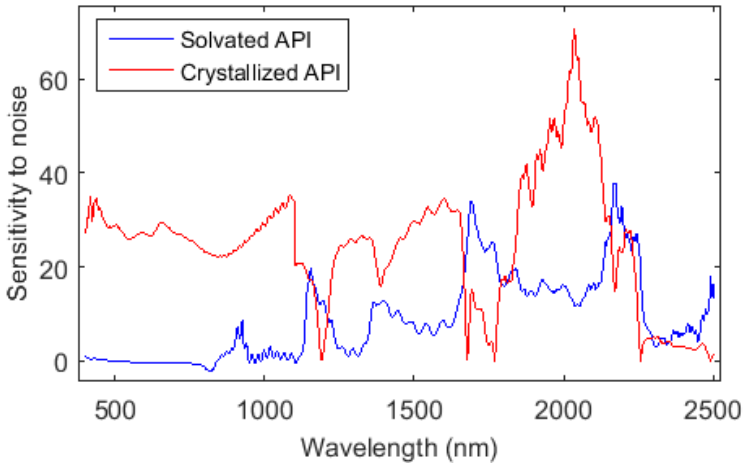

Figure 3.14 Sensitivity to noise ratio of the NIR system to different API phases.

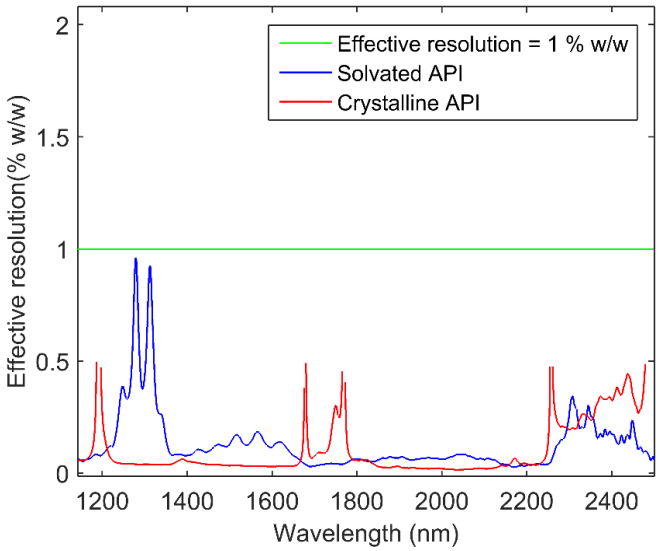

Figure 3.15 Effective resolution of the NIR system to changing crystalline and solvated API contents (The regions where sensitivity to noise ratio lower than 0.5 was excluded).

3.3.4.2 Raman System

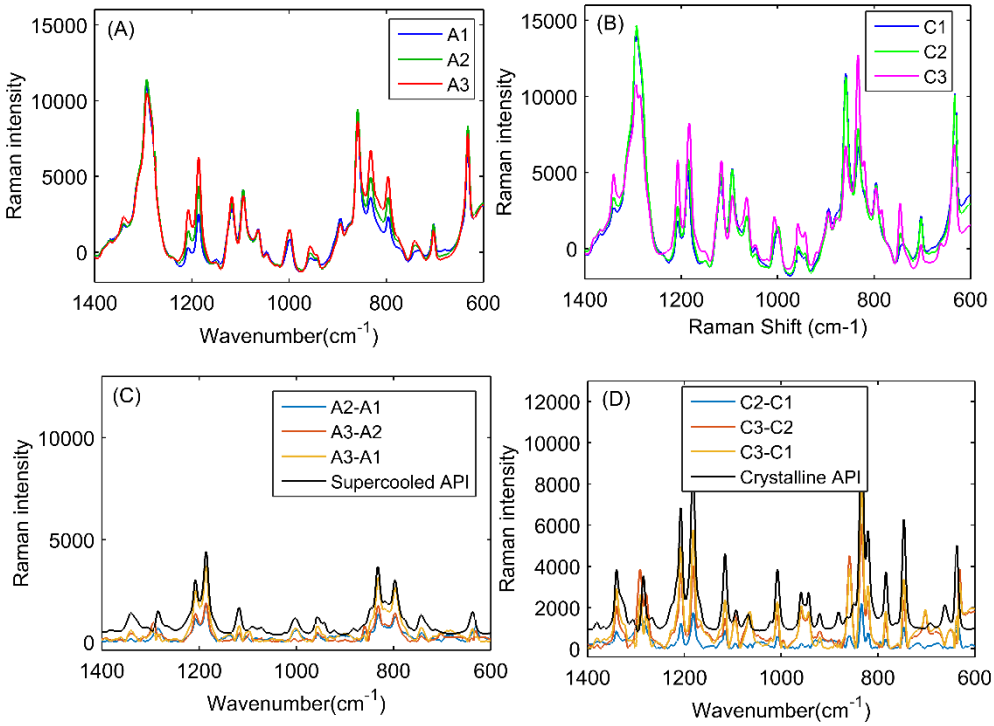

Figure 3.16 A: Raman spectra of DIA patches with solvated API; B: Raman spectra of DIA patches with different levels of crystalline API; C: Difference between Raman spectra of samples A1, A2 and A3; D: Difference between Raman spectra of samples C1, C2 and C3.

The Raman spectrum of the pure crystalline phase of the API presents information about the long-range order of molecules. This can be seen in Figure 3.16 (B). Peaks at 1208, 833, 821, 784, 746 cm^{-1} are related with the changes in crystalline drug content. Comparatively, changes in the solvated API concentration only led to subtle changes of Raman signal in the region near 1200 and 900 cm^{-1}(Figure 3.16 (A)). The difference between spectra of samples with different concentrations are shown in Figure 3.16 (C) and (D). Figure 3.16 (D) revealed some overlapping peaks between the spectral difference across samples C1-C3 and the pure crystalline ibuprofen. The similarities between the spectral difference across samples A1-A3 and the spectrum of the supercooled API is demonstrated in Figure 3.16 (C).

The sensitivities per 1% w/w change of crystalline or solvated content is shown in Figure 3.17. Overall, the Raman system is more sensitive to the crystalline drug than to the solvated drug. The ratio of the sensitivity between the two phases is about 6.4.

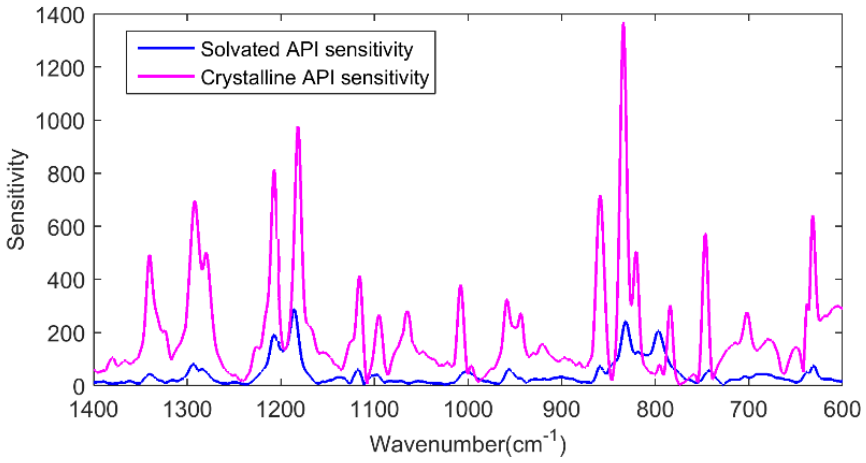

Figure 3.17 Sensitivity of solvated API and crystalline API determined from difference spectra

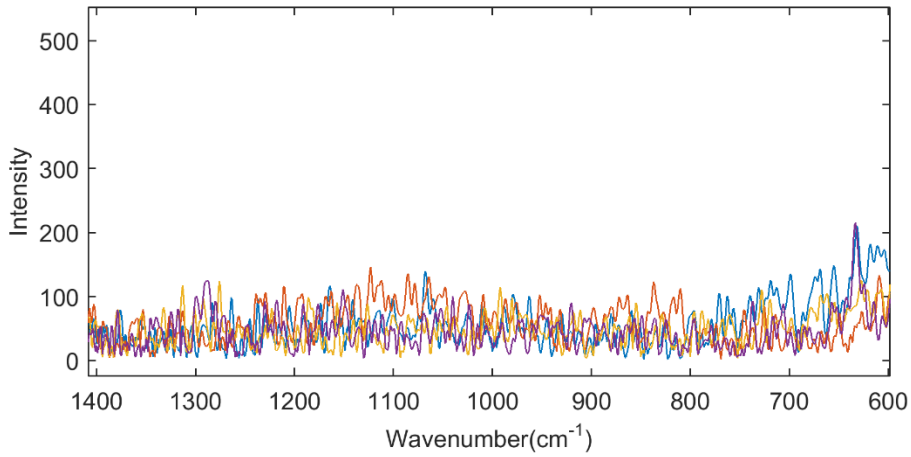

Figure 3.18 Noise profile of the Raman system collected from DIA patches with a crystalline content of 2.4% w/w.

The instrumental noise is characterized by the pooled standard deviation of the spectra obtained from repeated scans of the samples loaded with 23.5% w/w solvated API and 2.4% w/w crystalline API for 6 times. The noise is consistent across the wavenumber range under evaluation, as is shown in Figure 3.18. The noise profile is used to normalize the sensitivity associated with the Raman data to calculate the minimum discernible concentration (γ^{-1}), which is referred to as effective resolution.[191] The ratios between the sensitivity to noise at all wavenumbers are illustrated in Figure 3.19 (A) for the two physical forms of the API. The higher the ratio, the more likely the API can be determined at a given wavenumber. The effective resolution is the inverse of the sensitivity-to-noise ratio, which is shown in Figure 3.19 (B). The Raman system was demonstrated to be capable of detecting a change of crystalline API of less than 1% w/w across the entire wavenumber range.

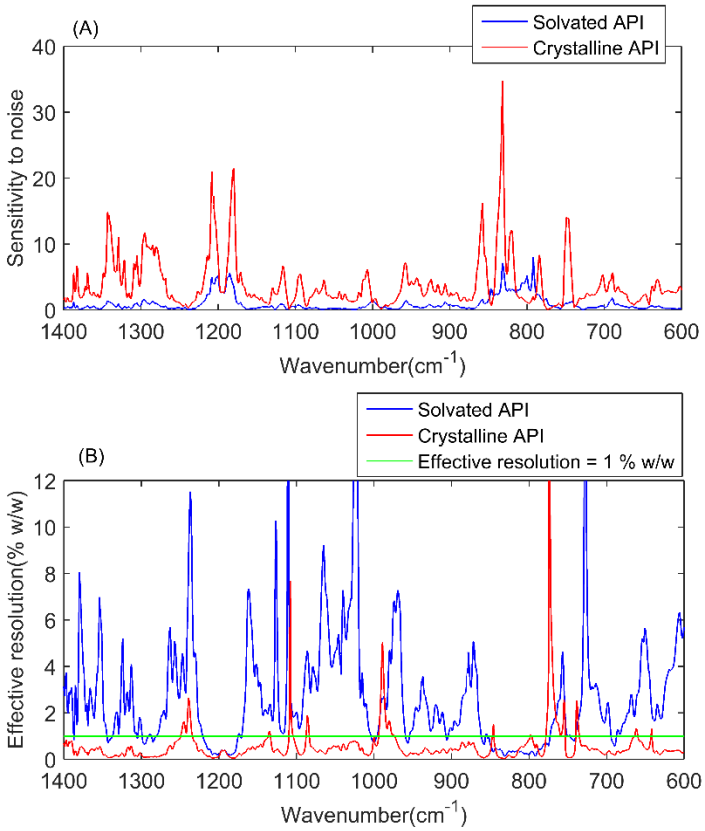

Figure 3.19 A: Signal to noise ratio of the Raman system for different phases of the API; B: Effective resolution for the Raman system.

3.3.4.3 XRD System

The sensitivity of the XRD system was estimated and compared with that of the Raman system and the NIR system. In Figure 3.20 (A), the XRD diffractogram of DIA patches was dominated by the strong signal from the polyethylene terephthalate (PET) liners around 20-30 °2θ.[186] The polymer is a semi-crystalline polymer with co-existing crystalline and amorphous phases. The signal from the crystalline ibuprofen was overwhelmed by the signal from the PET liner. The region of 0 to 20 °2θ was used to calculate the sensitivity of the XRD to API in DIA patches (see Figure 3.20 (B)). The diffractograms were corrected by removing a polynomial fit to

the baseline. The diffractograms after baseline removal are shown in Figure 3.20 (C). The diffraction peaks of ibuprofen crystalline powder were found in the diffractograms of DIA patches.

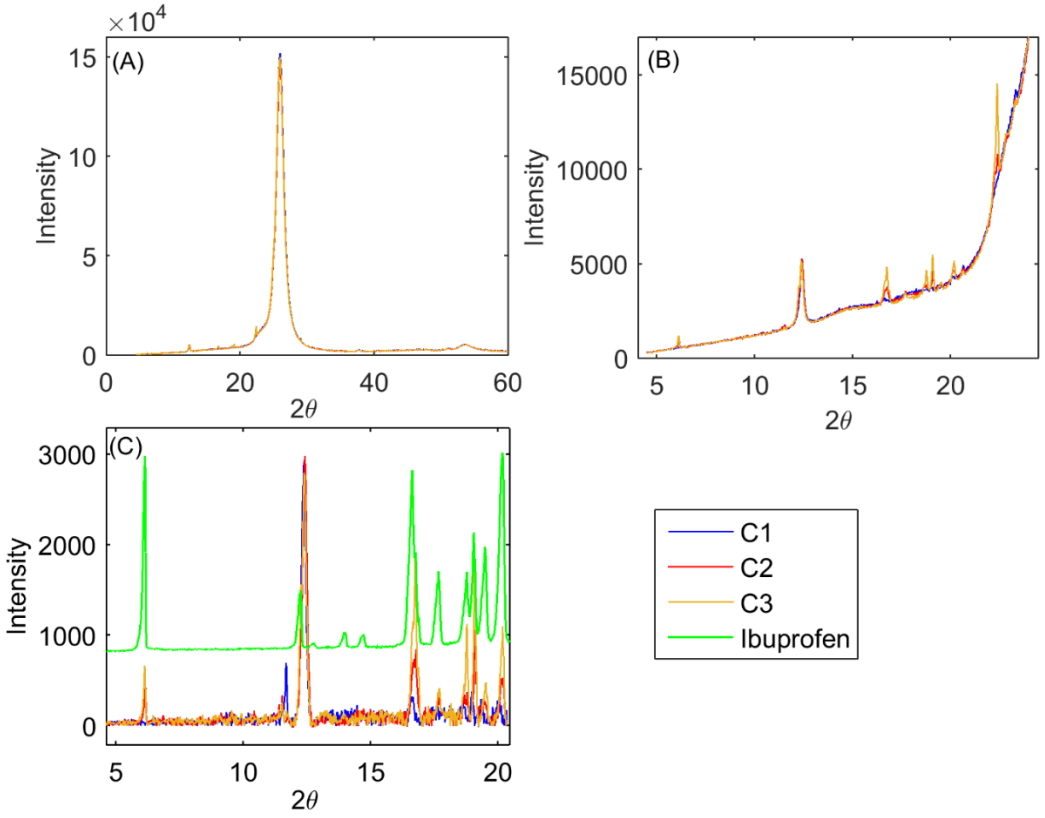

Figure 3.20 XRD patterns of patch C1, C2 and C3 over A: 0-60 °2θ; B: 0-20 °2θ; C: An overlay of ibuprofen XRD pattern and the diffractogram of samples C1-C3 after baseline removal.

The API dissolved in the polymer matrix do not possess the long-range order present in the crystalline structure. Thus, the solvated form did not show distinctive Bragg peaks. That is why XRD is much more sensitive to the crystalline solids than to the amorphous solids. The sensitivity of the XRD system to the crystalline API is illustrated in Figure 3.21 (A). The sensitivity values are on the magnitude of a few hundred in detector counts at the diffraction angles unique to the crystalline ibuprofen. The noise of the XRD system, however, is on the same magnitude. The noise profile of sample C2 is demonstrated in Figure 3.21(B). The large noise compared to the signal

adversely reduced the limit of detection of the XRD system, for detecting crystalline drug in DIA transdermal patches.

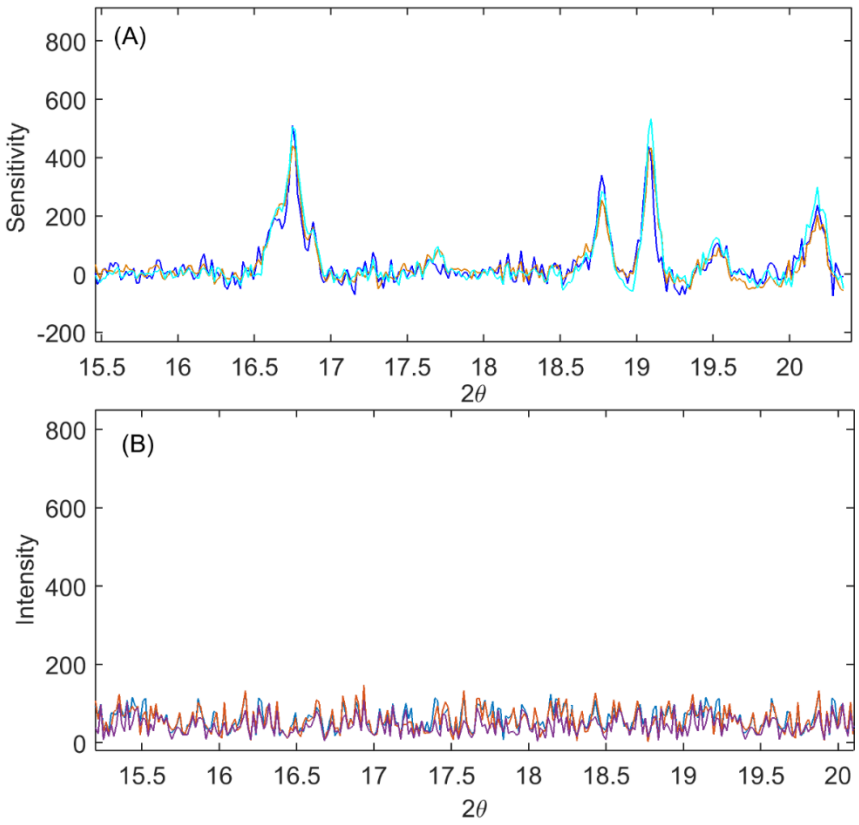

Figure 3.21 A: Sensitivity of the XRD system to the crystalline ibuprofen determined from difference spectra of samples C1, C2, and C3; B: The standard deviations of diffractograms collected from the sample C2 without repositioning.

The sensitivity to noise ratio is illustrated in Figure 3.22(A) for the crystalline API. The shaded regions marked in green color show the major diffraction peaks of crystalline ibuprofen. These regions are also associated with relatively high effective resolutions (<1% w/w). Compared to the NIR and Raman systems, the XRD system can only detect the crystalline API at an elevated concentration.

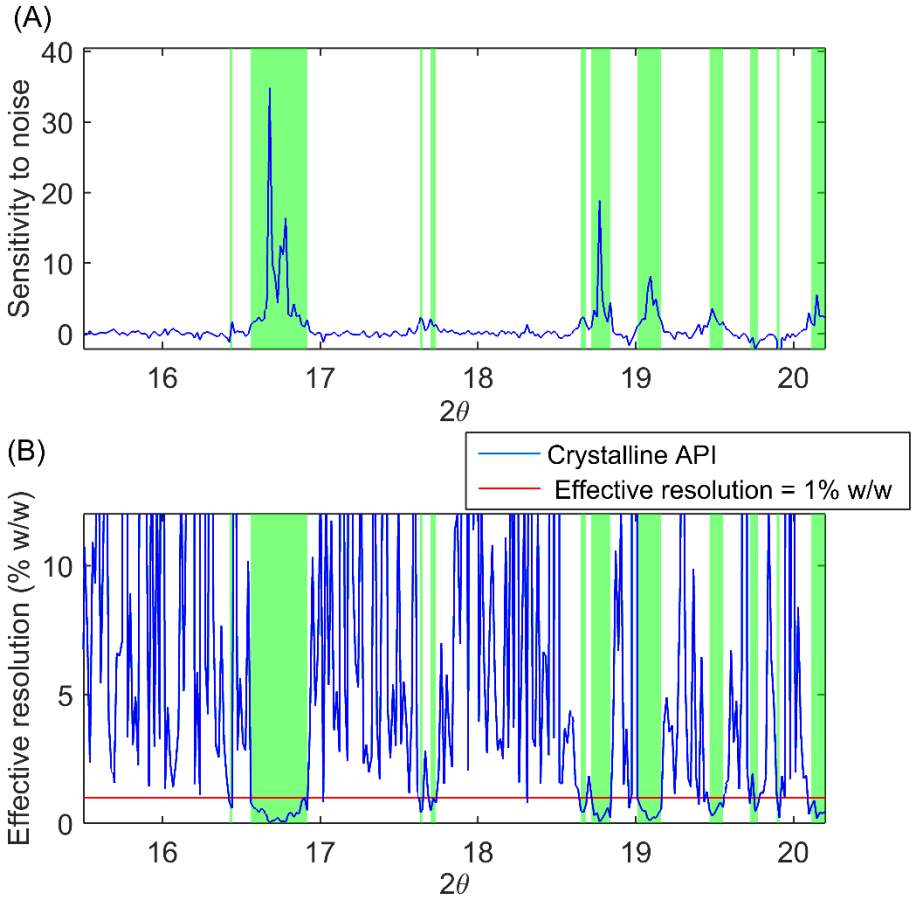

Figure 3.22 A: A plot of signal to noise ratio of XRD system determined from diffractograms of patches C1-C3; B: The effective resolution of the XRD system to the crystalline API.

Table 3.2 contains all the univariate sensitivities and effective resolutions for the two API forms measured by three analytical instruments. The univariate sensitivity was calculated as the sum of the sensitivities across the selected variables (wavelength, wavenumber and 2θ). The number of variables included in the calculation potentially affect the results. Therefore, the same number of variables (280) were used to calculate univariate sensitivity. Sensitivity across devices operating on different principles cannot be compared because different units are involved. Thus, the univariate sensitivity was used solely to compare the sensitivity of the two solid phases, via the same instrument. From the results discussed, both NIR and Raman instruments display stronger sensitivity to the crystalline phase relative to the solvated phase of the API. The XRD,

on the other hand, exhibited minimal sensitivity to the solvated phase. Alternatively, this means XRD exhibited superior selectivity to the crystalline API.

The effective resolution is a normalized statistic which quantifies sensitivity with respect to analytical precision.[191] The NIR has the smallest effective resolution for both the crystalline and the solvated API. The good sensitivity of NIR system is attributed to the high precision of this instrument. However, the NIR system is sensitive to physical variations. The baseline variations can easily alter the sensitivity calculation if they are not adjusted properly.

The Raman system has shown an average effective resolution of 0.69 % w/w. The sample homogeneity and repositioning error have direct influences on the noise vector obtained from repeated measurements via the Raman probe. The NIR instrument sampled the entire patch and the Raman system only sampled about 10% of the patch area due to the small spot size available. The impact of sampling heterogeneity was reduced by increasing the number of scans.

The XRD has the lowest effective resolution of 5.27% w/w. This is because the coated patches C1-C3 contain very small amounts of crystalline API that are lower than the detection limit of the XRD system. The mass of each coated patch was about 120 mg and the crystalline API was only about 1-8 mg. Moreover, the particles were all coated into one thin layer near the liner side of the patch. The sample surface may have not been at the best height for optimal signal collection. These factors may have contributed to the low XRD signal from the DIA system. From the effective resolution results, the two spectroscopic methods (NIR and Raman) have similar or better sensitivity as compared to the XRD method for detecting crystalline API in DIA patches.

3.3.5 Instrument Selectivity

Selectivity is a measure of the performance of an analytical system for detecting or quantifying the analyte of interest in the presence of interferences such as excipients, degradants, and polymorphs. The selectivity of the NIR instrument to different physical forms of the drug is low because the NIR peaks are broad and overlapping. Therefore, calibration and optimization are required to achieve good selectivity. The Raman system typically has very good selectivity to the different structures of molecules in the solid state. Therefore, it can be used to quantify crystalline API in amorphous matrices. Comparatively, the XRD system responds to crystalline materials exclusively so it is a technique of good specificity to the crystalline API.

a. PCA analysis

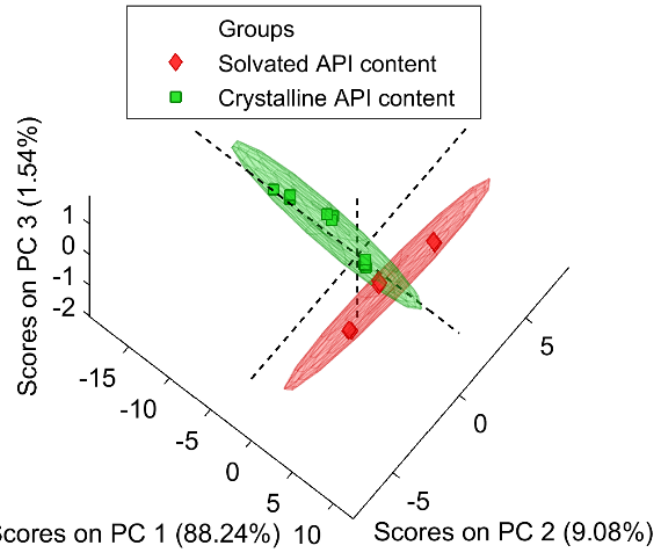

Figure 3.23PC scores of NIR spectra of samples containing crystalline API (C1-C3) and solvated API (A1-A3)

The confidence ellipses of the two groups representing the samples with and without spiked crystalline API are depicted in Figure 3.23 and Figure 3.24. The confidence ellipses included the 95% confidence interval of the covariance matrices of each sample group. The angle between the

planes containing the longer axes is 76.07 ° for NIR and 86.35 ° for Raman, suggesting the variance of the data of the two sample systems have limited correlations. The plot showed the potential of the NIR system to discriminate spectral variations arising from changes in the crystallinity versus that in the solvated API contents.

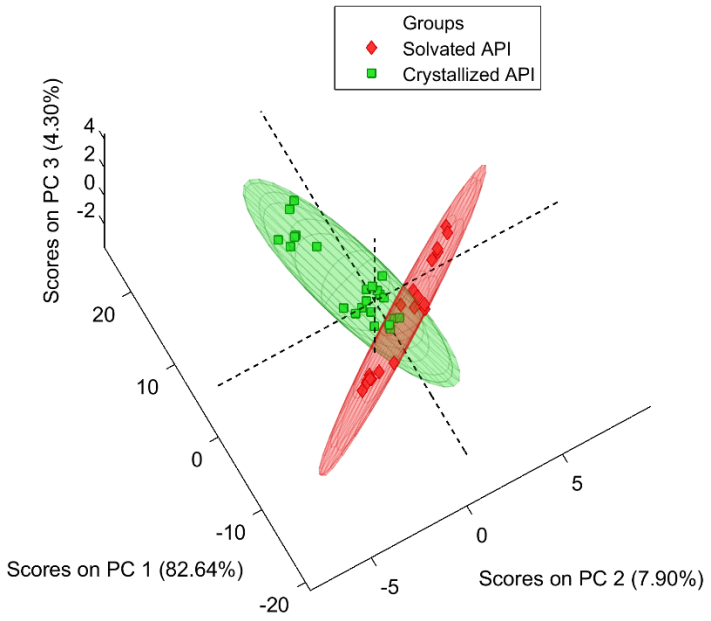

Figure 3.24 PC scores of Raman spectra of samples containing crystalline API (C1-C3) and solvated API (A1-A3)

Table 3.3 Angles between the longest planes of the 95% confidence ellipsoids fitted to PC scores of C1-C3 and A1-A3 spectra

Analytical Method	Shortest axes of confidence ellipsoids		Angle (°)
	C1-C3	A1-A3	
NIR	x+13.74y+6.37z=0	x-0.25y-1.25z=0	76.08
Raman	x+4.15y+4.99z=0	x-1.58y+0.56z=0	86.35

b. Prediction of the Crystalline API Content in Samples with Solvated API Content Variations

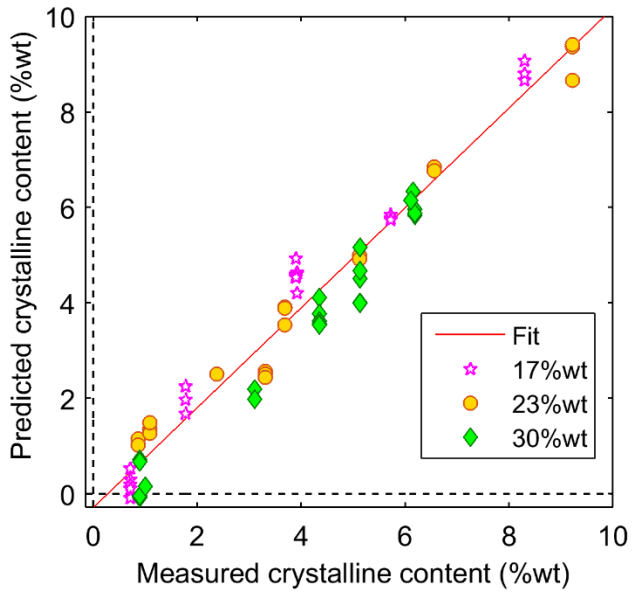

Figure 3.25The measured versus the predicted crystalline API contents of patches with varying solvated API concentrations using the NIR method.

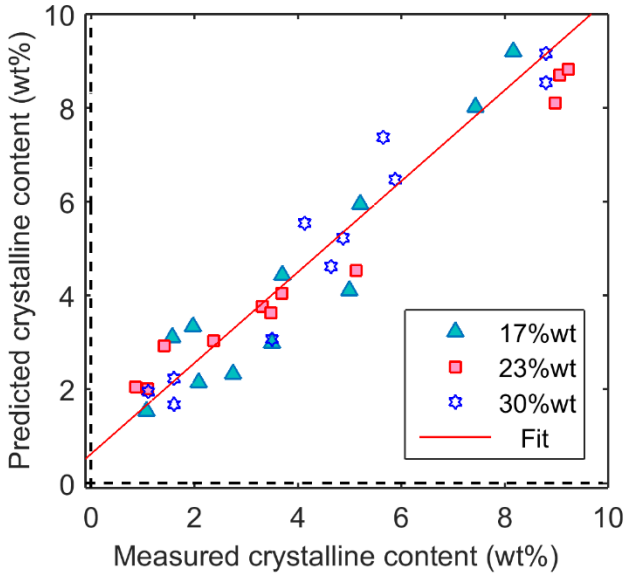

Figure 3.26 The measured versus the predicted crystalline API contents of patches with varying solvated API concentrations using the Raman method.

An analytical method is selective against a particular interference if the analytical results it renders is independent of the variations of the interference.[192] The National Committee for Clinical Laboratory Standards[193] and International Conference on Harmonization[194] both recommend accessing the degree of interference by measuring the error in the analytical results as

a function of the concentration of a given interference. The amorphous form of the drug is an interference to the crystalline drug in solid dispersions during spectroscopic analyses. In the current work, the solvated form has high spectral correlations with the crystalline form of drug. Therefore, the selectivity of the two analytical techniques to the crystalline drug relative to the solvated drug was assessed by the accuracy of the crystalline content predictions in the presence of varying solvated API concentrations. The crystalline contents (1.0 to 8.0 %w/w) of samples with different solvated API contents (17.0 to 30.0% w/w) were determined using a PLS model. This PLS model was developed from samples of which the solvated API contents were fixed at 23.5% w/w (samples C1-C3).

The measured versus the predicted crystalline contents of patches using the NIR model and the Raman model are displayed in Figure 3.25 and Figure 3.26. The prediction errors for the tested samples containing 17.0%, 23.0% and 31.0% w/w solvated API were 0.54 %, 0.55% and 0.63 % w/w using the NIR model, and 0.83%, 0.78% and 0.80% w/w based on the Raman model. The smaller RMSEPs of the NIR predictions reinforced the sensitivity results. The NIR instrument exhibited superior sensitivity to the crystalline phase of the API. One-way ANOVA suggested there was no statistical difference between the predicted crystalline contents across the three groups. The PLS models were selective to the crystalline drug with insignificant interference from the solvated API. A quantitative XRD method was not developed because the diffraction peaks of the drug in DIA patches had low intensity and a long scan time was required (>40 min) to achieve sufficient signal.

Table 3.4 Prediction errors in crystallinity of samples loaded with different solvated drug content

Solvated drug content (%, w/w)	RMSEP (%, w/w)	
	NIR	Raman
17	0.54	0.83
23.5	0.55	0.78
30	0.63	0.80
ANOVA	P = 0.40	P = 0.77

3.4 Conclusions

A novel way of preparing calibration patches with precisely spiked amounts of crystalline API was described. The patch system consists liners coated with crystalline API particles and backings cast with solvated API in adhesive polymer. The spiked patches were carefully evaluated as the physical properties of the calibration samples must meet several requirements. Specifically, the spiked crystalline drug was found to be physically stable over a period of 40 min, which is adequate for completing all required analytical characterizations. The Raman analyzer probes an area smaller than the area of a patch. To reduce the sampling error, the homogeneity of the crystalline particles sprayed on the transdermal patch must be ensured. The sprayed particles distributed uniformly across the patch surface. The standard deviations of the area representing the crystalline drug is below 10% as determined by an optical microscope.

The penetration depth of the Raman laser beam in DIA patches was determined. A PTFE film was stacked between DIA patches and the signature peaks of the PTFE decreased in an exponential manner. The Raman analyzer was able to detect the signal of PTFE through 8-9 layers of transdermal patches. The light penetration depth in the DIA patches was relatively high

compared to pharmaceutical powders because a continuous phase of drug and polymer exists in the DIA patches. Thus, the Raman system has shown adequate penetration in a single DIA patch.

Sensitivity and selectivity are important figures of merits. They are commonly used to evaluate and compare the performance of analytical methods. The effective resolution is a normalized, unitless measure of analytical sensitivity of analytical techniques. It allows direct comparisons between orthogonal analytical methods. The NIR and the Raman systems have shown lower minimum discernable concentrations for crystalline phases as compared to that for the XRD system. The good sensitivity of the NIR system attributes to its low instrumental noise. The two potential techniques have also shown superior selectivity to the crystalline API relative to the solvated API.

Chapter 4 : Development of Quantitative NIR and Raman Methods for Crystalline API Content Determination in Drug-in-adhesive Patches

4.1 Background and Introduction

The sensitivity of the investigated spectroscopic instruments for two API phases have been demonstrated in the previous chapter. Quantitative models for crystalline content determination via these tools are useful for quality evaluation of DIA patches. The information provided by the quantitative models can be used to study the crystallization mechnisms of an API in a polymer. In this chapter, calibration models are developed from spectroscopic analyses of patches spiked with crystalline drug, coupled with multivariate regression analyses. The weight percentages of the crystalline API in the DIA patches were used as reference values for the calibration. Two independent test sets of DIA patches were prepared to evaluate the performance of the calibration models. The first test set was composed of spiked samples with a constant total drug content. The purpose was simulate the process of solvated drug converting to crystalline drug. The crystalline drug and the solvated drug maintained a mass balance during crystallization. The drug load of samples of the second test set was the same as the first test set. However, the samples in this set were initially free of crystals. The crystallization of drug in the second test set was continuously monitored until the crystalline content reached a plateau. The correlation between the spectra of the two sets was calculated and spectral variations were compared.

Analytical method validation is frequently performed to determine the reliability and robustness of the analytical results. There are two general strategies for conducting method validation. The first strategy is to determine specific characteristics of the analytical method and to compare them with the acceptance limits. These characteristics typically include specificity, accuracy, precision, linearity, limit of detection, and robustness. The second strategy involves

using a single concept based on uncertainty to deliver fit-for-purpose evaluation.[195] This approach focuses on accuracy profile, a visual tool the method developers use to make statistical decisions. The main advantage of the second strategy is that an accuracy profile unifies several traditional validation figures of merits. In this chapter, the validation characteristics as well as accuracy profiles were determined to demonstrate the spectroscopic methods are suitable for crystallinity quantification in the chosen DIA system.

4.2 Experimental Methods

4.2.1 Design of Calibration Samples

The drug ibuprofen and adhesive Duro-Tak® 2052 were dissolved in ethyl acetate and cast onto backing layers as described in Section 2.2.2. Crystalline drug particles were coated onto liners following the procedure in Section 3.2.1.2. The backing layers and liners were combined to achieve the crystallinity according to a two-factor factorial design (Table 4.1). The two factors were the mass fraction of the drug dissolved in the adhesive and the mass fraction of drug sprayed onto liners. The crystalline content was varied from 0.0 to 4.8% w/w, or 0.0 to 22.0 % in terms of crystallinity (see Table 4.1). Besides a calibration set, two test sets were prepared. Test Set A was spiked by 0.0 to 4.8 % of crystalline API. The total API content of each patch was 23.5% w/w. The remaining 18.0-28.0 % w/w of the drug was added to the adhesive, maintaining a mass balance for the total drug content of these patches. This test set was used to evaluate the performance of the calibration model. Test Set B contained 23.5% w/w solvated ibuprofen. The samples of Test Set B were stored at 25 °C and 56 %RH. Drug crystallization was periodically measured by the NIR and the Raman systems.

Table 4.1 The compositions of calibration and test sets based on a full factorial design

	No.	Crystalline-Sprayed API (%, w/w)	Amorphous-Solvated API (%, w/w)	Adhesive Dry Weight (%, w/w)	Initial Crystallinity (%)
Calibration	C-1	0.0	17.0	83.0	0.0
	C-2	0.4	17.0	82.6	2.3
	C-3	1.2	17.0	81.8	6.6
	C-4	2.4	17.0	80.6	12.4
	C-5	4.8	17.0	78.2	22.0
	C-6	0.0	23.5	76.5	0.0
	C-7	0.4	23.5	76.1	1.7
	C-8	1.2	23.5	75.3	4.9
	C-9	2.4	23.5	74.1	9.3
	C-10	4.8	23.5	71.7	17.0
	C-11	0.0	30.0	70.0	0.0
	C-12	0.4	30.0	69.6	1.3
	C-13	1.2	30.0	68.8	3.8
	C-14	2.4	30.0	67.6	7.4
	C-15	4.8	30.0	65.2	13.8
Test A (spiked)	TA-1	0.0	23.5	76.5	0.0
	TA-2	0.4	23.1	76.5	1.7
	TA-3	1.2	22.3	76.5	5.1
	TA-4	2.4	21.1	76.5	10.2
	TA-5	4.8	18.7	76.5	20.4
Test B (recrystallized)	TB-1	0.0	23.5	76.5	0.0
Validation (spiked)	1	0.8	23.5	75.7	3.3
	2	1.2	23.5	75.3	4.9
	3	2.0	23.5	74.5	7.8
	4	3.0	23.5	73.5	11.3
	5	4.0	23.5	72.5	14.5

Comparisons between Test Set A and Test Set B allows the spectral features between the recrystallized and the spiked samples to be compared. The calibration model built from spiked samples can only be used to predict crystallinity in DIA patches when strong spectral similarities are demonstrated between the spiked and the authentically recrystallized samples. The third independent prediction set was a validation set. It was used for calculating the validation characteristics (specificity, accuracy, linearity, precision, and multivariate limit of detection) and accuracy profile. All four datasets are summarized in Figure 4.1. Six replicates were prepared at each design point. After spectroscopic measurements, the adhesive mixture was dissolved, and the drug content in each sample was analyzed by a UV spectrometer (Section 2.2.3.3).

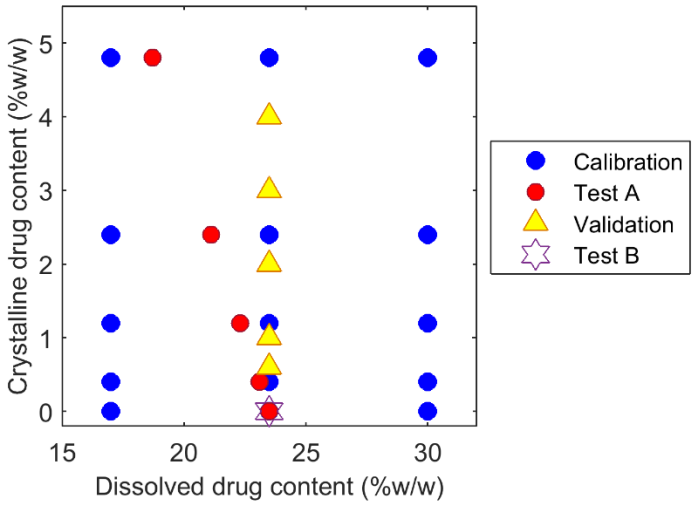

Figure 4.1 A plot of solvated and crystalline drug contents in the calibration set, test sets and validation set.

4.2.2 Spectroscopic Measurements

The DIA patches were measured by the NIR and the Raman systems within the time frame 0-t_{ind}. The areas of the spiked crystals remain statistically unchanged. The measurement was carried out following the procedure described in Section 2.2.4.1. Each sample was repeatedly measured for three times with and without repositioning. Five Raman spectra were collected on

each patch: four collected on the corners and one taken in the center. Multiple Raman spectra were taken to improve the sampling representativeness because the scale of scrutiny of the Raman probe was smaller than the size of one patch (1.5 by 1.5 cm). The obtained spectra were averaged to one spectrum per sample for calibration development and model testing. Due to a heterogeneous distribution of crystals in the Test Set B, 16 spectra were measured per sample.

The spectra of the pure components (blank adhesive films, supercooled liquid and crystalline API compacts) were collected on the NIR and Raman spectrometers. A sample of 300 mg crystalline ibuprofen was compressed at 4000 lb. into a 13 mm tablet using a Carver press (3887NE.LAutoPellt, Carver.Inc, Wabash, IN, USA). Approximately 1000 mg of ibuprofen powder was melted in a 10 mL beaker at 76 °C and cooled to 25 °C, yielding supercooled liquid ibuprofen. Blank adhesive films were prepared by dissolving Duro-Tak® 2052 in ethyl acetate and dried in oven at 55 °C for 24 hr.

4.2.3 Multivariate Data Analysis

4.2.3.1 Development of PLS Models

Spectral preprocessing and multivariate regression were performed using MATLAB R2015 a. (MathWorks Inc., Natick, MA, USA) using the PLS toolbox 7.9 (Eigenvector Research Inc., Manson, WA, USA). PLS calibration models were developed from the spectra of the calibration samples and the spiked crystalline drug contents expressed in percent crystallinity:

$$\%\ Crystallinity = \frac{m_{coated}}{m_{total}} \times 100\% \qquad (4.1)$$

where $m_{sprayed}$ is the mass of the drug particles coated on the liners and m_{total} is the mass of the drug determined by the UV method. Spectral preprocessing and variable selection methods are

summarized in Table 4.2. They were chosen by minimization of the root mean squared error of the calibration (RMSEC) and cross-validation (RMSECV):

$$\mathrm{RMSEC/V} = \sqrt{\frac{\sum(\hat{y}_i - y_i)^2}{n-N}} \tag{4.2}$$

The root mean squared error of the prediction (RMSEP) is calculated as:

$$\mathrm{RMSEP} = \sqrt{\frac{\sum(\hat{y}_i - y_i)^2}{n}} \tag{4.3}$$

where $\hat{y}_i$ and y_i are the predicted and the measured crystallinity for the i^{th} sample, n is the number of samples for the dataset under consideration, and N is the number of factors used in the model construction. Random subsets cross-validation with 6 splits and 20 iterations was used to determine the number of latent variables to include in the model. At the optimum number of latent variables, RMSEC and RMSECV began to diverge as the latent variable progressively increased.

Table 4.2 Preprocessing methods and spectral ranges used to build PLS models for crystalline content determination in DIA patches

	NIR data	Raman data
Spectral range	1291-1880 and 2022-2204 nm	767-1225 cm^{-1}
Preprocessing	SNV mean centering	Weighted least squares baseline removal + normalization to unit area + mean centering
Number of LV[d]	3	4

[d] LV: Latent variable

4.2.4 Model Comparisons

The performance of the PLS models based on NIR spectra and Raman spectra were compared to determine which instrument is better at predicting crystalline content in DIA system. Multivariate limit of detection was calculated for the independent test set and was compared sample-wise between the two methods. The prediction ability of the two models were compared with respect to accuracy (bias) and precision (standard error of prediction).

4.2.4.1 Multivariate Limit of Detection

Multivariate detection limit (MDL) is an important figure of merit for characterizing instrument performance. The MDL is calculated based on the prediction uncertainty associated with all steps of calibration and predictions, and it takes into account the probabilities of committing type I (false positive) and type II (false negative) errors:[196]

$$MDL = t_{1-\alpha,df} \cdot \sigma_{\hat{C}_D} + t_{1-\beta,df} \cdot \sigma_{\hat{y}_{pred,i}} \tag{4.5}$$

where $t_{1-\alpha,df}$ and $t_{1-\beta,df}$ are the single-tailed t-distribution values with probabilities of α and β for committing type I and type II errors, respectively. The variable $\sigma_{\hat{C}_D}$ is the standard deviation of the estimated detection response $\hat{r}_D$ of an unknown sample of zero crystallinity. The prediction uncertainty was determined using an errors-in-variables approach:[197]

$$\hat{\sigma}^2_{\hat{y}_{pred,i}} \approx \left(h_{p,i} + \frac{1}{I_{cal}}\right)\left(\hat{\sigma}_{\varepsilon c}{}^2 + \hat{\sigma}_{Yc,ref}{}^2 + \left\|\hat{\boldsymbol{b}}\right\|^2 \hat{\sigma}_{Xc}{}^2\right) + \hat{\sigma}_{\varepsilon p,i}{}^2 + \left\|\hat{\boldsymbol{b}}\right\|^2 \hat{\sigma}_{Xp,i}{}^2 \tag{4.6}$$

where $h_{p,i}$ is the leverage of the ith sample in test set, I_{cal} is the calibration sample size, $\hat{\boldsymbol{b}}$ is the estimated regression vector of the multivariate model, and $\hat{\sigma}_{Yc,ref}$ is the reference uncertainty. For calibration samples, the pooled standard deviations of the measurement error and that of the prediction residual are denoted by $\hat{\sigma}_{Xc}$ and $\hat{\sigma}_{\varepsilon c}$, respectively. $\hat{\sigma}_{Xp,i}$ and $\hat{\sigma}_{\varepsilon p,i}$ symbolize the standard

deviations of spectral measurement error and the prediction residual for the i[th] sample in the test set. The pooled standard deviations of the measurement errors were determined from repeated measurements of the samples.

4.2.4.2 Standard Error of Prediction and Bias

The performances of the multivariate models were evaluated through comparisons of standard error of predictions (SEP) and biases between models.[198] A t-confidence interval for paired samples was used to compare the biases. The difference between the means of the predicted, $m_1 - m_2$, has a standard deviation (SD):

$$S_d = \sqrt{\frac{\sum_{i=1}^{n}(d_i - \bar{d})^2}{n \times (n-1)}} \tag{4.7}$$

where $d_i = e_{i1} - e_{i2}$ is the difference between the two errors for the ith sample, and $\bar{d} = \frac{\sum_{i=1}^{n} d_i}{n}$. The 95% confidence interval for the true difference in biases is:

$$(m_1 - m_2) \pm t_{n-1,0.025} \times S_d \tag{4.8}$$

The lower and upper limits of a 95% confidence interval for the ratio of the true standard deviations are:

$$\frac{S_1}{S_2} \times \frac{1}{L} \text{ and } \frac{S_2}{S_1} \times \frac{1}{L} \tag{4.9}$$

where S_1 and S_2 denote the SEPs of the test set calculated from different multivariate models. Since the comparison was based on a common test set, the predictions generated from different techniques are often self-correlated. L is used to account for correlation between the two sets of prediction errors:

$$L = \sqrt{K + \sqrt{K^2 - 10}} \quad (4.10)$$

$$K = 1 + \frac{2(1-r^2)t^2_{n-2,0.025}}{n-2} \quad (4.11)$$

where *r* is the correlation coefficient between the two sets of prediction errors and $t^2_{n-2,0.025}$ is the upper 2.5% point of a t-distribution on *n*-2 degree of freedom. The two multivariate models were considered different when biases or the SEPs were significantly different. Two models were not significantly different only when the confidence interval for the true difference in biases included 0 and the ratio of SEPs included 1.

4.2.5 Comparison of Spiked and Recrystallized Patches

The spectra of spiked samples (Test set A) and naturally recrystallized samples (Test set B) were paired up and compared based on the predicted crystalline contents. For example, a spectrum of a spiked sample with 2.0% predicted crystallinity was obtained. At the same time, a spectrum of a recrystallized sample with 2.0% predicted crystallinity was also obtained. The correlation coefficient between the two spectra was calculated and the significance was tested by a t-test (P=0.05). The variance of the spectral signal was compared by using PC scores and the multivariate diagnostics including Hotelling's T^2 and Q residual.

4.2.6 Validation

The objective of validation is to ensure that every future measurement in routine analysis will be close enough to the unknown true value.[199] The study combines a number of validation approaches such as accuracy profile[195] and ICH validation strategies. The approach used in this study consisted of checking the conformity of performance measures to acceptability limits.

Method validation, together with uncertainty assessment, provide a way to independently and reliably assess the quality of analytical results.

4.2.6.1 Specificity

According to USP <1119>, evaluations of the specificity of a NIR method to the analyte of interest is based on both spectral attributes and chemometric parameters.[197] This approach is optional for other spectroscopic techniques such as Raman spectroscopy. All pure components were measured by the chosen analytical systems. The correlation coefficients between the loadings of the calibration model and the spectra of the pure components were used to evaluate the method specificity.

4.2.6.2 Precision

Precision describes the closeness of multiple measurements of the same homogeneous sample under a prescribed condition. Repeated measurements of the validation samples at Q3.3%, 7.8% 11.3% and 14.5% crystallinity were performed. Repeatability with no repositioning was determined as the relative standard deviations of six readings, without changing the location of each sample relative to the detector. Repeatability with repositioning was performed on patches that underwent removal and replacement on the sampling stage between consecutive scans. Intermediate precision was conducted on validation samples prepared on three different days.

4.2.6.3 Accuracy Profile

Accuracy profile is a decision-making graphical tool designed to help analysts decide whether or not an analytical procedure is valid.[195] The difference between the measured value (X) and the unknown true value (μ) should be lower than an acceptance limit (λ):

$$|X - \mu| < \lambda \tag{4.12}$$

The probability that a measurement will fall outside the acceptance limits is less or equal to the maximum risk (5%) that the analyst is able to take during routine use:

$$Pr(|X - \mu T| < \lambda) \geq \beta \tag{4.13}$$

The β-expectantion tolerance interval is calculated based on the following formula to check if it fits into the acceptability limits:[200-201]

$$\hat{\delta}_M \pm Q_t k_s \hat{\sigma}_M \tag{4.14}$$

where

$$\hat{\sigma}_M^2 = \hat{\sigma}_B^2 + \hat{\sigma}_W^2 \tag{4.15}$$

$\hat{\sigma}_M^2$, $\hat{\sigma}_B^2$ and $\hat{\sigma}_W^2$ are the estimates of the intermediate precision variance, the between-day variance and the within-day variance. $\hat{\delta}_M$ is the estimated bias. Q_t is the β quantile of the Student's t-distribution with υ degree of freedom:

$$\upsilon = \frac{(R+1)^2}{\left(R+\left(\frac{1}{n}\right)\right)^2/(p-1)+(1-\left(\frac{1}{n}\right))/pn} \tag{4.16}$$

$$R = \frac{\hat{\sigma}_B^2}{\hat{\sigma}_W^2} \tag{4.17}$$

where p is the number of experimental conditions used in precision tests and n is the number of independent replicate in each series. k_s is an expasion factor that takes into account the variability of the mean bias. It was estimated as follows:

$$k_s = \sqrt{1 + \frac{1}{pnB^2}} \tag{4.17}$$

with

$$B = \sqrt{\frac{R+1}{nR+1}} \tag{4.18}$$

4.3 Results and Discussion

4.3.1 Calibration Model Development

The increase in opacity of patches (Batch C6 to C10) because of increasing crystalline content is illustrated in Figure 4.2. The crystallinity from left to right are 0, 1.7, 4.9, 9.3 and 17.0%, corresponding to mass fraction of 0, 0.4, 1.2, 2.4 and 4.8% w/w of film weight. The coated particles were uniformly distributed across the patch surface.

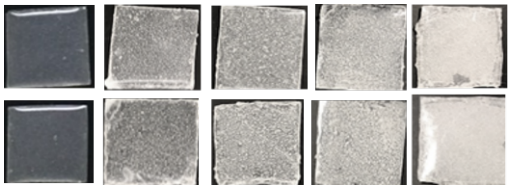

Figure 4.2 Calibration samples spiked by crystalline ibuprofen particles. The crystallinity from left to right are 0, 1.7, 4.9, 9.3 and 17.0%, corresponding to mass fraction of 0, 0.4, 1.2, 2.4 and 4.8% w/w.

4.3.1.1 NIR PLS Model

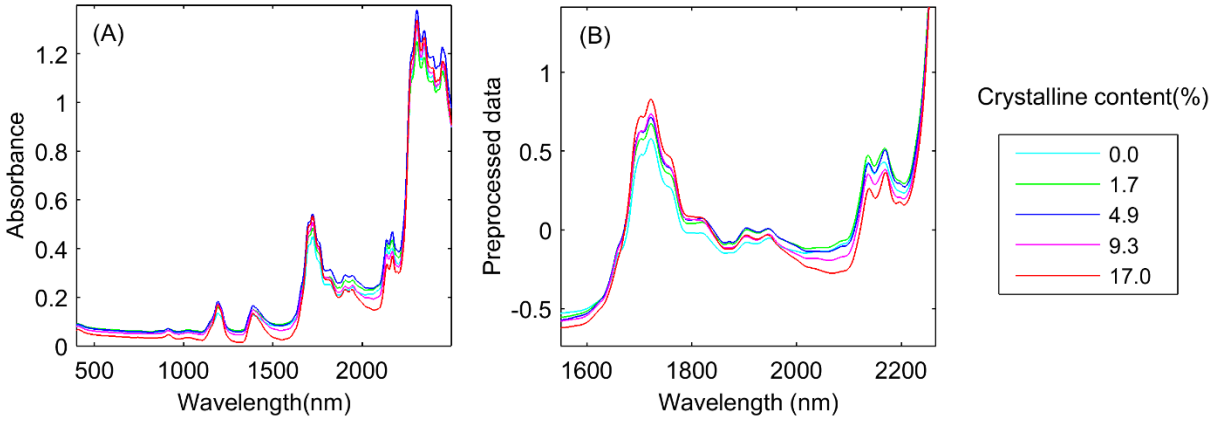

Figure 4.3 A: NIR spectra of the calibration set with varying crystalline content; B: SNV preprocessed NIR spectra of the calibration set in the region of 1560-2250 nm.

The dependence of NIR signal intensity on crystalline drug is illustrated in the Figure 4.3. Each spectrum represents the mean of six spectra at each crystalline level (Batch C6-C10). There is a baseline change accompanying the change in the crystalline content. The baseline first

increased as the crystallinity increased from 0% to 4.9% and then decreased as the crystallinity continued to increase. SNV was applied to the NIR spectra to reduce the influence of baseline and scale differences. The SNV-corrected spectra are drawn in Figure 4.3 (B). Although there is a decreased baseline near 2000 nm, there is a pronounced increase in the peak intensity at 2171 nm with the increase of the crystalline content. Spectral differences between pure crystalline and supercooled liquid phases was observed in this region.

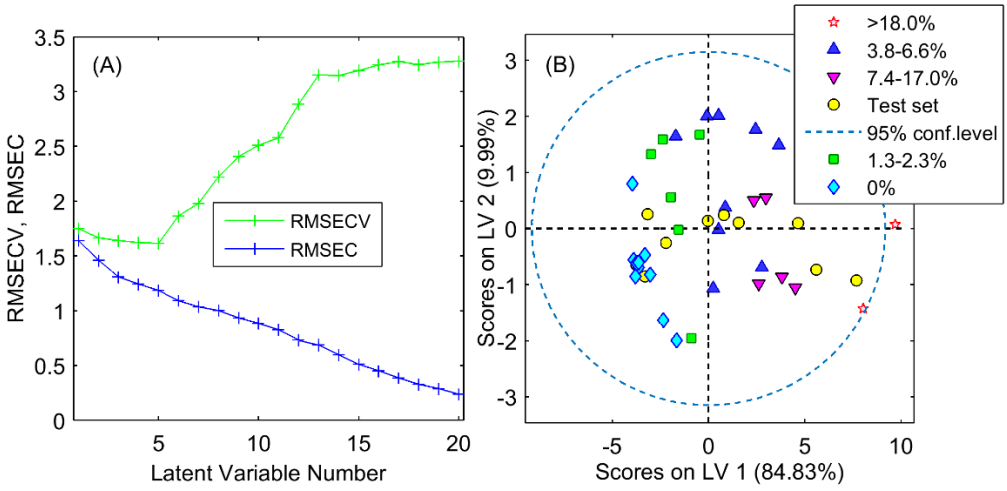

Figure 4.4 A: RMSEC and RMSECV as a function of number of latent variables used in the NIR PLS model development. B: PC scores of the calibration set and the test set A.

A PLS model was developed from the NIR spectra of the calibration set. The wavelength regions of 1291-1880 and 2022-2204 nm were selected. The wavelength regions of 1400-1500 nm and1880-2022 nm were excluded because they were affected by moisture. The spectral preprocessing, including SNV and mean-centering, were performed after wavelength selection. Three latent variables were chosen based on the divergence of RMSEC and RMSECV as a function of latent variable, as is shown in Figure 4.4(A). One may argue that five latent variables should be selected. However, the first three latent variables explained more than 95% variance in both X and Y. Adding additional latent variables may run the risk of overfitting the model. The variance in X (NIR signal) accounted by the three LVs were 85.83%, 9.99% and 2.11% whereas the variance in

Y (crystallinity) explained by the three LVs were 94.48%, 1.14% and 0.87%. The PC scores of calibration data on LV1 and LV2 were plotted in Figure 4.4(B). The scores on LV1 gradually increased as the crystalline content increased. The variance spanned by the test set is contained in that of the calibration set, as is shown in Figure 4.4(B).

4.3.1.2 Raman PLS Model

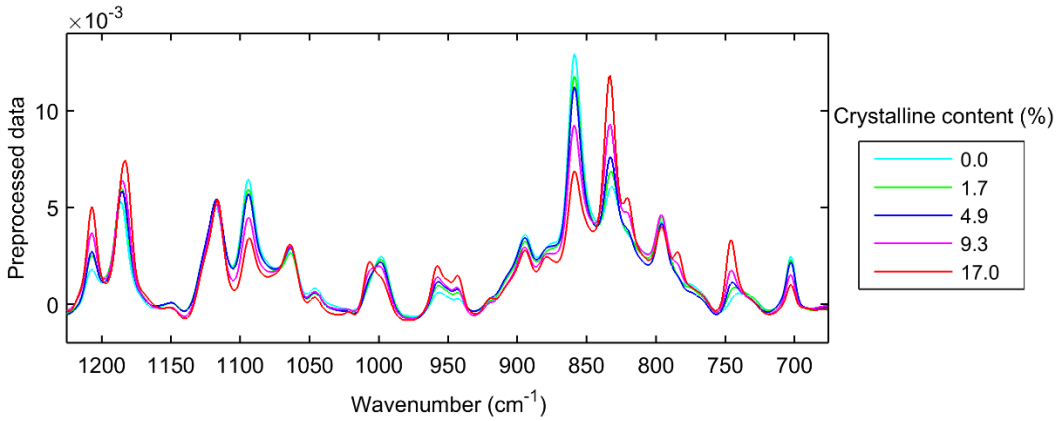

Figure 4.5 The preprocessed Raman spectra of calibration set with varying crystalline content (preprocessing methods include weighted-least-squares baseline removal and normalization to unit area).

Each spectrum in Figure 4.5 is the mean of spectra of samples at each crystalline level. Several spectral changes were observed as the crystalline content was increased. Peak intensity increased at 1207, 958, 833 and 746 cm^{-1}. Two shoulder peaks emerged at 820 and 784 cm^{-1}. Wavenumber of the peak at 1185 and 998 cm^{-1} changed with the increase in crystallinity, which is consistent with the peak changes found between the supercooled liquid and the crystalline drug.

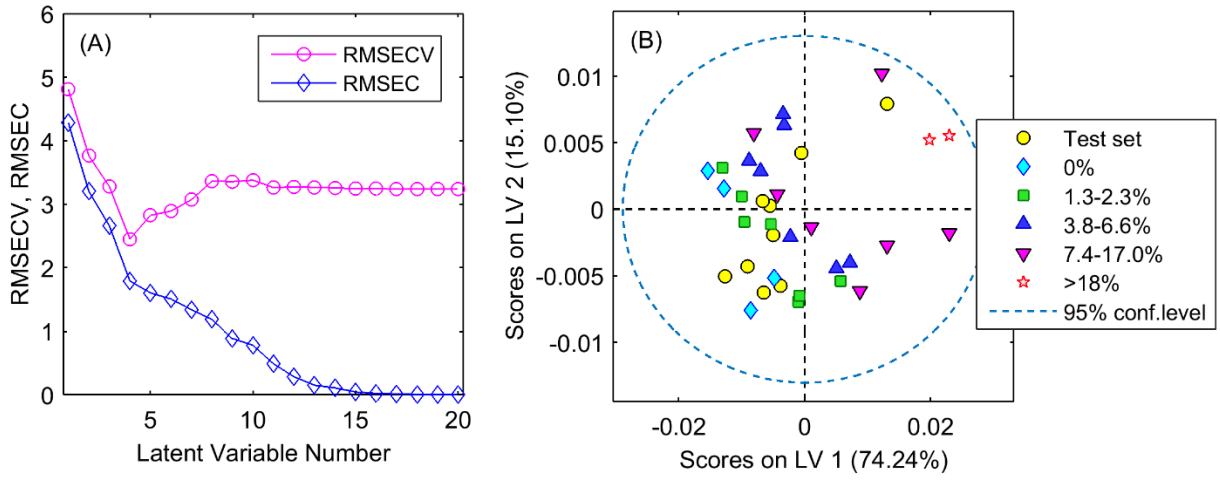

Figure 4.6 A: RMSEC and RMSECV as a function of number of latent variables used in the Raman PLS model development. B: PC scores of the calibration set and the test set.

The wavelength regions of 767-1225 cm^{-1} were selected to develop a PLS model. This region is inside the fingerprint region of organic molecules thus providing plentiful of information about the structure and arrangements of the drug molecules. The spectral preprocessing methods include weighted-least-squares baseline removal, normalization to unit area and mean-centering. The number of latent variables (4 LVs) were chosen based on the divergence of RMSEC and RMSECV as a function of latent variable number, as is shown in Figure 4.6 (A). The variance in X (Raman signal) accounted by the first four LVs were 74.24%, 15.10%, 6.57% and 2.21% whereas the variance in Y(crystallinity) explained were 61.20%, 17.11%, 6.74 and 8.16%. The scores of calibration data on LV1 and LV2 were plotted in Figure 4.6(B). The variance spanned by the test set is contained in that of the calibration set.

4.3.1.3 Model Performance Evaluation

The PLS models were calculated and optimized using the NIR and the Raman spectra. The model statistical parameters are displayed in Figure 4.7. From the calibration and prediction errors, the NIR model outperformed the Raman model. The calibration and prediction errors of the NIR

method are approximately 50% lower than that of the Raman method. The agrees with the results of the sensitivity study in 3.3.4 in which NIR instrument showed better sensitivity to the crystalline API relative to the Raman instrument.

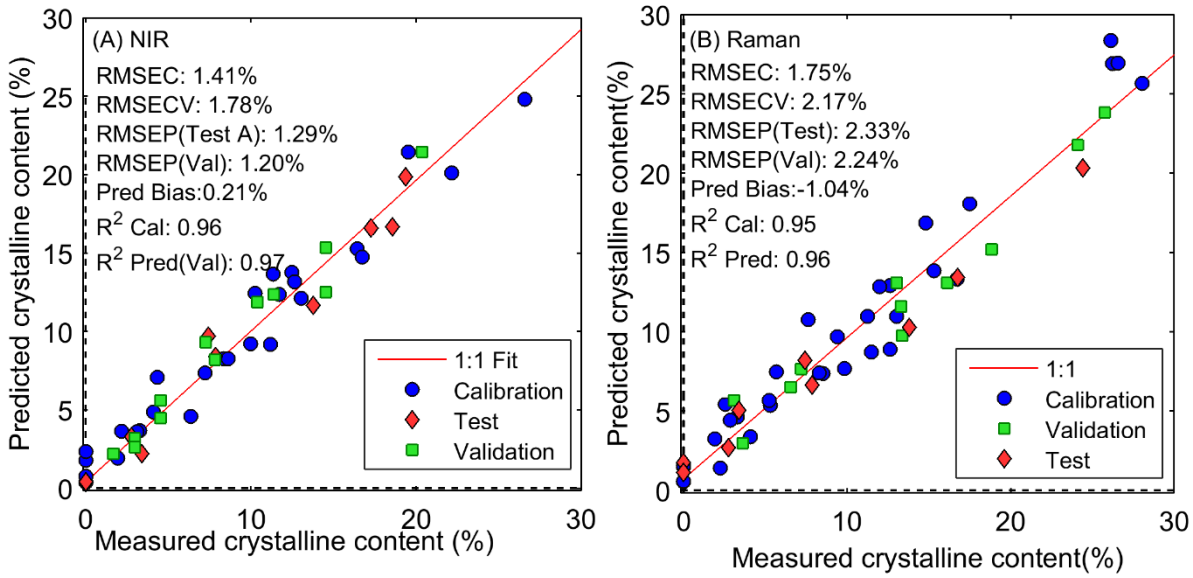

Figure 4.7 The predicted and measured crystalline contents of the calibration, test and validation sets. A: NIR data; B: Raman data.

The predictive ability of the two models were compared in terms of SEP and bias. The confidence interval of the bias was estimated to be (-1.422, 1.724), suggesting the bias was not significant between the two models. However, the confidence interval of the SEP, (0.318, 0.690), did not include 1. The SEPs of the prediction results for the NIR is smaller than that of the Raman. This result confirms that the NIR analyzer exhibits superior precision.

4.3.2 Test Sets - Comparing Spiked and Recrystallized Patches

The similarity between the spiked and the recrystallized patches was evaluated using the Raman method. The set A was prepared by spiking crystalline API and solvated drug to achieve a total drug content of 23.5% w/w. This is to simulate the natural drug crystallization process which follows the direction pointed out by the black arrow drawn in Figure 4.8. Test set B consisted 23.5%

w/w API in the solvated form. As the patches were stored in stressed environment to induce crystallization, the crystalline content started to increase and eventually reaching similar composition as the spiked samples. Five pairs of samples with similar predicted crystallinity were grouped together for comparisons.

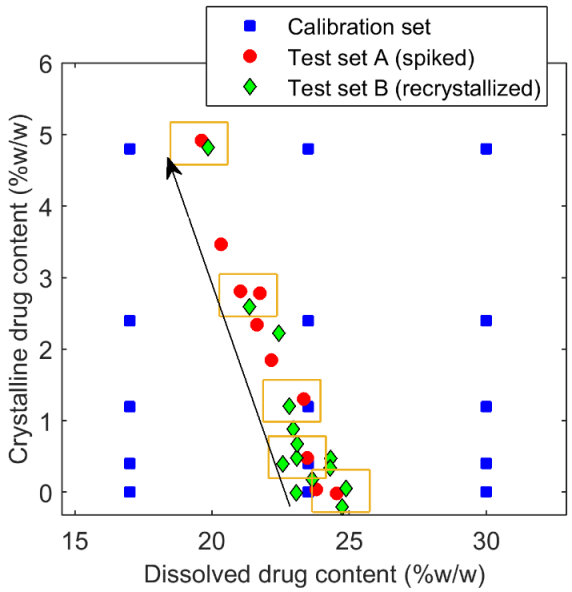

Figure 4.8 The crystalline drug contents and solvated drug contents of spiked and recrystallized DIA patches. Samples marked in orange rectangles are the five pairs of samples compared in 4.3.2.

A high degree of spectral correlation was found between the two test sets as the crystallinity was varied between 0.3 and 5.0% w/w, as is shown in Figure 4.9. The preprocessing method, normalization to unit area, helped to remove the scale variation. The increase in the crystallinity can be well tracked in Raman spectra in both the spiked and the recrystallized samples. There were increases of peaks at 708, 1144 and 1058 cm^{-1}. Two shoulder peaks emerged at 1107 and 1170 cm^{-1} as the crystallinity reached 10, or 2.5% w/w. The spectral similarity was represented by the high correlation coefficient (>0.98) between each pairs of spectra.

The PC1 and PC2 scores of the two test sets were plotted in Figure 4.10 (A). The first two PCs (90% variance in X) represent where the variance of the samples reside with respect to the

calibration data. Both the spiked and recrystallized patches were found within the space enclosed by the calibration samples. The Hotelling's T^2 and Q residuals of the two sets can be found in Figure 4.10 (B). The recrystallized samples yielded larger Q residuals than that of the spiked samples, indicating presence of unmodeled variance. Figure 4.9 shows the correlation between the spectra of the spiked and the recrystallized samples decreased progressively as the crystalline content increased. The crystals tend to recrystallize at the interface between the liner and the adhesive layer. The interface can serve as heterogeneous nucleation sites. With this knowledge, the test set B was spiked with drug crystals on the same interface.

A possible explanation for the inflated Q-residuals of the naturally recrystallized samples is the shape and sizes of crystals in this system is different from the spiked samples. Another possible explanation is the water contents of the samples were different. The intensity of fluorescence measured by the Raman spectrometer can be quenched by water.[202] Factors altering the baseline or fluorescence level of the Raman spectra may have inflated the Q-residuals of the recrystallized samples.

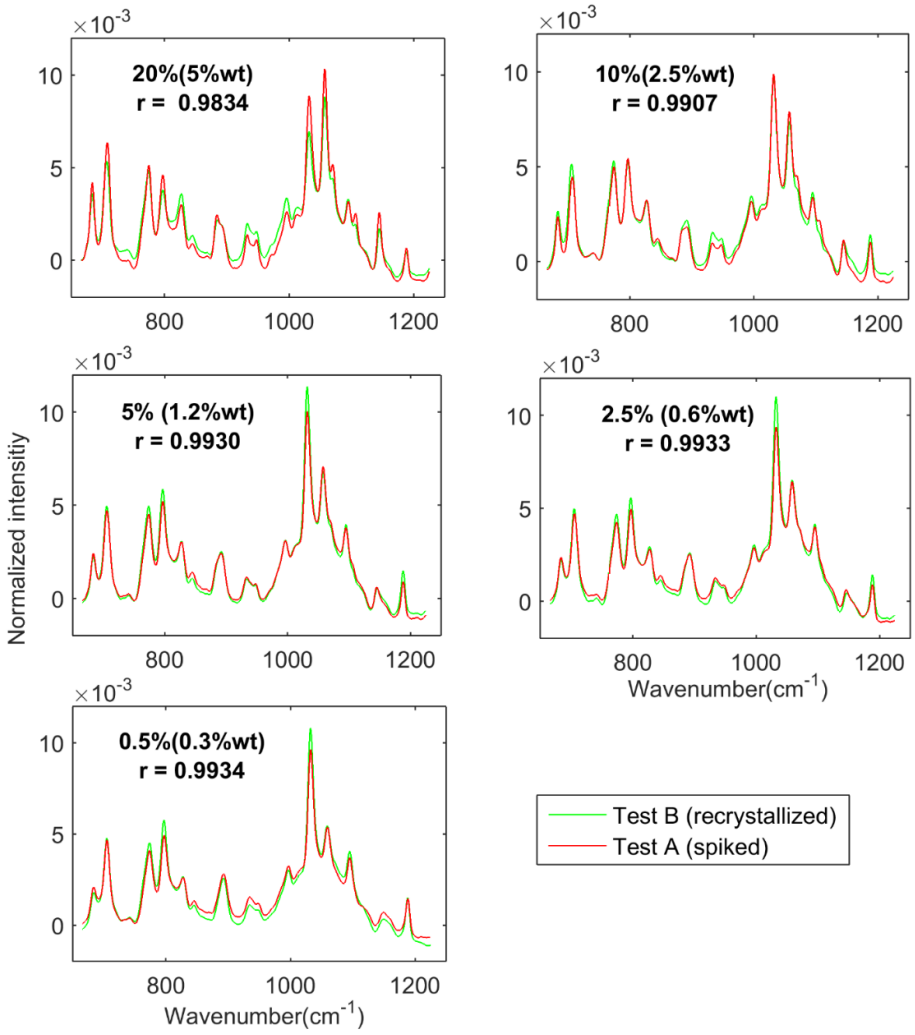

Figure 4.9 Raman spectra of spiked and recrystallized patches with similar crystallinity (0.5 to 20% in crystallinity or 0.3 to 5% w/w). The correlation coefficient (r) for each pair of spectra can be found in each plot.

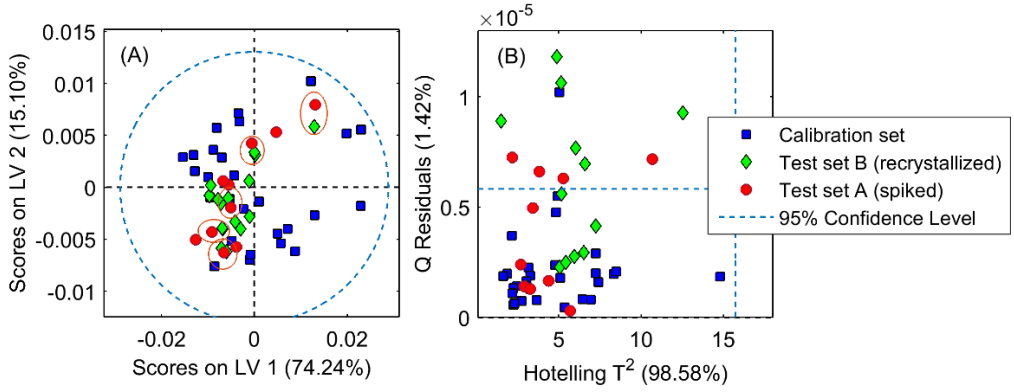

Figure 4.10 A: A schematic demonstrating similar PC scores of the five groups of recrystallized and spiked samples. Samples marked in red circles are the five pairs of samples compared in terms of spectral similarities in 4.3.2.B: Hotelling's T^2 and Q residuals of the calibration set and two test sets.

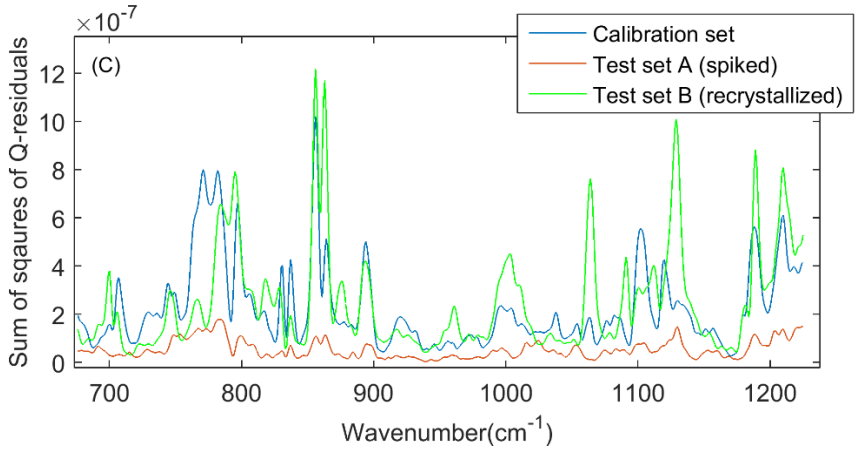

Figure 4.11 Q-residual contribution plots for the calibration set and two test sets.

4.3.3 Validation Results

4.3.3.1 Specificity

The spectral similarity and differences of NIR and Raman spectra of pure components are displayed in Figure 4.11 (A) and Figure 4.12 (A). The plots were scaled (normalization to unit area) to facilitate visual comparisons. The correlation between components are calculated for the full wavelength or wavenumber region as well as for the region used in the calibration models. The NIR spectrum of drug in the crystalline form resembles that of the supercooled liquid form. The NIR spectra of these two physical forms had high correlation (0.96). In comparison, crystalline and supercooled liquid ibuprofen show many differences in Raman spectra. A correlation coefficient of 0.81 was observed between their spectra. The crystalline ibuprofen has peaks at 663, 784, 820 cm^{-1} that are absent in the Raman spectrum of the supercooled liquid. The crystalline ibuprofen also has larger peaks compared to the supercooled liquid.

In Table 4.3, The correlation between the API and the adhesive is higher for the NIR spectra than that for the Raman spectra. This finding supports literature reports that Raman spectroscopy is sensitive to conjugated double bonds, aromatic rings and other structures present in most APIs,

but is not sensitive to polymeric excipients,[203-204] which may be related to the high chemical specificity of this technique.

Table 4.3 Correlation coefficients between the components used in the DIA patch formulation

Correlation coefficient	NIR		Raman	
	1100-2500 nm	860-1108 2020-2209 nm	150-1850 cm^{-1}	767-1225 cm^{-1}
API(crystal) vs. API(supercooled liquid)	0.96	0.99	0.81	0.79
API(crystal) vs. Adhesive + liner + backing	0.89	0.87	0.09	-0.14
API(supercooled liquid) vs. Adhesive + liner + backing	0.85	0.87	0.08	-0.13

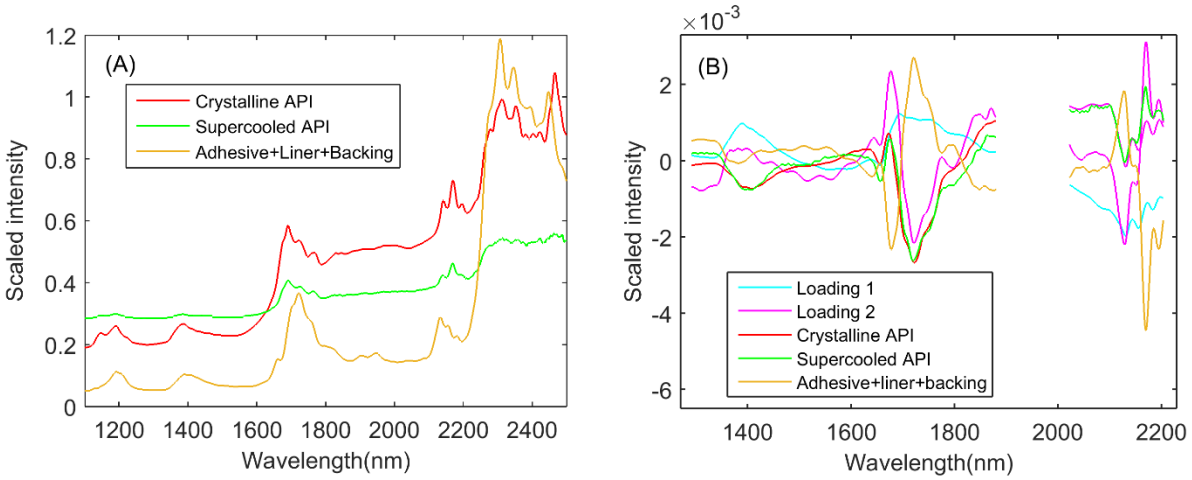

Figure 4.12 A: NIR spectra of pure components of DIA patches; B: An overlay of the first two loadings of the NIR PLS model and preprocessed NIR spectra of pure components of DIA patches. Plots were scaled to allow visual comparison.

The specificity of the developed methods was evaluated by comparing the loadings and the spectra of the pure components. The loading of the first PC of the Raman model exhibited the highest correlation with the spectrum of the crystalline API, whereas the second loading of the NIR model showed some overlaps with both API forms.

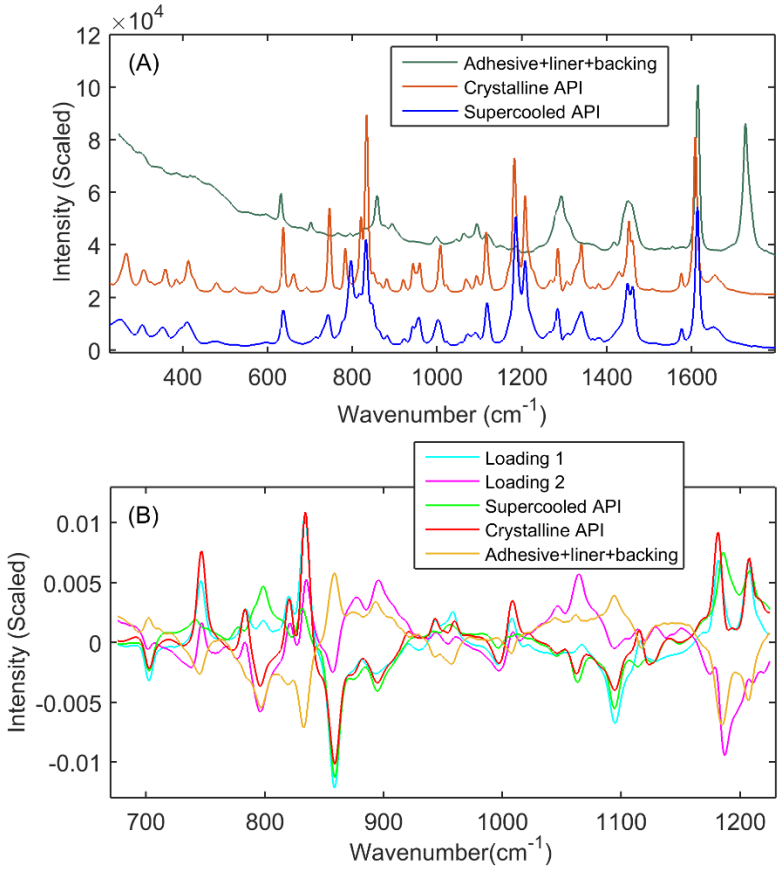

Figure 4.13 A: Raman spectra of DIA components; B: An overlay of the first two loadings of the Raman PLS model with preprocessed Raman spectra of pure components of DIA patches.

4.3.3.2 Precision

Precision describes the "closeness of agreement between a series of measurements obtained from multiple sampling of the same homogeneous sample under the prescribed conditions".[194] It is defined at three levels by the ICH Q2: repeatability, intermediate precision and reproducibility. Repeatability expresses the precision under the same operating conditions over a short interval of time. Repeatability is required for validation of assay methods. Intermediate precision considers variations within-laboratories: different days, different analysts and different equipments, etc. The extent to which intermediate precision is established is based on circumstances under which the

procedure is intended to be used. Reproducibility expresses the precision between laboratories. It is not necessary to test reproducibility if all analyses are accomplished in one laboratory.

Table 4.4 Precision results of the quantitative methods for crystalline content quantification

Method	NIR				Raman			
Crystallinity (%)	3.3	7.8	11.3	14.5	3.3	7.8	11.3	14.5
w/o repositioning (%)	0.10	0.12	0.09	0.15	0.14	0.15	0.11	0.39
repositioning (%)	0.16	0.26	0.32	0.24	0.26	0.37	0.54	0.68
intermediate (%)	0.14	0.33	0.37	0.48	0.47	0.51	0.57	0.87

The results of the repeatability and reproducibility of the two quantitative methods are summarized in Table 4.3. Precision was determined with patches of four crystallinity levels (3.3, 7.8, 11.3 and 14.5%) of the validation set. Except for the patches scanned with repositioning at the lowest crystallinity level (3.3%) via Raman, all three levels of the validation samples exhibited relative standard deviations smaller than 5.0%, representing consistent performance of the two analytical systems. It was noted that repositioning was the major contributor to precision error for Raman spectroscopy. As the laser spot size (1.5 mm) of the Raman analyzer is smaller than the size of the patch (15 mm), this error may be due to intra-patch heterogeneity. Intermediate precision was performed on three different days. The pooled standard deviation (SD) for samples scanned with repositioning on day one (0.31% for NIR and 0.60% for Raman) was similar to what were observed on a different day (0.33% for NIR and 0.67% for Raman).

4.3.3.3 Accuracy Profile

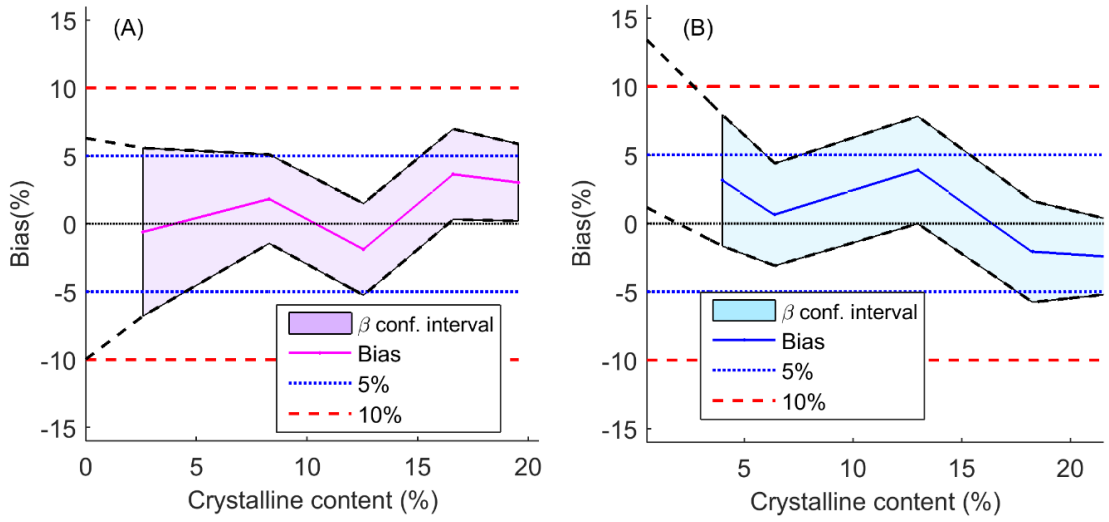

Figure 4.14 Accuracy profile for A: NIR method; B: Raman method.

The β tolerance intervals calculated with the NIR and the Raman methods are shown in Figure 4.13. The central solid line of Figure 4.13(A) represents the mean biases of NIR predicted crystallinity at five validation concentrations. The β tolerance interval was calculated from the relative standard deviations of the intermediate precision and it was normalized to the mean crystalline content. That explained why the width of the β intervals was the largest at the lowest crystalline content level. For both methods (NIR and Raman), the β intervals were contained within 10% at the crystalline content levels (3 to 22%) under evaluation, indicating the lower level of quantification is below 3.0%. However, this is only true when the bias is small (<5%). Two extrapolated lines from the lowest concentration of the validation set to 0% crystallinity were drawn to determine the concentrations at which the β interval exceeded ± 10%. Thus, the intersection between the accuracy profile and the acceptance limits defined the lower level of the dynamic range of the quantitative method. The lower level of the dynamic range of the Raman method was about 3.0% while it was not defined for NIR because the accuracy profile was confined in the 95% acceptance limits even at 0% crystallinity.

4.3.3.4 Multivariate Detection Limit

The multivariate detection limit (MDL) was calculated to facilitate model optimization and evaluation. The method is based on statistical analysis and error propagation. The MDL dependents on the accuracy of the reference method, instrumental noise, spectral interference and modeling error. The sources of error for the developed analytical methods are summarized in table 4.4. The reference method used in this study was a digital balance, its reference error was negligible. Spectral interference constituted less than 0.1% of the total prediction uncertainty. Comparatively, prediction residuals and calibration or model errors account for most of the prediction uncertainties.

Table 4.5 Sources of errors for the developed analytical methods.

Instrument	Sources of errors	Modeling error			Prediction error	
		Variance-cal. set	Reference error	Spectral error-cal. set	Spectral error-test set	Prediction residual-test set
NIR	Variance	0.198	0.006	1.42×10^{-6}	1.65×10^{-5}	1.53
	Percentage (%)	11.42	0.35	<0.001	<0.001	88.23
Raman	Variance	0.641	0.009	2.12×10^{-4}	2.99×10^{-4}	2.24
	Percentage (%)	22.18	0.31	<0.001	<0.001	77.51

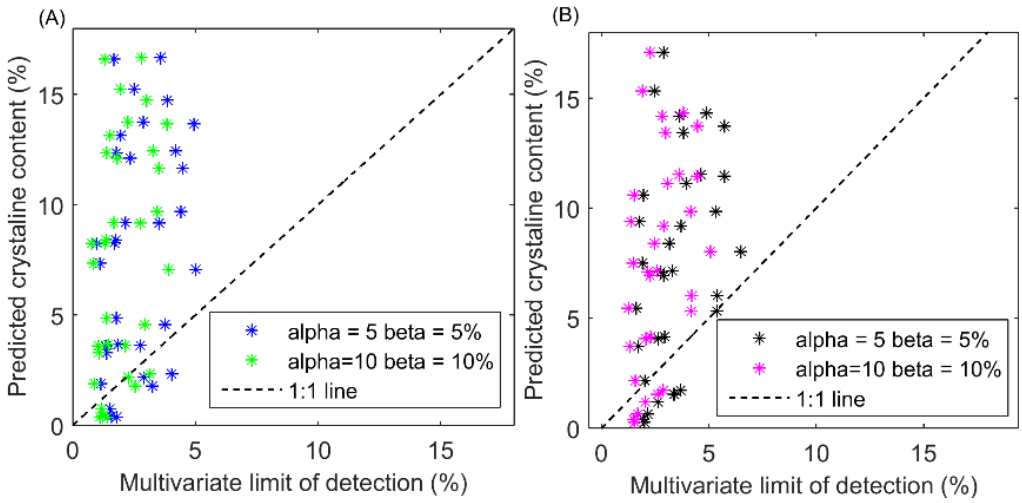

Figure 4.15 Multivariate detection limit of the test set samples based on A: the NIR method; B: the Raman method.

Multivariate detection limits determined from Equation (4.5) are sample specific because the calculation was performed with the information of each sample. Each sample has a leverage that increases with the concentration of the analyte. That is why the MDLs demonstrated in the Figure 4.14 are slightly greater for samples with high crystalline contents than those with low crystalline content. The dotted lines in Figure 4.14 (A) and (B) represent the cutoff values at which the predicted crystalline contents are equal to the MDLs, based on predefined type I and type II errors. The confidence of correctly predicted the crystallinity of samples found below this line is lower than the predefined confidence limit(s).

The MDLs estimated in this way were recorded in Table 4.5, along with the detection limits determined from IUPAC definition. The mean value of the MDLs of validation samples was used to represent the overall MDL. As the conventional LOD is defined as the lowest concentration of an analyte that can be distinguished from the blank, the LOD based on IUPAC was much smaller than the MDL. Using the LOD from IUPAC, the probability of stating there is no crystalline API in a patch which contains crystalline drug is low. In Figure 4.15, all samples spiked with crystalline API are observed above the LOD. However, the LOD was insufficient to reject blank samples.

The predicted concentrations of blank samples are greater than the LOD. Therefore, the error of detecting crystallinity in blank samples is high (high type I error). The blank samples can be distinguished from the crystalline drug-bearing samples given MDLs, suggesting MDL is a more stringent metric compared to the LOD.

The calculated MDLs enable direct comparisons of MDLs between different analytical instruments and modeling methods. Overall, the NIR method has lower detection limits compared to the Raman method. Based on the MDL at 5% of both α and β, the MDL for NIR is 2.67 or 0.63% w/w and 3.61 or 0.85% w/w for Raman. The NIR method can detect 10% drug recrystallization in a patch loaded with as little as 6.3% w/w drug; while the Raman method detects the same conversion percentage only when the drug concentration is greater than 8.5% w/w.

Table 4.6 Detection limits of NIR and Raman methods for crystalline content quantification of the API in DIA patches.

Detection Limit (%)	NIR	Raman
MDL (α = β = 0.10)	2.08	2.81
MDL (α = β = 0.05)	2.67	3.61
LOD (IUPAC, α = 0.05)	0.53	0.96

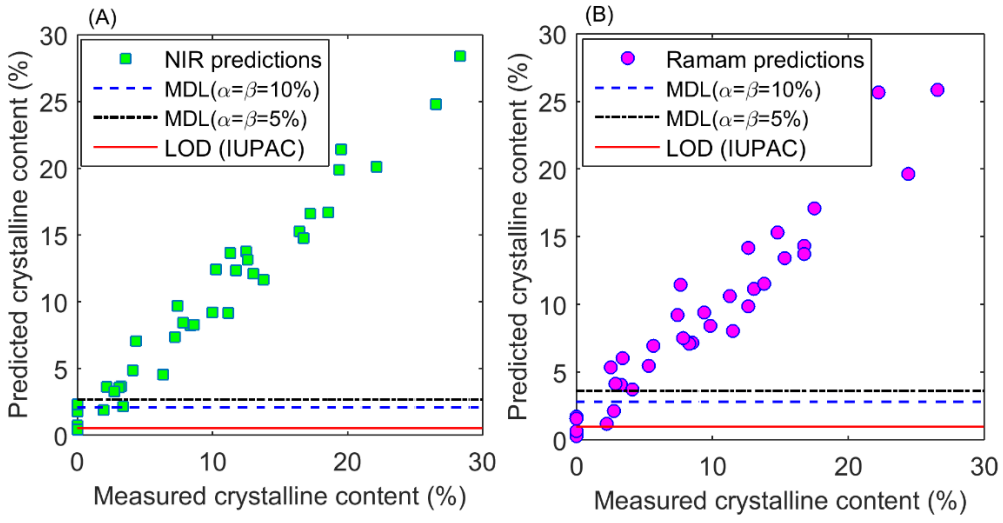

Figure 4.16 Comparisons of the predicted crystalline contents to MDL and LOD. A: The NIR method; B: The Raman method.

4.4 Conclusions

The aim of the study was to develop and validate analytical methods for the quantification of crystalline contents of the API in DIA patches. This study utilized a backscatter Raman spectrometer and a NIR spectrometer. The calibration models were developed from NIR and Raman spectra of patches spiked with crystalline drug according to a sample design that minimize the corrlation between the two physical forms of the API. The weight percentages of the crystaline drug spiked in the DIA patches were used as reference values. Two independent tests sets were prepared to verify the quantitave capability of the PLS models. The first test set was composed of spiked samples with a constant drug mass in order to keep a mass balance between the crystallized and solvated drug forms. The second test set contained the same drug concentrations as the first test set; while the samples in this set were initially free of spiked crystals. The crystallization in the second test set was continuously monitored until the crystalline contents reached a plateau. Strong correlations between the spectra of the two sets was found, showing the spectra of patches made by spiking crystals and from natural crystallization were very similar. Therefore, the spiking method was used to prepare validation samples.

The developed methods were validated using the fit-for-purpose concept. Accuracy profiles derived from biases and intermediate precisions related the method performance to the predefined acceptance criteria. The β-intervals constructed from the NIR and the Raman methods were contained in a predefined acceptability interval (±10 % crystallinity) across the three levels of concentration covering the validation domain. The prediction uncertainty of the method was calculated using an independent data set to yield sample-specific multivariate detection limits (MDL). The overall MDL of the Raman method is about 3.61% and the MDL of the NIR method is 2.67%, with a 5% type I and type II errors. Finally, the variance of the spectral signal was compared between the spiked and the naturally recrystallized samples using PC scores

and the diagnostic measures (Hotelling's T^2 and Q-residuals). Strong correlations between the Raman signals of the two systems were identified.

Development of reliable solid-state quantification methods is a critical component in understanding crystallization processes. The approach demonstrated in this chapter can be applied to develop analytical methods for physical stability studies. In this case, sample representativeness, analytical capability and method suitability were integrated to form a systematic approach for crystallization quantification. The developed approach enabled reliable predictions of crystalline drug content in DIA transdermal patches.

Chapter 5 : Monitoring Crystallization of Ibuprofen in Supersaturated Ibuprofen Duro-Tak®2052 Transdermal Patches

5.1 Background and Introduction

Supersaturated transdermal drug delivery systems have been utilized to improve the delivery of drugs through the skin. The unique advantage of supersaturated systems is that drug supersaturation provides an increased thermodynamic activity and thus improved skin permeation. However, DIA patches supersaturated with active pharmaceutical ingredients are thermodynamically unstable and are prone to recrystallization. Physical instability is the major hurdle that limits the application of supersaturation in transdermal drug delivery. [205] It is essential to understand the drug crystallization processes from the adhesive systems to enhance the physical stability of such systems. The objective of this chapter was to determine the crystallization kinetics of drug from a DIA system via vibrational spectroscopy. The information generated was used to understand the factors that affect the extent of drug crystallization.

Crystallization of ibuprofen in supersaturated Ibuprofen Duro-Tak® 2052 polyacrylate pressure sensitive adhesive patches was monitored by Raman spectroscopy. The crystallinity estimated from a PLS model was fitted by a Weibull function to determine the recrystallization kinetics. The degree of supersaturation was determined based on the saturation solubility of the API in the adhesive, considering the influence of environmental humidity. The risk of environmental factors was discussed on the basis of crystallization of APIs in DIA patches.

5.2 Experimental Methods

5.2.1 Materials and Storage Conditions

Transdermal patches for stability evaluation were prepared according to the target formulation (Section 2.2.1) and they were stored in desiccators with changing temperature (5, 25 and 45 °C) and humidity (11, 32 and 56 %RH). Saturated solutions of lithium chloride, magnesium chloride and magnesium nitrate were used to maintain corresponding relative humidifies. Patches were withdrawn from the stability chambers to collect Raman spectra at various sampling time points until the crystalline contents reached plateaus. Prior to spectroscopic measurements, the samples were equilibrated in a chamber with controlled temperature (25 °C) and humidity (56 %RH) for 30 min.

Table 5.1 Storage conditions used in the stability evaluation

Experimental condition	Humidity (% RH)	Temperature (°C)
1	32 ± 5	5 ± 2
2	11 ± 5	25 ± 2
3	32 ± 5	25 ± 2
4	56 ± 5	25 ± 2
5	32 ± 5	45 ± 2

5.2.2 Determination of Recrystallization Kinetics

The effects of temperature and relative humidity on the rate of crystallization was investigated. In Chapter 2, the patches showed preferential nucleation along the edges and at the interface between the liner and the adhesive. These observations suggest the nucleation is primarily heterogeneous, rather than homogenous. Avrami equation assumes homogeneous nucleation occurring randomly throughout the entire sample. Therefore, Avrami equation is not an

appropriate model to describe the kinetics of recrystallization in the DIA system. An assumption free, numerical function was selected to correlate model parameters to the rate of crystallization. The crystalline content determined from the Raman PLS model (Section 4.3.1.2) was fitted into a Weibull function:

$$X(t) = 1 - \mathrm{e}^{-(\frac{t}{a})^b} \tag{5.1}$$

where $X(t)$ is the relative crystallinity determined by dividing the crystallinity at each time point by the final crystallinity. *a* is the scale parameter and *b* is the shape parameter. At each level of relative humidity, the crystallinity determined from the Raman method were fitted in equation (5.1). The values of *a* and *b* were optimized by an unconstrained non-linear fitting method using MATLAB R2015a. The correlation coefficient, r^2, was utilized to determine the fit of the data to the Weibull function. Two parameters were used to analyze the crystallization rates at different humidty conditions. The half-crystallization time, t_{50}, was interpolated from the fitted curve. It represents the time at which the crystallization is half of the total relative crystallinity. The parameter $1/t_{50}$ was plotted as a function of the relative humdity emploeyd. The other parameter, X_{end}, denotes the percent crystallinity at the last time point and was used to represent the extent of drug crystallization at the end of the stability study.

5.2.3 Impact of Humidity on Drug Crystallization

The dependence of drug crystallization on humidity was determined by regressing the crystallization rate constant k with the RH%. After the crystallinity reached plateau, the solvated drug contents in the adhesive was used to determine the apparent solubility (C_s) for each temperature and humidity combination. The solubilities of API at humidity between 11 % RH and

56% RH were estimated by a linear interpolation. Therefore, the degree of supersaturation (S) of ibuprofen in the ibuprofen Duro-Tak® system can be calculated according to:

$$S = \frac{X_{total} - X_c}{C_s} \quad (5.4)$$

and

$$C_s = \frac{X_{total} - X_{end}}{X_{total}} \quad (5.5)$$

where X_{total} is the API content determined by UV analysis, X_c is the crystalline content detemrined from the Raman method, and X_{end} is the crystalline content at the end of stability study. A solid dispersion system with a degree of supersaturation smaller than 1 was considered to be thermodynamically stable whereas a degree of supersaturation greater than 1 is indicative of a physically unstable system under a cetain termperature and humdity. The plot of degree of supersaturation of the API in the DIA system can help to guide the selection of storage conditions for DIA patches.

5.3 Results and Discussion

5.3.1 Predicting Crystalline Contents of Samples Stored Under Stress Conditions

Ibuprofen was fully dissolved in the adhesive upon preparation. Only one crystalline phase (phase I) was expected because the storage conditions involved in the study were extremely unfavorable for polymorphic form II, which was identified after rapid quench of the melt at least 60 °C below the T_g of ibuprofen(-48 °C).[206] Any change in physical form, including crystal morphologies and density, may lead to changes in the spectroscopic responses. The spectroscopic variations unrelated with crystallinity were minimized with spectral preprocessing and variable

selection. From Chapter 5, the stability samples had very similar spectroscopic responses as that of the spiked samples. Therefore, the PLS models were used to predict the crystalline contents of naturally recrystallized patches.

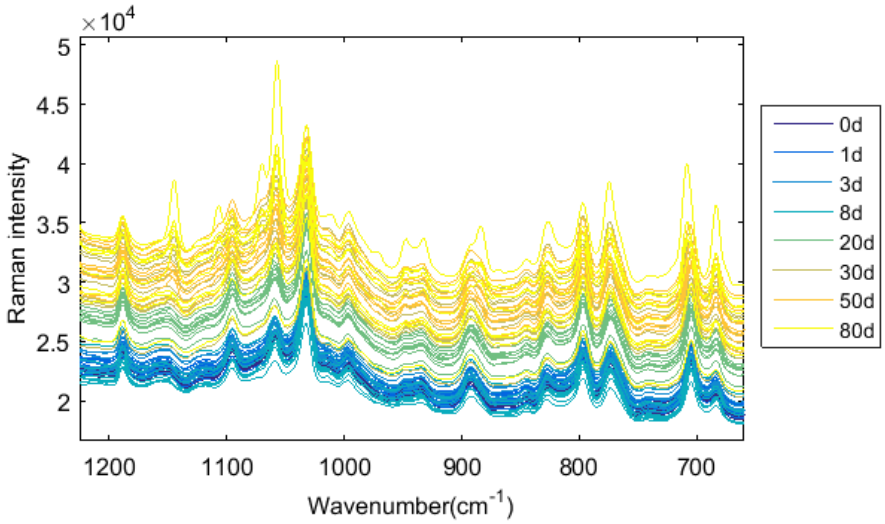

Figure 5.1 Raman spectra of samples used in the stability study.

The Raman spectra of samples stored for 80 days were plotted in the Figure 5.1. A progressive increase of the baseline was found. This may be related with changes of the sample systems, such as density changes and sorption of water. spectrometer drifts is also possible over this period of time. The baseline variation was removed by weighted least squares baseline removal and normalization to unit area. The crystalline contents were estimated using the developed Raman PLS model. The predicted crystalline contents at five humidity and humidity conditions are displayed in Figure 5.2.

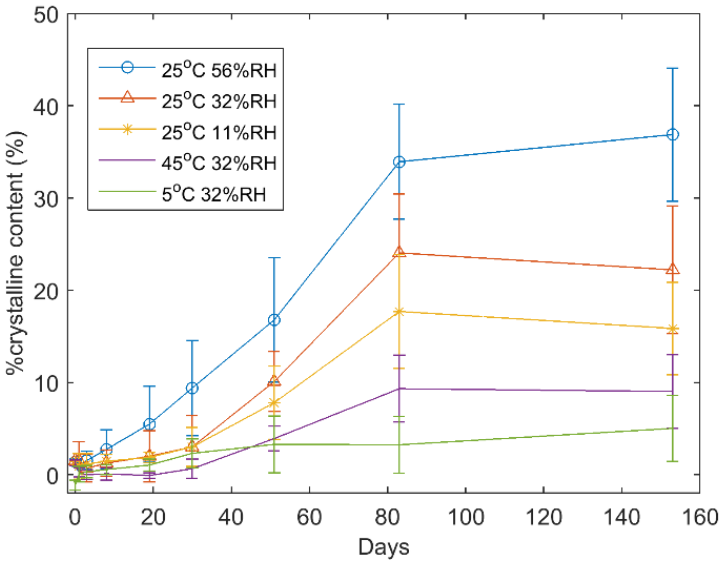

Figure 5.2 Crystalline contents of API in samples used in the stability study. The error bars represent the standard deviation of five replicates.

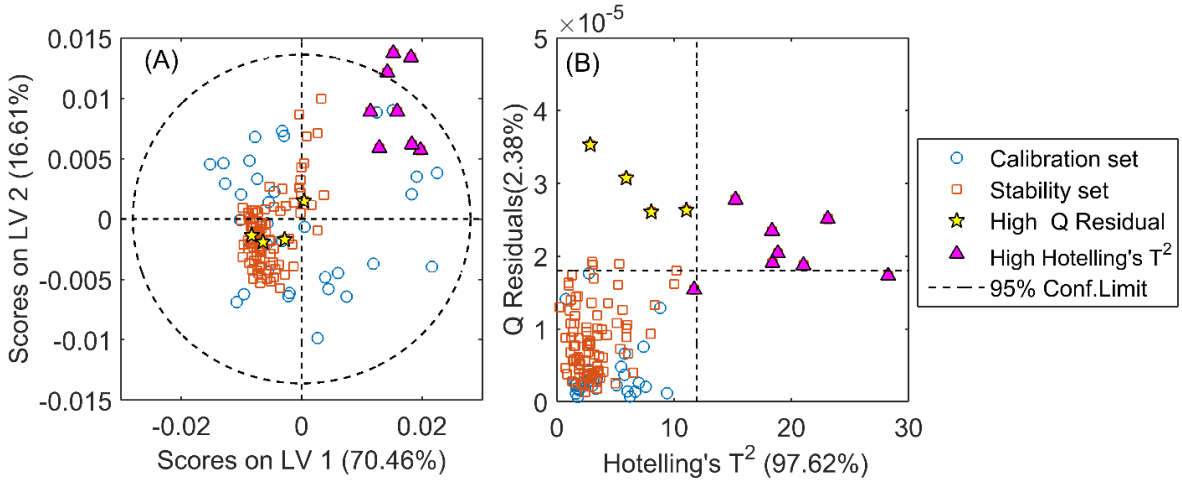

Figure 5.3 A: Scores of the first two latent variables of the Raman PLS model; B: Hotelling's T2 and Q-residuals of the calibration set, and the stability set.

Diagnostics, including Q-residuals and Hotelling's T^2, were used to determine if the models developed in the Chapter 4 span the variability of the stability samples. They also represent how models react to changes in input variability. The diagnostics of the majorities of the stability samples are contained within the 95% confidence intervals of the calibration set (Figure 5.3(B)). The stability samples, denoted by purple triangles, showed high Hotelling's T^2 and Q-residuals.

High Hotelling's T^2 indicates that the modeled variability has exceeded the calibration range. The calibration range was 0.0 - 28.0% in crystallinity while the crystalline contents of these samples were predicted to be higher than 30.0%. Four samples with low Hotelling's T^2 but high Q-residuals were marked by yellow pentagons. Although their corresponding scores are found within that of the calibration set, as is shown in Figure 5.3(A), the high Q-residuals may be associated with the spectral variations demonstrated in Figure 5.4.

The plot of diagnostics revealed there were unexpected variations detected by the Raman analyzer. The variations can result from sample density changes, instrument drift or measurement inconsistency. A part of the stability samples can be used to augment the calibration to span the variabilities of the calibration; alternatively, calibration samples can be stored in varying environmental conditions to incorporate the variability of temperature and humidity into the models.

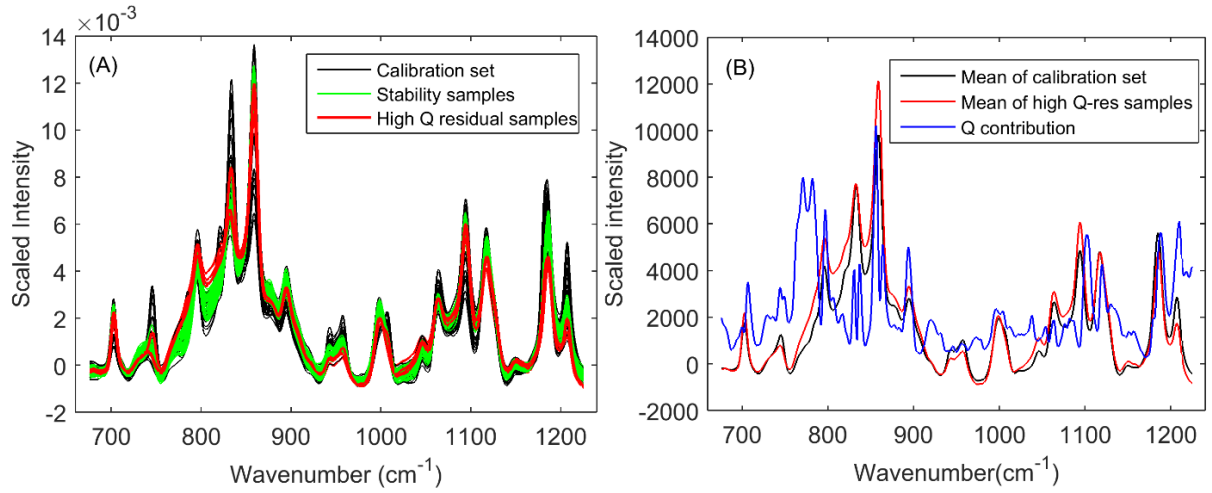

Figure 5.4 A: Preprocessed Raman spectra of calibration samples, samples for stability testing and samples with high Q-residuals. Preprocessing methods include weighted least squares baseline removal and normalization. B: An overlay of the mean of calibration spectra, the mean of high Q-residual sample spectra and Q-contribution plot.

5.3.2 Effect of Temperature on Physical Stability of the DIA System

The temperature and humidity had influences on both the extent and the rate of crystallization. The rate of crystallization first increased with temperature from 5 °C to 25 °C. However, as temperature further increased from 25 °C to 45 °C, a drop in the overall crystalline content with temperature was observed. The films stored at 45 °C had reached an equilibrium at around 2-3 month, as the crystallinity stayed unaltered afterwards. The crystallization kinetics are fast at such an elevated temperate (100 °C above the T_g of the system). Conversely, the patches stored at 5 °C may not have reached the equilibrium as crystallization is considerably slower with a temperature drop of 40 °C. A photo of the stability samples taken at the end of five months is shown in Figure 5.5. It demonstrated numbers and sizes of drug crystals of samples stored at 5 °C and 45 °C are lower than that of samples preserved at 25 °C.

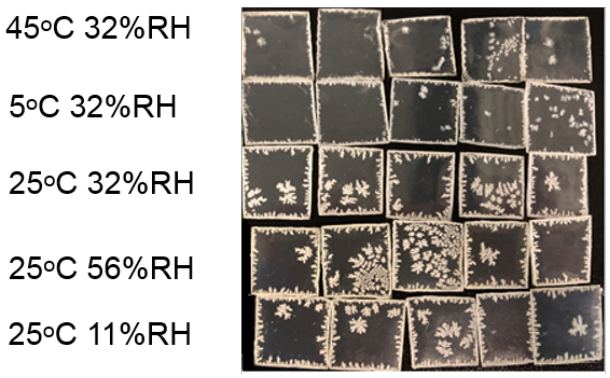

Figure 5.5 A photo of DIA patches prepared with 23.5 % w/w API and 76.5% w/w adhesive. The photo was taken at the end of a 6-month storage. Each row of sample corresponds to one of five storage conditions.

The observed phenomenon can be explained by considering kinetic and thermodynamic factors affecting crystallization. Kinetically, the molecular mobility increases with temperature. Both the nucleation and crystal growth rates increase with temperature. Thermodynamically, the crystallization is under complex influences of the degree of undercooling and supersaturation. Raising the temperature would lower the degree of undercooling but increase the solubility of API in the polymer. That is why the maximum crystallization rate is usually observed between the glass

transition temperature and the melting temperature. However, the crystallization does not follow Arrhenius relationship because of the wide temperature range used in the study.

5.3.3 Effect of Humidity on Physical Stability of the DIA System

An increase of crystallinity was observed in Figure 5.2 at higher humidity levels. The crystallinity at each time point was transformed to relative fractions, based on the crystallinities at the last time point. The crystallization profile was fit into a numerical function (Weibull) to understand the kinetics of drug recrystallization. The R^2 and t_{50} from the curve fitting are recorded in Table 5.2.

Table 5.2 Parameters calculated from curve fitting using a Weibull function

	b	*a*	R^2	t_{50}	X_{end}
25 °C 56%RH	2.09	59.86	0.993	49.2	37.9
25 °C 32%RH	2.58	62.50	0.998	52.5	22.7
25 °C 11%RH	2.37	64.70	0.999	54.5	16.8

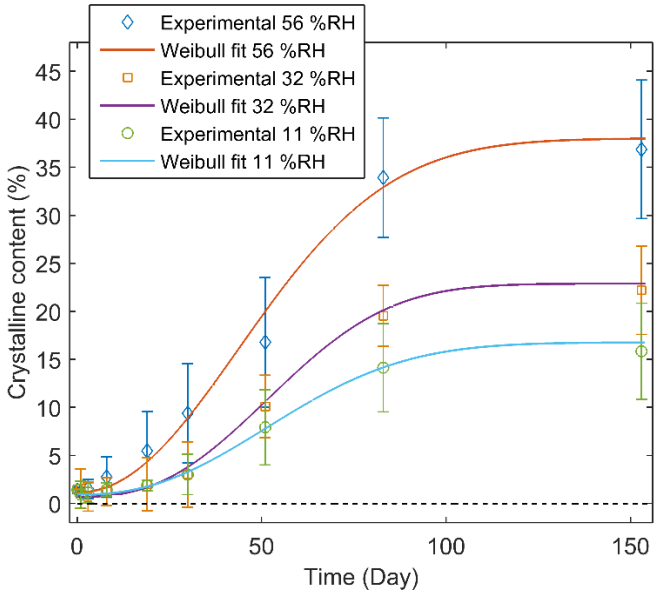

Figure 5.6 Crystallinity as a function of time for DIA patches (23.5%w/w API and 76.5%w/w adhesive) stored at 25 °C and three relative humidity conditions (56 %RH, 32 %RH and 11 %RH).

The rate of crystallization changed linearly with the relative humidity. This is demonstrated by plotting $1/t_{50}$ as a function of relative humidity (see Figure 5.7). There are many theories that explain why environmental water leads to faster crystallization. Hancock, Zografi and Marsac described the phenomenon as a result of water-induced plasticization and ensuing enhanced molecular mobility. [122, 207]

Crowley and Zografi proposed that the absorbed water decreases the API solubility in the polymer by competing with the API to bind with the polymer at the hydrogen bonding sites. This changes the equilibrium between the bound API and the free API, resulting in an increase in the API that are free to form crystals.[208-210] The process is demonstrated in Figure 5.8. Chenevas-Paule proposed that incorporation of drug molecules in the acrylate polymers leads to breakage of intramolecular H-bonds between polymer chains of the adhesive.[210] The interaction between drug-acrylic polymers further increased the number of water-binding sites. This process promotes to drug release and is referred to the "hydration effect" in DIA patches".[210] However, this

phenomenon also points out the detrimental effect of environmental humidity on the physical stability of DIA films.

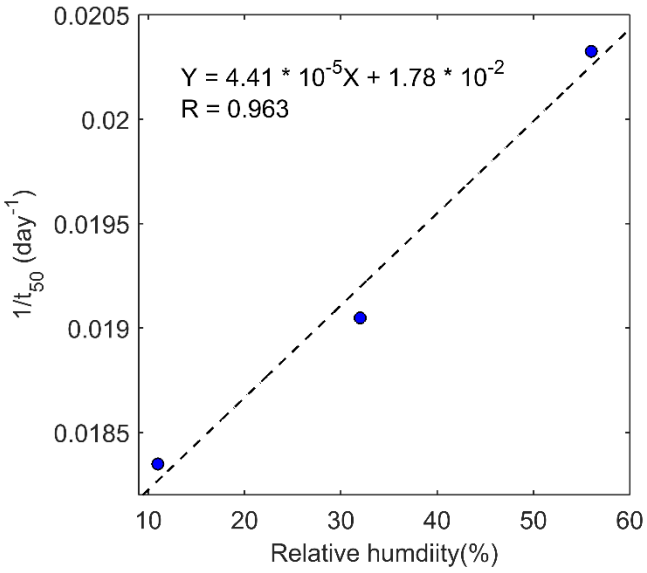

Figure 5.7 Inverse of experimental crystallization half time as a function of relative humidity.

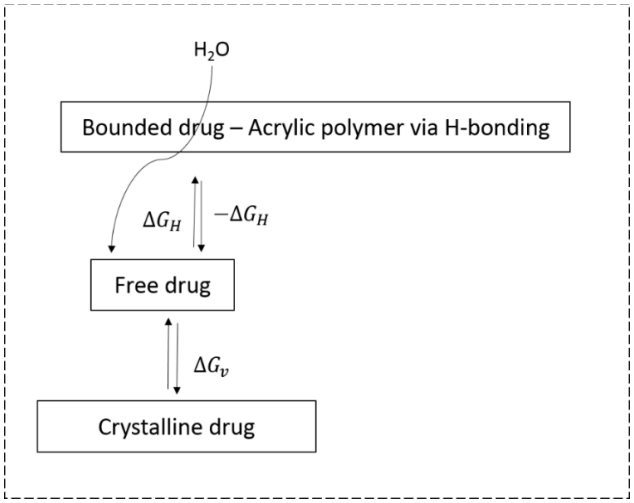

Figure 5.8 Adapted from Chenevas-Paule and Dodou.[210] The process of water competing with the API at the H-boinding sites of the polymer and its effect on recrystallization.[e]

[e] Adapted from Development of a Predictive Model for the Long-Term Stability Assessment of Drug-In-Adhesive Transdermal Films Using Polar Pressure-Sensitive Adhesives as Carrier/Matrix, 165(3), Chenevas-Paule C, Wolff H-M, Ashton M, Schubert M, Dodou K, 1293-1301., Copyright (2017), with permission from Elsevier.

The degree of supersaturation can be used as an indicator of physical stability of DIA systems. Figure 5.9 shows the supersaturation of ibuprofen in Duro-Tak® 2052 at varying compositions and relatvie humdity under isothermal conditions. The plot was seperated into upper and lower regions representing where the degree of supersaturation was lower and higher than 1, respectively. When the concentration of the API in the DIA system is lower than the solubility, *i.e.* $S < 1$, the system is considered thermodynamically stable; whereas the concentration of the API in the system is higher than the solubility, or $S > 1$, the solvated drug is unstable and tend to recrystallize. The type of nucleation expected relative to the value of S is commonly described by a solublity map.[211-212] When $S >> 1$, homogenous nucleation is energetically permissible, and the supersatured solution is in the labile zone. When S is close to 1, the system is in the metastable zone. Heterogeneous nulcleation and seondary nucleation are more prevalent in the metastable zone. At a concentration of 23.5 % w/w and a solublity of 16.17 % w/w, the degree of supersaturation of the DIA system is 1.45. This value of S suggests that the nucleation in the system is heterogeneous, which agrees with the observation that the crystallization was predominantly at the patch edges and interfaces.

It can be observed from Figure 5.9 that the degree of supersaturation increased with both API concentartion and relative humidity. As a passive transdermal delivery sytem, the DIA system is typically loaded with a supersaturated amount of the API. At differnet humdity levels, the patch system exhibits different extent of physical stability. For example, a 18% w/w drug-adhesive film has a degree of supersaturation of 0.93 if it is stored at 11% RH; thus it would not recrystallze at this storage condition. However, a film with the same composition is more likely to crystallize if the hudimity increased to 56%RH since the drug concentration is higher than its solubility in the adhesive. This plot reiterate the importance of packaging and storing of transdermal patches.

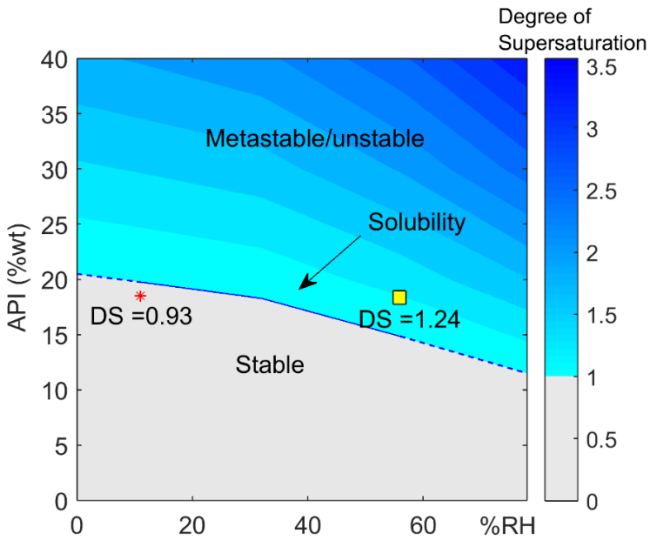

Figure 5.9 Degree of supersaturation of ibuprofen as a function of relative humidity.

5.4 Conclusions

The crystallization can be described by two distinct yet inseparable processes: nucleation and crystal growth. The nucleation and crystal growth processes in supersaturated DIA patches are expected to vary with the crystallization temperature. The higher the temperature, the greater the thermodynamic driving force for crystallization. The crystallization rate constant is expected to increase exponentially with temperature within the proposed range of temperature according to the Arrhenius equation. However, the solubility of the drug increases with the temperature and that reduces the degree of supersaturation which favors crystallization. Water, on the other hand, plasticizes the solid dispersions and promote to greater molecular mobility in the system.

In this chapter, the crystallization kinetics of iburpfen in DIA patches was determined non-destructively by Raman spectroscopy. The predicted crystallinity was used to calculate the crystallization rate($1/t_{50}$) and degree of supersaturation of API in adhesive at varying humidity conditions. These information were related to factors that impact the physical stability. The

maximum recrystallization rate was observed at a temperature above T_g and below T_m. The presence of water in the environment reduces the physical stability of the ibuprofen Duro-Tak® patches. The extent and rate of recrystallization both increased with relative humidity.

Chapter 6 : Summary

The stability of pharmaceuticals encompasses various aspects: chemical, physical and microbiological. Physical stability refers to the ability of a product to maintain its physical dimensions and properties during the shelf-life. Physical changes are often more difficult to quantitate and with poor predictability compared to chemical stability.[13] A sensitive and selective analytical tool for quantitative assessment of the drug crystallinity in pharmaceutical products allows for testing of different formulations and observation of the effect of those formulations on the recrystallization kinetics. Fundamental understanding of mechanisms of physical variations is essential to achieve robust formulations and must be incorporated in the drug and drug product developments.

The recrystallization of a solvated drug in a DIA transdermal patch potentially hampers drug solubility, permeability and bioavailability. The extent of recrystallization must be closely monitored to reveal factors affecting crystallization. A quantitative method that is specific and sensitive to the crystalline form of the API facilitates the understanding of the mechanisms behind physical changes of pharmaceuticals. However, challenges are associated with quantification of solid phases in transdermal drug delivery system. The traditional solid-state quantification methods, which serve as reference methods, suffer from poor sensitivity. In addition, it is extremely difficult to achieve a homogeneous distribution of the crystalline and the solvated phases in the physical mixtures. Sources of errors linked to solid-state quantification in transdermal films have not been reported.

This dissertation has demonstrated the analytical capability of NIR and Raman spectroscopy for crystalline content quantification in a drug-in-adhesive transdermal patch system.

Rigorous evaluations of feasibility and performance of the analytical systems for crystalline content determination were conducted. The measurement setups, suitability of spiked samples, analytical sensitivity and selectivity, and validation strategy were included in the evaluations.

A few practical investigations of the drug-in-adhesive systems were conducted in the early-stage development of the spectroscopic methods. That included the characterization of the physicochemical properties of the DIA system and the determination of potential effects formulation variables had on spectra. These characteristics, including drug content and solubility of the API in the adhesive, are of relevance to understanding the variability of the analytical results. This information can also guide the initial establishment of a regression function using a suitable dynamic range.

An artificial system that maximizes the spectral similarity to the naturally recrystallized patches were developed. The combination of two drug layers with distinct physical state (crystalline and solvated) makes crystallinity in each patch controllable. This method allows the generation of homogenous distributed crystalline particles within the patches. Recrystallization due to spiking was found to be insignificant in the time frame needed to complete measurements. With abundant information generated regarding the attributes of the spiked samples, the sample system prepared by coating were used for calibration.

The assessment of the analytical capability should be conducted prior to analytical method development. As the assessment only uses a reduced number of samples relative to the calibration experiment, it is particularly useful when time and resources are limited. The analytical capabilities for determination of crystalline content in a DIA formulation via the NIR and Raman instruments were demonstrated in this dissertation. The sensitivity of an analytical tool for crystallinity determination cannot be thoroughly justified without comparison to a reference method. The

effective resolution, a quantifiable sensitivity measure, was calculated for the spiked and crystal-free DIA patches using a backscatter Raman analyzer, a reflectance NIR spectrometer and an XRD diffractometer. The highest sensitivity, or the ability to detect crystalline API at the lowest concentration, is associated with the NIR system due to its outstanding signal to noise ratio. The selectivity for an analytical method was inferred from the accuracy of the predictions when interferences were varied. Both the Raman and the NIR preliminary models provided similar and accurate crystallinity predictions despite alternations of the substrate solvated drug concentrations. Thus, this part of the dissertation demonstrated the feasibility of the selected techniques to calibrate crystalline drug in spiked DIA patches.

The importance of rigorous sample design and understanding at all levels the sample variability and difference between spiked and authentic samples was demonstrated in this dissertation. In the calibration set, the concentrations of the crystalline drug and solvated drug were added with minimized correlation in compositions. This step is necessary as there is a strong spectral correlation between the two phases of the API. After the quantitative methods were established, the validity of the spiking method was carefully evaluated using two independent test sets. The first test set consisted of spectra of crystal-free samples, which were measured as they underwent recrystallization during storage. The second test set contained spectra of spiked samples with the same drug content to that of the first test set (their crystalline contents were varied to simulate the recrystallization process). A high degree of correlation was found between the spiked and the recrystallized samples in terms of predicted crystallinity and their corresponding spectra.

Method validation based on a fit-for-purpose concept was used to generate figures of merit for analytical methods. These figures of merit are specificity, accuracy, precision and multivariate detection limits (MDL). The MDL was used to set the dynamic range of the multivariate models.

The traditional LOD threshold, based on 3σ, is defined for univariate calibrations and it almost always gives an unrealistic detection limit because very few sources of errors are considered. The dissertation demonstrated multivariate detection limits for the NIR and the Raman methods, taking into accounts the uncertainties involved in all steps of the calibration and predictions. An accuracy profile derived from biases and intermediate precisions related the method performance to the predefined acceptance criteria. The β-intervals constructed from the NIR and the Raman methods were contained in the acceptability interval (±10% crystallinity) across the calibration range, demonstrating methods are validate for crystallinity quantification in the chosen DIA system.

The spectroscopic methods for solid-state quantification have the potential to enhance the efficiency of stability studies. The fast measurement speed minimizes the risk of exposing samples to uncontrolled environmental conditions. The Raman method was applied to DIA patches to determine the recrystallization kinetics and understand the impact of environmental factors on the rate of drug crystallization. The degree of supersaturation of the drug in a DIA patch increased with environmental humidity, reiterating the importance of packaging and storing of DIA transdermal patches.

The work presented a novel approach for evaluating physical stability of transdermal drug products through careful calibration and validation of the analytical methods. A systematic approach that determines the feasibility, capability and performance of analytical methods allows for accurate analysis of crystalline content in recrystallized DIA systems with improved sensitivity and selectivity. As determination of the physical stability of solid-state pharmaceuticals remains to a challenge, the current methodology offers a means to understand the interplay between formulation factors, crystallization and drug release.

REFERENCES

1. Jung, E.; Lee, E. Y.; Choi, H.-K.; Ban, S.-J.; Choi, S.-H.; Kim, J. S.; Yoon, I.-S.; Kim, D.-D., Development of Drug-in-Adhesive Patch Formulations for Transdermal Delivery of Fluoxetine: In Vitro and in Vivo Evaluations. *Int. J. Pharm.* **2015,** *487* (1), 49-55.

2. Mitragotri, S., Breaking the Skin Barrier. *Adv. Drug Deliv. Rev.* **2004,** *56* (5), 555-6.

3. Prausnitz, M. R.; Langer, R., Transdermal Drug Delivery. *Nat. Biotechnol.* **2008,** *26*, 1261.

4. Pastore, M. N.; Kalia, Y. N.; Horstmann, M.; Roberts, M. S., Transdermal Patches: History, Development and Pharmacology. *Br. J. Pharmacol.* **2015,** *172* (9), 2179-209.

5. Rai, V.; Raghavan, L., Transdermal Drug Delivery Systems Using Supersaturation. In *Percutaneous Penetration Enhancers Chemical Methods in Penetration Enhancement: Drug Manipulation Strategies and Vehicle Effects*, Dragicevic, N.; Maibach, H. I., Eds. Springer Berlin Heidelberg: Berlin, Heidelberg, 2015; pp 151-161.

6. Jain, P.; Banga, A. K., Inhibition of Crystallization in Drug-in-Adhesive-Type Transdermal Patches. *Int. J. Pharm.* **2010,** *394* (1-2), 68-74.

7. Edwards, A.; Qi, S.; Liu, F.; Brown, M. B.; McAuley, W. J., Rationalising Polymer Selection for Supersaturated Film Forming Systems Produced by an Aerosol Spray for the Transdermal Delivery of Methylphenidate. *Eur. J. Pharm. Biopharm.* **2017,** *114*, 164-174.

8. Sharma, P. K.; Panda, A.; Pradhan, A.; Zhang, J.; Thakkar, R.; Whang, C.-H.; Repka, M. A.; Murthy, S. N., Solid-State Stability Issues of Drugs in Transdermal Patch Formulations. *AAPS PharmSciTech* **2018,** *19* (1), 27-35.

9. Chaudhuri, K. R., Crystallisation within Transdermal Rotigotine Patch: Is There Cause for Concern? *Expert Opin. Drug Deliv.* **2008,** *5* (11), 1169-1171.

10. Variankaval, N.; Jacob, K.; Dinh, S., Crystallization of B - Estradiol in an Acrylic Transdermal Drug Delivery System. *J. Biomed. Mater. Res.* **1999,** *44* (4), 397-406.

11. David B. LeboJuny LeeVincent LuisiJe Phil RyooOliver J. Toigo, I. Transdermal Tulobuterol Delivery. 2004.

12. Feth, M. P.; Volz, J.; Hess, U.; Sturm, E.; Hummel, R. P., Physicochemical, Crystallographic, Thermal, and Spectroscopic Behavior of Crystalline and X-Ray Amorphous Ciclesonide. *J. Pharm. Sci.* **2008,** *97* (9), 3765-80.

13. Guo, Y.; Shalaev, E.; Smith, S., Physical Stability of Pharmaceutical Formulations: Solid-State Characterization of Amorphous Dispersions. *TrAC, Trends Anal. Chem.* **2013,** *49*, 137-144.

14. RI., C., *Symmetry in Crystallography A2*. Oxford: Academic Press: 2017.

15. Saerens, L.; Dierickx, L.; Quinten, T.; Adriaensens, P.; Carleer, R.; Vervaet, C.; Remon, J. P.; De Beer, T., In-Line Nir Spectroscopy for the Understanding of Polymer-Drug Interaction During Pharmaceutical Hot-Melt Extrusion. *Eur. J. Pharm. Biopharm.* **2012,** *81* (1), 230-7.

16. Sinclair, W.; Leane, M.; Clarke, G.; Dennis, A.; Tobyn, M.; Timmins, P., Physical Stability and Recrystallization Kinetics of Amorphous Ibipinabant Drug Product by Fourier Transform Raman Spectroscopy. *J. Pharm. Sci.* **2011,** *100* (11), 4687-99.

17. Okumura, T.; Otsuka, M., Evaluation of the Microcrystallinity of a Drug Substance, Indomethacin, in a Pharmaceutical Model Tablet by Chemometric Ft-Raman Spectroscopy. *Pharm. Res.* **2005,** *22* (8), 1350-7.

18. Palermo, R. N.; Short, S. M.; Anderson, C. A.; Tian, H.; Drennen, J. K., Determination of Figures of Merit for near-Infrared, Raman and Powder X-Ray Diffraction by Net Analyte Signal Analysis for a Compacted Amorphous Dispersion with Spiked Crystallinity. *J. Pharm. Innov.* **2012,** *7* (2), 56-68.

19. (EMA), E. M. A., Guideline on Quality of Transdermal Patches, Ema/Chmp/Qwp/608924/2014 London, 2014.

20. Nunes, C.; Mahendrasingam, A.; Suryanarayanan, R., Quantification of Crystallinity in Substantially Amorphous Materials by Synchrotron X-Ray Powder Diffractometry. *Pharm. Res.* **2005,** *22* (11), 1942-1953.

21. Lust, A.; Strachan, C. J.; Veski, P.; Aaltonen, J.; Heinämäki, J.; Yliruusi, J.; Kogermann, K., Amorphous Solid Dispersions of Piroxicam and Soluplus®: Qualitative and Quantitative Analysis of Piroxicam Recrystallization During Storage. *Int. J. Pharm.* **2015,** *486* (1), 306-314.

22. Widjaja, E.; Kanaujia, P.; Lau, G.; Ng, W. K.; Garland, M.; Saal, C.; Hanefeld, A.; Fischbach, M.; Maio, M.; Tan, R. B., Detection of Trace Crystallinity in an Amorphous System Using Raman Microscopy and Chemometric Analysis. *Eur. J. Pharm. Sci.* **2011,** *42* (1-2), 45-54.

23. Strasinger, C.; Raney, S. G.; Tran, D. C.; Ghosh, P.; Newman, B.; Bashaw, E. D.; Ghosh, T.; Shukla, C. G., Navigating Sticky Areas in Transdermal Product Development. *J. Control. Release* **2016,** *233*, 1-9.

24. Graham, J.; Banaschewski, T.; Buitelaar, J.; Coghill, D.; Danckaerts, M.; Dittmann, R.; Döpfner, M.; Hamilton, R.; Hollis, C.; Holtmann, M., European Guidelines on Managing Adverse Effects of Medication for Adhd. *Eur. Child Adolesc. Psychiatry* **2011,** *20* (1), 17-37.

25. Wiedersberg, S.; Guy, R. H., Transdermal Drug Delivery: 30+ Years of War and Still Fighting! *J. Control. Release* **2014,** *190*, 150-156.

26. Mehdizadeh, A.; Toliate, T.; Rouini, M. R.; Abashzadeh, S.; Dorkoosh, F., Design and in Vitro Evaluation of New Drug-in-Adhesive Formulations of Fentanyl Transdermal Patches. *Acta Pharm.* **2004,** *54* (4), 301-17.

27. Lake, Y.; Pinnock, S., Improved Patient Acceptability with a Transdermal Drug-in-Adhesive Oestradiol Patch. *Aus. N. Z. J. Obstet. Gynaecol.* **2000,** *40* (3), 313-6.

28. Tan, H. S.; Pfister, W. R., Pressure-Sensitive Adhesives for Transdermal Drug Delivery Systems. *Pharm. Sci. Technol. Today* **1999,** *2* (2), 60-69.

29. Ghosh, T. K.; Pfister, W.; Yum, S. I., *Transdermal and Topical Drug Delivery Systems*. Taylor & Francis: 1997.

30. Schlademan, J., *Handbook of Pressure Sensitive Adhesive Technology*. New York: Satas Donatas: 1989; p 396-456.

31. Benedek, I., *Pressure-Sensitive Adhesives and Applications*. Taylor & Francis: 2004.

32. Benedek, I.; Feldstein, M. M., *Technology of Pressure-Sensitive Adhesives and Products*. CRC Press: 2008.

33. van der Maaden, K.; Jiskoot, W.; Bouwstra, J., Microneedle Technologies for (Trans)Dermal Drug and Vaccine Delivery. *J. Control. Release* **2012,** *161* (2), 645-655.

34. Prausnitz, M. R.; Langer, R., Transdermal Drug Delivery. *Nature biotechnol.* **2008,** *26* (11), 1261-1268.

35. Kanitakis, J., Anatomy, Histology and Immunohistochemistry of Normal Human Skin. *Eur. J. Dermatol.* **2002,** *12* (4), 390-401.

36. Bouwstra, J. A.; de Graaff, A.; Gooris, G. S.; Nijsse, J.; Wiechers, J. W.; van Aelst, A. C., Water Distribution and Related Morphology in Human Stratum Corneum at Different Hydration Levels. *J. Invest. Dermatol.* **2003,** *120* (5), 750-758.

37. Ma, J.; Gao, Y.; Sun, Y.; Ding, D.; Zhang, Q.; Sun, B.; Wang, M.; Sun, J.; He, Z., Tissue Distribution and Dermal Drug Determination of Indomethacin Transdermal-Absorption Patches. *Drug Deliv. Transl. Res.* **2017,** *7* (5), 617-624.

38. Behl, C. R.; Flynn, G. L.; Kurihara, T.; Harper, N.; Smith, W.; Higuchi, W. I.; Ho, N. F.; Pierson, C. L., Hydration and Percutaneous Absorption: I. Influence of Hydration on Alkanol Permeation through Hairless Mouse Skin. *J. Invest. Dermatol.* **1980,** *75* (4), 346-52.

39. Marjukka Suhonen, T.; Bouwstra, J. A.; Urtti, A., Chemical Enhancement of Percutaneous Absorption in Relation to Stratum Corneum Structural Alterations. *J. Control. Release* **1999,** *59* (2), 149-61.

40. Kligman, A. M., Hydration Injury to Human Skin. *Bioengineering of the Skin: Water and the Stratum corneum. Elsner P, Berardesca E, Maibach HI (eds). CRC Press, Boca Raton* **1994**, 251-255.

41. Hadgraft, J., Skin, the Final Frontier. *Int. J. Pharm.* **2001,** *224* (1-2), 1-18.

42. Moser, K.; Kriwet, K.; Naik, A.; Kalia, Y. N.; Guy, R. H., Passive Skin Penetration Enhancement and Its Quantification in Vitro. *Eur. J. Pharm. Biopharm.* **2001,** *52* (2), 103-112.

43. Higuchi, T., Physical Chemical Analysis of Percutaneous Absorption Process from Creams and Ointments. *J. Soc. Cosmet. Chem.* **1960,** *11*, 85-97.

44. Siepmann, J.; Siepmann, F., Modeling of Diffusion Controlled Drug Delivery. *J. Control. Release* **2012,** *161* (2), 351-362.

45. Vergnaud, J.-M., *Controlled Drug Release of Oral Dosage Forms*. CRC Press: 1993.

46. Takeru, H., Rate of Release of Medicaments from Ointment Bases Containing Drugs in Suspension. *J. Pharm. Sci.* **1961,** *50* (10), 874-875.

47. Tang J; Deverich JM; Miller JM; RD, B. Amorphous Drug Transdermal Systems, Manufacturing Methods, and Stabilization.Us Patent Application 0226698 A1,Mylan Technologies, Inc. 2008.

48. Vakili, H.; Kolakovic, R.; Genina, N.; Marmion, M.; Salo, H.; Ihalainen, P.; Peltonen, J.; Sandler, N., Hyperspectral Imaging in Quality Control of Inkjet Printed Personalised Dosage Forms. *Int. J. Pharm.* **2015,** *483* (1), 244-249.

49. Janßen, E. M.; Schliephacke, R.; Breitenbach, A.; Breitkreutz, J., Drug-Printing by Flexographic Printing Technology - a New Manufacturing Process for Orodispersible Films. *Int. J. Pharm.* **2013,** *441* (1-2), 818-825.

50. Frenot, A.; Chronakis, I. S., Polymer Nanofibers Assembled by Electrospinning. *Curr. Opin. Colloid Interface Sci.* **2003,** *8* (1), 64-75.

51. Buanz, A. B.; Belaunde, C. C.; Soutari, N.; Tuleu, C.; Gul, M. O.; Gaisford, S., Ink-Jet Printing Versus Solvent Casting to Prepare Oral Films: Effect on Mechanical Properties and Physical Stability. *Int. J. Pharm.* **2015,** *494* (2), 611-8.

52. Vakili, H.; Kolakovic, R.; Genina, N.; Marmion, M.; Salo, H.; Ihalainen, P.; Peltonen, J.; Sandler, N., Hyperspectral Imaging in Quality Control of Inkjet Printed Personalised Dosage Forms. *Int. J. Pharm.* **2015,** *483* (1-2), 244-9.

53. Hsu, H. Y.; Toth, S. J.; Simpson, G. J.; Taylor, L. S.; Harris, M. T., Effect of Substrates on Naproxen-Polyvinylpyrrolidone Solid Dispersions Formed Via the Drop Printing Technique. *J. Pharm. Sci.* **2013,** *102* (2), 638-48.

54. Janßen, E. M.; Schliephacke, R.; Breitenbach, A.; Breitkreutz, J., Drug-Printing by Flexographic Printing Technology—a New Manufacturing Process for Orodispersible Films. *Int. J. Pharm.* **2013,** *441* (1–2), 818-825.

55. Frederiksen, K.; Guy, R. H.; Petersson, K., Formulation Considerations in the Design of Topical, Polymeric Film-Forming Systems for Sustained Drug Delivery to the Skin. *Eur. J. Pharm. Biopharm.* **2015,** *91*, 9-15.

56. Démuth, B.; Farkas, A.; Pataki, H.; Balogh, A.; Szabó, B.; Borbás, E.; Sóti, P. L.; Vigh, T.; Kiserdei, É.; Farkas, B.; Mensch, J.; Verreck, G.; Van Assche, I.; Marosi, G.; Nagy, Z. K., Detailed Stability Investigation of Amorphous Solid Dispersions Prepared by Single-Needle and High Speed Electrospinning. *Int. J. Pharm.* **2016,** *498* (1–2), 234-244.

57. Macri, L. K.; Sheihet, L.; Singer, A. J.; Kohn, J.; Clark, R. A. F., Ultrafast and Fast Bioerodible Electrospun Fiber Mats for Topical Delivery of a Hydrophilic Peptide. *J.Control. Release* **2012,** *161* (3), 813-820.

58. Seif, S.; Franzen, L.; Windbergs, M., Overcoming Drug Crystallization in Electrospun Fibers--Elucidating Key Parameters and Developing Strategies for Drug Delivery. *Int. J. Pharm.* **2015,** *478* (1), 390-7.

59. Garvie-Cook, H.; Frederiksen, K.; Petersson, K.; Guy, R. H.; Gordeev, S., Characterization of Topical Film-Forming Systems Using Atomic Force Microscopy and Raman Microspectroscopy. *Mol. Pharmaceutics* **2015,** *12* (3), 751-757.

60. Zhang, J.; Ying, Y.; Pielecha-Safira, B.; Bilgili, E.; Ramachandran, R.; Romanach, R.; Dave, R. N.; Iqbal, Z., Raman Spectroscopy for in-Line and Off-Line Quantification of Poorly Soluble Drugs in Strip Films. *Int. J. Pharm.* **2014,** *475* (1-2), 428-37.

61. Hammes, F.; Hille, T.; Kissel, T., Reflectance Infrared Spectroscopy for in-Line Monitoring of Nicotine During a Coating Process for an Oral Thin Film. *J. Pharm. Biomed. Anal.* **2014,** *89*, 176-82.

62. Qi, S.; Moffat, J. G.; Yang, Z., Early Stage Phase Separation in Pharmaceutical Solid Dispersion Thin Films under High Humidity: Improved Spatial Understanding Using Probe-Based Thermal and Spectroscopic Nanocharacterization Methods. *Mol. Pharmaceutics* **2013,** *10* (3), 918-930.

63. Park, J. B.; Prodduturi, S.; Morott, J.; Kulkarni, V. I.; Jacob, M. R.; Khan, S. I.; Stodghill, S. P.; Repka, M. A., Development of an Antifungal Denture Adhesive Film for Oral Candidiasis Utilizing Hot Melt Extrusion Technology. *Expert Opin. Drug Deliv.* **2015,** *12* (1), 1-13.

64. Alhijjaj, M.; Bouman, J.; Wellner, N.; Belton, P.; Qi, S., Creating Drug Solubilization Compartments Via Phase Separation in Multicomponent Buccal Patches Prepared by Direct Hot Melt Extrusion–Injection Molding. *Mol. Pharmaceutics* **2015,** *12* (12), 4349-4362.

65. Brough, C.; Williams, R. O., Amorphous Solid Dispersions and Nano-Crystal Technologies for Poorly Water-Soluble Drug Delivery. *Int. J. Pharm.* **2013,** *453* (1), 157-166.

66. Huang, Y.; Dai, W.-G., Fundamental Aspects of Solid Dispersion Technology for Poorly Soluble Drugs. *Acta Pharm. Sin. B* **2014,** *4* (1), 18-25.

67. Chiou, W. L.; Riegelman, S., Pharmaceutical Applications of Solid Dispersion Systems. *J. Pharm. Sci.* **1971,** *60* (9), 1281-302.

68. Baird, J. A.; Taylor, L. S., Evaluation of Amorphous Solid Dispersion Properties Using Thermal Analysis Techniques. *Adv. Drug Deliv. Rev.* **2012,** *64* (5), 396-421.

69. Chiou, W. L.; Riegelman, S., Preparation and Dissolution Characteristics of Several Fast-Release Solid Dispersions of Griseofulvin. *J. Pharm. Sci.* **1969,** *58* (12), 1505-1510.

70. Konno, H.; Handa, T.; Alonzo, D. E.; Taylor, L. S., Effect of Polymer Type on the Dissolution Profile of Amorphous Solid Dispersions Containing Felodipine. *Eur. J. Pharm. Biopharm.* **2008,** *70* (2), 493-9.

71. Qian, F.; Huang, J.; Hussain, M. A., Drug–Polymer Solubility and Miscibility: Stability Consideration and Practical Challenges in Amorphous Solid Dispersion Development. *J. Pharm. Sci.* **2010,** *99* (7), 2941-2947.

72. Serajuddin, A. T., Solid Dispersion of Poorly Water-Soluble Drugs: Early Promises, Subsequent Problems, and Recent Breakthroughs. *J. Pharm. Sci.* **1999,** *88* (10), 1058-66.

73. Leuner, C.; Dressman, J., Improving Drug Solubility for Oral Delivery Using Solid Dispersions. *Eur. J. Pharm. Biopharm.* **2000,** *50* (1), 47-60.

74. Paudel, A.; Geppi, M.; Van den Mooter, G., Structural and Dynamic Properties of Amorphous Solid Dispersions: The Role of Solid-State Nuclear Magnetic Resonance Spectroscopy and Relaxometry. *J. Pharm. Sci.* **2014,** *103*, 2635–2662.

75. Vogt, F. G.; Clawson, J. S.; Strohmeier, M.; Pham, T. N.; Watson, S. A.; Edwards, A. J., New Approaches to the Characterization of Drug Candidates by Solid-State Nmr. In *Pharmaceutical Sciences Encyclopedia*, John Wiley & Sons, Inc.: 2010.

76. Higashi, K.; Yamamoto, K.; Pandey, M. K.; Mroue, K. H.; Moribe, K.; Yamamoto, K.; Ramamoorthy, A., Insights into Atomic-Level Interaction between Mefenamic Acid and Eudragit(®) Epo in a Supersaturated Solution by High-Resolution Magic-Angle Spinning Nmr Spectroscopy. *Mol. Pharmaceutics* **2014,** *11* (1), 351-357.

77. Konno, H.; Taylor, L. S., Influence of Different Polymers on the Crystallization Tendency of Molecularly Dispersed Amorphous Felodipine. *J. Pharm. Sci.* **2006,** *95* (12), 2692-705.

78. Janssens, S.; Van den Mooter, G., Review: Physical Chemistry of Solid Dispersions. *J. Pharm. Pharmacol.* **2009,** *61* (12), 1571-86.

79. Mullin, J. W., 5 - Nucleation. In *Crystallization (Fourth Edition)*, Mullin, J. W., Ed. Butterworth-Heinemann: Oxford, 2001; pp 181-215.

80. Carpentier, L.; Desprez, S.; Descamps, M., Crystallization and Glass Properties of Pentitols. *J. Therm. Anal. Calorim.* **2003,** *73* (2), 577-586.

81. Zhou, D.; Zhang, G. G. Z.; Law, D.; Grant, D. J. W.; Schmitt, E. A., Physical Stability of Amorphous Pharmaceuticals: Importance of Configurational Thermodynamic Quantities and Molecular Mobility. *J. Pharm. Sci.* **2002,** *91* (8), 1863-1872.

82. Bhugra, C.; Pikal, M. J., Role of Thermodynamic, Molecular, and Kinetic Factors in Crystallization from the Amorphous State. *J. Pharm. Sci.* **2008,** *97* (4), 1329-1349.

83. Jackson, K. A., On the Theory of Crystal Growth: The Fundamental Rate Equation. *J. Cryst. Growth* **1969,** *5* (1), 13-18.

84. Frenkel, J., Note on a Relation between the Speed of Crystallization and Viscosity. *Phisik. Zeit. Sowjetunion* **1932,** *1*, 498-510.

85. Newman, A., *Pharmaceutical Amorphous Solid Dispersions*. John Wiley & Sons, Incorporated: Somerset, UNITED STATES, 2015.

86. Cui, Y.; Frank, S. G., Isothermal Crystallization Kinetics of Lidocaine in Supersaturated Lidocaine/Polyacrylate Pressure Sensitive Adhesive Systems. *J. Pharm. Sci.* **2005,** *94* (9), 2039-48.

87. Söhnel, O.; Garside, J., *Precipitation: Basic Principles and Industrial Applications*. Butterworth-Heinemann: 1992.

88. Zeng, J.; Tikare, V.; Jacob, K. I., Numerical Study of a Drug Release Profile in the Transdermal Drug Delivery System. *Langmuir* **2006,** *22* (3), 1333-1340.

89. Marsac, P. J.; Konno, H.; Rumondor, A. C. F.; Taylor, L. S., Recrystallization of Nifedipine and Felodipine from Amorphous Molecular Level Solid Dispersions Containing Poly(Vinylpyrrolidone) and Sorbed Water. *Pharm. Res.* **2008,** *25* (3), 647-656.

90. Rumondor, A. C. F.; Jackson, M. J.; Taylor, L. S., Effects of Moisture on the Growth Rate of Felodipine Crystals in the Presence and Absence of Polymers. *Cryst. Growth Des.* **2010,** *10* (2), 747-753.

91. Chenevas-Paule, C.; Wolff, H.-M.; Ashton, M.; Schubert, M.; Dodou, K., Development of a Predictive Model for the Long-Term Stability Assessment of Drug-in-Adhesive Transdermal Films Using Polar Pressure-Sensitive Adhesives as Carrier/Matrix. *J. Pharm. Sci.* **2017,** *106* (5), 1293-1301.

92. Padermshoke, A.; Katsumoto, Y.; Sato, H.; Ekgasit, S.; Noda, I.; Ozaki, Y., Surface Melting and Crystallization Behavior of Polyhydroxyalkanoates Studied by Attenuated Total Reflection Infrared Spectroscopy. *Polymer* **2004,** *45* (19), 6547-6554.

93. Wu, J. X.; Yang, M.; Berg, F.; Pajander, J.; Rades, T.; Rantanen, J., Influence of Solvent Evaporation Rate and Formulation Factors on Solid Dispersion Physical Stability. *Eur. J. Pharm. Sci.* **2011,** *44* (5), 610-20.

94. Sun, Y.; Zhu, L.; Kearns, K. L.; Ediger, M. D.; Yu, L., Glasses Crystallize Rapidly at Free Surfaces by Growing Crystals Upward. *PNAS* **2011,** *108* (15), 5990-5995.

95. Zhu, L.; Wong, L.; Yu, L., Previous Article Next Article Table of Contents Surface-Enhanced Rrystallization of Amorphous Nifedipine. *Mol. Pharmaceutics* **2008,** *5* (6), 921-926.

96. Schmelzer, J.; Pascova, R.; Möller, J.; Gutzow, I., Surface-Induced Devitrification of Glasses: The Influence of Elastic Strains. *J. Non-Cryst. Solids* **1993,** *162* (1–2), 26-39.

97. Farrance, O. E.; Jones, R. A. L.; Hobbs, J. K., The Observation of Rapid Surface Growth During the Crystallization of Polyhydroxybutyrate. *Polymer* **2009,** *50* (15), 3730-3738.

98. Hasebe, M.; Musumeci, D.; Yu, L., Fast Surface Crystallization of Molecular Glasses: Creation of Depletion Zones by Surface Diffusion and Crystallization Flux. *J. Phys. Chem. B* **2015,** *119* (7), 3304-3311.

99. Z.Fakhraai; Forrest, J. A., Measuring the Surface Dynamics of Glassy Polymers. *Science* **2008,** *319* (5863), 600-604.

100. SF, S., Extraordinarily Stable Glassy Materials Prepared by Vapor Deposition. *Science* **2007,** *315*, 353-356.

101. RC, B.; H, W.; MJ, L.; JP, C., Nanometer-Resolved Interfacial Fluidity. *J. Am. Chem. Soc.* **2003,** *125*, 5176-5185.

102. Brian, C. W.; Yu, L., Surface Self-Diffusion of Organic Glasses. *J.Phys. Chem. A* **2013,** *117* (50), 13303-13309.

103. Yang, Z.; Nollenberger, K.; Albers, J.; Craig, D.; Qi, S., Molecular Indicators of Surface and Bulk Instability of Hot Melt Extruded Amorphous Solid Dispersions. *Pharm. Res.* **2015,** *32* (4), 1210-28.

104. Tian, Y.; Jones, D. S.; Andrews, G. P., An Investigation into the Role of Polymeric Carriers on Crystal Growth within Amorphous Solid Dispersion Systems. *Mol. Pharmaceutics* **2015,** *12* (4), 1180-92.

105. Kestur, U. S.; Ivanesivic, I.; Alonzo, D. E.; Taylor, L. S., Influence of Particle Size on the Crystallization Kinetics of Amorphous Felodipine Powders. *Powder Technol.* **2013,** *236*, 197-204.

106. Variankaval, N. E.; Jacob, K. I.; Dinh, S. M., Crystallization of Beta-Estradiol in an Acrylic Transdermal Drug Delivery System. *J. Biomed. Mater. Res.* **1999,** *44* (4), 397-406.

107. Variankaval, N. E.; Jacob, K. I.; Dinh, S. M., Polymorphism of 17-B Estradiol in a Transdermal Drug Delivery System. *J. Mater. Sci.:Mater. in Med.* **2002,** *13* (3), 271-280.

108. Hadgraft, J.; Lane, M. E., Drug Crystallization–Implications for Topical and Transdermal Delivery. *Expert Opin. Drug Delivery* **2016,** *13* (6), 817-830.

109. Latsch, S.; Selzer, T.; Fink, L.; Kreuter, J., Determination of the Physical State of Norethindrone Acetate Containing Transdermal Drug Delivery Systems by Isothermal Microcalorimetry, X-Ray Diffraction, and Optical Microscopy. *Eur. J. Pharm. Biopharm.* **2004,** *57* (2), 383-395.

110. Rumondor, A. C. F.; Taylor, L. S., Application of Partial Least-Squares (Pls) Modeling in Quantifying Drug Crystallinity in Amorphous Solid Dispersions. *Int. J. Pharm.* **2010,** *398* (1), 155-160.

111. Zidan, A. S.; Rahman, Z.; Sayeed, V.; Raw, A.; Yu, L.; Khan, M. A., Crystallinity Evaluation of Tacrolimus Solid Dispersions by Chemometric Analysis. *Int. J. Pharm.* **2012,** *423* (2), 341-350.

112. Netchacovitch, L.; Dumont, E.; Cailletaud, J.; Thiry, J.; De Bleye, C.; Sacré, P. Y.; Boiret, M.; Evrard, B.; Hubert, P.; Ziemons, E., Development of an Analytical Method for Crystalline Content Determination in Amorphous Solid Dispersions Produced by Hot-Melt Extrusion Using Transmission Raman Spectroscopy: A Feasibility Study. *Int. J. Pharm.* **2017,** *530* (1), 249-255.

113. Ermolina, I.; Darkwah, J.; Smith, G., Characterisation of Crystalline-Amorphous Blends of Sucrose with Terahertz-Pulsed Spectroscopy: The Development of a Prediction Technique for Estimating the Degree of Crystallinity with Partial Least Squares Regression. *AAPS PharmSciTech* **2014,** *15* (2), 253-260.

114. Tian, Y.; Jones, D. S.; Andrews, G. P., An Investigation into the Role of Polymeric Carriers on Crystal Growth within Amorphous Solid Dispersion Systems. *Mol. Pharmaceutics* **2015,** *12* (4), 1180-1192.

115. Sheokand, S.; Modi, S. R.; Bansal, A. K., Dynamic Vapor Sorption as a Tool for Characterization and Quantification of Amorphous Content in Predominantly Crystalline Materials. *J. Pharm. Sci.* **2014,** *103* (11), 3364-3376.

116. Punčochová, K.; Heng, J. Y. Y.; Beránek, J.; Štěpánek, F., Investigation of Drug–Polymer Interaction in Solid Dispersions by Vapour Sorption Methods. *Int. J. Pharm.* **2014,** *469* (1), 159-167.

117. Columbano, A.; Buckton, G.; Wikeley, P., A Study of the Crystallisation of Amorphous Salbutamol Sulphate Using Water Vapour Sorption and near Infrared Spectroscopy. *Int. J. Pharm.* **2002,** *237* (1), 171-178.

118. Kontny, M. J.; Zografi, G., Sorption of Water by Solids. *Drugs Pharm. Sci.* **1995,** *70*, 387-387.

119. Ahlneck, C.; Zografi, G., The Molecular Basis of Moisture Effects on the Physical and Chemical Stability of Drugs in the Solid State. *Int. J. Pharm.* **1990,** *62* (2), 87-95.

120. Li, W.; Buckton, G., Using Dvs-Nir to Assess the Water Sorption Behaviour and Stability of a Griseofulvin/Pvp K30 Solid Dispersion. *Int. J. Pharm.* **2015,** *495* (2), 999-1004.

121. Lewicki, P. P., Water Sorption Isotherms and Their Estimation in Food Model Mechanical Mixtures. *J. Food Process Eng.* **1997,** *32* (1), 47-68.

122. Hancock, B. C.; Zografi, G., Characteristics and Significance of the Amorphous State in Pharmaceutical Systems. *J. Pharm. Sci.* **1997,** *86* (1), 1-12.

123. Bragg, W. L., The Diffraction of Short Electromagnetic Waves by a Crystal. **1929**.

124. R., S., *X-Ray Powder Diffractometry*. Marcel Dekker: New York, 1995.

125. Byard, S. J.; Jackson, S. L.; Smail, A.; Bauer, M.; Apperley, D. C., Studies on the Crystallinity of a Pharmaceutical Development Drug Substance. *J. Pharm. Sci.* **2005,** *94* (6), 1321-1335.

126. Suryanarayanan, R.; Mitchell, A. G., Evaluation of Two Concepts of Crystallinity Using Calcium Gluceptate as a Model Compound. *Int. J. Pharm.* **1985,** *24* (1), 1-17.

127. Albarahmieh, E. a.; Qi, S.; Craig, D. Q. M., Hot Melt Extruded Transdermal Films Based on Amorphous Solid Dispersions in Eudragit Rs Po: The Inclusion of Hydrophilic Additives to Develop Moisture-Activated Release Systems. *Int. J. Pharm.* **2016,** *514* (1), 270-281.

128. Gumaste, S. G.; Gupta, S. S.; Serajuddin, A. T. M., Investigation of Polymer-Surfactant and Polymer-Drug-Surfactant Miscibility for Solid Dispersion. *AAPS J.* **2016,** *18* (5), 1131-1143.

129. Umeki, N.; Sato, T.; Harada, M.; Takeda, J.; Saito, S.; Iwao, Y.; Itai, S., Preparation and Evaluation of Biodegradable Films Containing the Potent Osteogenic Compound Bfb0261 for Localized Delivery. *Int. J. Pharm.* **2011,** *404* (1), 10-18.

130. Ohta, K. M.; Fuji, M.; Takei, T.; Chikazawa, M., Development of a Simple Method for the Preparation of a Silica Gel Based Controlled Delivery System with a High Drug Content. *Eur. J. Pharm. Sci.* **2005,** *26* (1), 87-96.

131. Shah, B.; Kakumanu, V. K.; Bansal, A. K., Analytical Techniques for Quantification of Amorphous/Crystalline Phases in Pharmaceutical Solids. *J. Pharm. Sci.* **2006,** *95* (8), 1641-65.

132. Brittain, H. G.; Bogdanowich, S. J.; Bugay, D. E.; DeVincentis, J.; Lewen, G.; Newman, A. W., Physical Characterization of Pharmaceutical Solids. *Pharm. Res.* **1991,** *8* (8), 963-73.

133. Padilla, A. M.; Chou, S. G.; Luthra, S.; Pikal, M. J., The Study of Amorphous Phase Separation in a Model Polymer Phase-Separating System Using Raman Microscopy and a Low-Temperature Stage: Effect of Cooling Rate and Nucleation Temperature. *J. Pharm. Sci.* **2011,** *100* (4), 1362-1376.

134. Newman, A.; Engers, D.; Bates, S.; Ivanisevic, I.; Kelly, R. C.; Zografi, G., Characterization of Amorphous Api:Polymer Mixtures Using X-Ray Powder Diffraction. *J. Pharm. Sci.* **2008,** *97* (11), 4840-56.

135. Davis, T.; Johnson, M.; Billinge, S. J. L., Toward Phase Quantification at the Nanoscale Using the Total Scattering Pair Distribution Function (Tspdf) Method: Recrystallization of Cryomilled Sulfamerazine. *Cryst. Growth Des.* **2013,** *13* (10), 4239-4244.

136. Bates, S.; Kelly, R. C.; Ivanisevic, I.; Schields, P.; Zografi, G.; Newman, A. W., Assessment of Defects and Amorphous Structure Produced in Raffinose Pentahydrate Upon Dehydration. *J. Pharm. Sci.* **2007,** *96* (5), 1418-33.

137. Chieng, N.; Trnka, H.; Boetker, J.; Pikal, M.; Rantanen, J.; Grohganz, H., Detecting Phase Separation of Freeze-Dried Binary Amorphous Systems Using Pair-Wise Distribution Function and Multivariate Data Analysis. *Int. J. Pharm.* **2013,** *454* (1), 167-73.

138. Moore, M. D.; Shi, Z.; Wildfong, P. L. D., Structural Interpretation in Composite Systems Using Powder X-Ray Diffraction: Applications of Error Propagation to the Pair Distribution Function. *Pharm. Res.* **2010,** *27* (12), 2624-2632.

139. Sogias, I. A.; Williams, A. C.; Khutoryanskiy, V. V., Chitosan-Based Mucoadhesive Tablets for Oral Delivery of Ibuprofen. *Int. J. Pharm.* **2012,** *436* (1-2), 602-610.

140. Takahashi, H.; Chen, R.; Okamoto, H.; Danjo, K., Acetaminophen Particle Design Using Chitosan and a Spray-Drying Technique. *Chem. Pharm. Bull.* **2005,** *53* (1), 37-41.

141. Feng, X.; Ye, X.; Park, J. B.; Lu, W.; Morott, J.; Beissner, B.; Lian, Z. J.; Pinto, E.; Bi, V.; Porter, S.; Durig, T.; Majumdar, S.; Repka, M. A., Evaluation of the Recrystallization Kinetics of Hot-Melt Extruded Polymeric Solid Dispersions Using an Improved Avrami Equation. *Drug Dev. Ind. Pharm.* **2015,** *41* (9), 1479-1487.

142. Yang, J.; Grey, K.; Doney, J., An Improved Kinetics Approach to Describe the Physical Stability of Amorphous Solid Dispersions. *Int. J. Pharm.* **2010,** *384* (1), 24-31.

143. Hsu, H.-Y.; Harris, M. T.; Toth, S.; Simpson, G. J., Drop Printing of Pharmaceuticals: Effect of Molecular Weight on Peg Coated-Naproxen/Peg 3350 Solid Dispersions. *AIChE J.* **2015,** *61* (12), 4502-4508.

144. Savolainen, M.; Jouppila, K.; Pajamo, O.; Christiansen, L.; Strachan, C.; Karjalainen, M.; Rantanen, J., Determination of Amorphous Content in the Pharmaceutical Process Environment. *J. Pharm. Pharmacol.* **2007,** *59* (2), 161-170.

145. Pan, X.; Julian, T.; Augsburger, L., Quantitative Measurement of Indomethacin Crystallinity in Indomethacin-Silica Gel Binary System Using Differential Scanning Calorimetry and X-Ray Powder Diffractometry. *AAPS PharmSciTech* **2006,** *7* (1), E72-E78.

146. Otsuka, M.; Kato, F.; Matsuda, Y., Comparative Evaluation of the Degree of Indomethacin Crystallinity by Chemoinfometrical Fourie-Transformed near-Infrared Spectroscopy and Conventional Powder X-Ray Diffractiometry. *AAPS PharmSciTech* **2000,** *2* (1), 80-87.

147. Shi, Z.; Anderson, C. A., Scattering Orthogonalization of near-Infrared Spectra for Analysis of Pharmaceutical Tablets. *Anal. Chem.* **2009,** *81* (4), 1389-1396.

148. Kirsch, J. D.; Drennen, J. K., Nondestructive Tablet Hardness Testing by near-Infrared Spectroscopy: A New and Robust Spectral Best-Fit Algorithm. *J. Pharm. Biomed. Anal.* **1999,** *19* (3), 351-362.

149. Blanco, M.; Alcalá, M.; González, J. M.; Torras, E., A Process Analytical Technology Approach Based on near Infrared Spectroscopy: Tablet Hardness, Content Uniformity, and Dissolution Test Measurements of Intact Tablets. *J. Pharm. Sci.* **2006,** *95* (10), 2137-2144.

150. Huang, M.; Kim, M. S.; Chao, K.; Qin, J.; Mo, C.; Esquerre, C.; Delwiche, S.; Zhu, Q., Penetration Depth Measurement of near-Infrared Hyperspectral Imaging Light for Milk Powder. *Sensors (Basel, Switzerland)* **2016,** *16* (4), 441.

151. Shi, Z.; Anderson, C. A., Application of Monte Carlo Simulation-Based Photon Migration for Enhanced Understanding of near-Infrared (Nir) Diffuse Reflectance. Part I: Depth of Penetration in Pharmaceutical Materials. *J. Pharm. Sci.* **2010,** *99* (5), 2399-2412.

152. Wahl, P. R.; Treffer, D.; Mohr, S.; Roblegg, E.; Koscher, G.; Khinast, J. G., Inline Monitoring and a Pat Strategy for Pharmaceutical Hot Melt Extrusion. *Int. J. Pharm.* **2013,** *455* (1), 159-168.

153. Sakamoto, T.; Fujimaki, Y.; Takada, Y.; Aida, K.; Terahara, T.; Kawanishi, T.; Hiyama, Y., Non-Destructive Analysis of Tulobuterol Crystal Reservoir-Type Transdermal Tapes Using near Infrared Spectroscopy and Imaging. *J. Pharm. Biomed. Anal.* **2013,** *74*, 14-21.

154. Févotte, G., In Situ Raman Spectroscopy for in-Line Control of Pharmaceutical Crystallization and Solids Elaboration Processes: A Review. *Chem. Eng. Res. Des.* **2007,** *85* (7), 906-920.

155. Skoog, D. A.; Holler, F. J.; Crouch, S. R., *Principles of Instrumental Analysis*. Cengage learning: 2017.

156. Willard, H. H.; Merritt Jr, L. L.; Dean, J. A.; Settle Jr, F. A., Instrumental Methods of Analysis. **1988**.

157. Vigh, T.; Drávavölgyi, G.; Sóti, P. L.; Pataki, H.; Igricz, T.; Wagner, I.; Vajna, B.; Madarász, J.; Marosi, G.; Nagy, Z. K., Predicting Final Product Properties of Melt Extruded Solid Dispersions from Process Parameters Using Raman Spectrometry. *J. Pharm. Biomed. Anal.* **2014,** *98*, 166-177.

158. Nakamoto, K.; Urasaki, T.; Hondo, S.; Murahashi, N.; Yonemochi, E.; Terada, K., Evaluation of the Crystalline and Amorphous States of Drug Products by Nanothermal Analysis and Raman Imaging. *J. Pharm. Biomed. Anal.* **2013,** *75*, 105-111.

159. Lust, A.; Strachan, C. J.; Veski, P.; Aaltonen, J.; Heinämäki, J.; Yliruusi, J.; Kogermann, K., Amorphous Solid Dispersions of Piroxicam and Soluplus®: Qualitative and Quantitative Analysis of Piroxicam Recrystallization During Storage. *Int. J. Pharm.* **2015,** *486* (1-2), 306-314.

160. Tian, Y.; Jones, D. S.; Andrews, G. P., An Investigation into the Role of Polymeric Carriers on Crystal Growth within Amorphous Solid Dispersion Systems. *Mol. Pharm.* **2015,** *12* (4), 1180-1192.

161. Tumuluri, V. S.; Kemper, M. S.; Lewis, I. R.; Prodduturi, S.; Majumdar, S.; Avery, B. A.; Repka, M. A., Off-Line and on-Line Measurements of Drug-Loaded Hot-Melt Extruded Films Using Raman Spectroscopy. *Int. J. Pharm.* **2008,** *357* (1-2), 77-84.

162. Trenfield, S. J.; Goyanes, A.; Telford, R.; Wilsdon, D.; Rowland, M.; Gaisford, S.; Basit, A. W., 3d Printed Drug Products: Non-Destructive Dose Verification Using a Rapid Point-and-Shoot Approach. *Int. J. Pharm.* **2018,** *549* (1), 283-292.

163. Blanco, M.; Villar, A., Development and Validation of a Method for the Polymorphic Analysis of Pharmaceutical Preparations Using near Infrared Spectroscopy. *J. Pharm. Sci.* **2003,** *92* (4), 823-30.

164. Kestur, U. S.; Wanapun, D.; Toth, S. J.; Wegiel, L. A.; Simpson, G. J.; Taylor, L. S., Nonlinear Optical Imaging for Sensitive Detection of Crystals in Bulk Amorphous Powders. *J. Pharm. Sci.* **2012,** *101* (11), 4201-4213.

165. Schmitt, P. D.; Trasi, N. S.; Taylor, L. S.; Simpson, G. J., Finding the Needle in the Haystack: Characterization of Trace Crystallinity in a Commercial Formulation of Paclitaxel Protein-Bound Particles by Raman Spectroscopy Enabled by Second Harmonic Generation Microscopy. *Mol. Pharm.* **2015,** *12* (7), 2378-2383.

166. Krause, S.; Iskandar, M., Phase Separation in Styrene-A-Methyl Styrene Block Copolymers. In *Polymer Alloys: Blends, Blocks, Grafts, and Interpenetrating Networks*, Klempner, D.; Frisch, K. C., Eds. Springer US: Boston, MA, 1977; pp 231-243.

167. Barnes, T. J.; Kempson, I. M.; Prestidge, C. A., Surface Analysis for Compositional, Chemical and Structural Imaging in Pharmaceutics with Mass Spectrometry: A Tof-Sims Perspective. *Int. J. Pharm.* **2011,** *417* (1), 61-69.

168. Wanapun, D.; Kestur, U. S.; Kissick, D. J.; Simpson, G. J.; Taylor, L. S., Selective Detection and Quantitation of Organic Molecule Crystallization by Second Harmonic Generation Microscopy. *Anal. Chem.* **2010,** *82* (13), 5425-5432.

169. Zhang, W.; Parniak, M. A.; Sarafianos, S. G.; Cost, M. R.; Rohan, L. C., Development of a Vaginal Delivery Film Containing Efda, a Novel Anti-Hiv Nucleoside Reverse Transcriptase Inhibitor. *Int. J. Pharm.* **2014,** *461* (1-2), 203-13.

170. Keen, J. M.; Martin, C.; Machado, A.; Sandhu, H.; McGinity, J. W.; DiNunzio, J. C., Investigation of Process Temperature and Screw Speed on Properties of a Pharmaceutical Solid Dispersion Using Corotating and Counter‐Rotating Twin‐Screw Extruders. *J. Pharm. Pharmacol.* **2014,** *66* (2), 204-217.

171. Banerjee, S.; Chattopadhyay, P.; Ghosh, A.; Bhattacharya, S. S.; Kundu, A.; Veer, V., Accelerated Stability Testing of a Transdermal Patch Composed of Eserine and Pralidoxime Chloride for Prophylaxis against (±)-Anatoxin a Poisoning. *J. Food Drug Anal.* **2014,** *22* (2), 264-270.

172. Guideline, I. H. T., Stability Testing of New Drug Substances and Products. *Q1A (R2), current step* **2003,** *4*, 1-24.

173. Jain, P.; Banga, A. K., Inhibition of Crystallization in Drug-in-Adhesive-Type Transdermal Patches. *Int. J. Pharm.* **2010,** *394* (1), 68-74.

174. Imani, M.; Lahooti-Fard, F.; Taghizadeh, S. M.; Takrousta, M., Effect of Adhesive Layer Thickness and Drug Loading on Estradiol Crystallization in a Transdermal Drug Delivery System. *AAPS PharmSciTech* **2010,** *11* (3), 1268-1275.

175. Latsch, S.; Selzer, T.; Fink, L.; Kreuter, J., Crystallisation of Estradiol Containing Tdds Determined by Isothermal Microcalorimetry, X-Ray Diffraction, and Optical Microscopy. *Eur. J. Pharm. Biopharm.* **2003,** *56* (1), 43-52.

176. Gaisford, S.; Verma, A.; Saunders, M.; Royall, P. G., Monitoring Crystallisation of Drugs from Fast-Dissolving Oral Films with Isothermal Calorimetry. *Int. J. Pharm.* **2009,** *380* (1), 105-111.

177. Ueda, C. T.; Shah, V. P.; Derdzinski, K.; Ewing, G.; Flynn, G.; Maibach, H.; Marques, M.; Rytting, H.; Shaw, S.; Thakker, K. In *Topical and Transdermal Drug Products*, Pharmacopeial Forum, 2009; pp 750-764.

178. Cogdill, R. P.; Anderson, C. A.; Delgado-Lopez, M.; Molseed, D.; Chisholm, R.; Bolton, R.; Herkert, T.; Afnán, A. M.; Drennen, J. K., Process Analytical Technology Case Study Part I: Feasibility Studies for Quantitative near-Infrared Method Development. *AAPS PharmSciTech* **2005,** *6* (2), E262-E272.

179. Hubert, P.; Nguyen-Huu, J. J.; Boulanger, B.; Chapuzet, E.; Chiap, P.; Cohen, N.; Compagnon, P. A.; Dewe, W.; Feinberg, M.; Lallier, M.; Laurentie, M.; Mercier, N.; Muzard, G.; Nivet, C.; Valat, L.; Rozet, E., Harmonization of Strategies for the Validation of Quantitative Analytical Procedures. A Sfstp Proposal--Part Ii. *J. Pharm. Biomed. Anal.* **2007,** *45* (1), 70-81.

180. Liltorp, K.; Larsen, T. G.; Willumsen, B.; Holm, R., Solid State Compatibility Studies with Tablet Excipients Using Non Thermal Methods. *J. Pharm. Biomed. Anal.* **2011,** *55* (3), 424-428.

181. Wolff, H. M.; Irsan; Dodou, K., Investigations on the Viscoelastic Performance of Pressure Sensitive Adhesives in Drug-in-Adhesive Type Transdermal Films. *Pharm. Res.* **2014,** *31* (8), 2186-202.

182. Hildebrand, J. H.; Prausnitz, J. M.; Scott, R. L., *Regular and Related Solutions: The Solubility of Gases, Liquids, and Solids*. Van Nostrand Reinhold Co.: 1970.

183. Namur, J.; Wassef, M.; Pelage, J. P.; Lewis, A.; Manfait, M.; Laurent, A., Infrared Microspectroscopy Analysis of Ibuprofen Release from Drug Eluting Beads in Uterine Tissue. *J. Control. Release* **2009,** *135* (3), 198-202.

184. Kitak, T.; Dumičić, A.; Planinšek, O.; Šibanc, R.; Srčič, S., Determination of Solubility Parameters of Ibuprofen and Ibuprofen Lysinate. *Molecules* **2015,** *20* (12), 19777.

185. Wolff, H.-M.; Irsan; Dodou, K., Investigations on the Viscoelastic Performance of Pressure Sensitive Adhesives in Drug-in-Adhesive Type Transdermal Films. *Pharm. Res.* **2014,** *31* (8), 2186-2202.

186. Demirel, B.; Yaraş, A.; Elçiçek, H., Crystallization Behavior of Pet Materials. *Balıkesir Üniversitesi Fen Bilimleri Enstitüsü Dergisi* **2016,** *13* (1), 26-35.

187. Everall, N.; Priestnall, I. A. N.; Dallin, P.; Andrews, J.; Lewis, I. A. N.; Davis, K.; Owen, H.; George, M. W., Measurement of Spatial Resolution and Sensitivity in Transmission and Backscattering Raman Spectroscopy of Opaque Samples: Impact on Pharmaceutical Quality Control and Raman Tomography. *Appl. Spectrosc.* **2010,** *64* (5), 476-484.

188. Matousek, P.; Clark, I.; Draper, E.; Morris, M.; Goodship, A.; Everall, N.; Towrie, M.; Finney, W.; Parker, A., Subsurface Probing in Diffusely Scattering Media Using Spatially Offset Raman Spectroscopy. *Appl. Spectrosc.* **2005,** *59* (4), 393-400.

189. Goicoechea, H. C.; Olivieri, A. C., Enhanced Synchronous Spectrofluorometric Determination of Tetracycline in Blood Serum by Chemometric Analysis. Comparison of Partial Least-Squares and Hybrid Linear Analysis Calibrations. *Anal. Chem.* **1999,** *71* (19), 4361-4368.

190. Vessman, J.; Stefan, R. I.; Van Staden, J. F.; Danzer, K.; Lindner, W.; Burns, D. T.; Fajgelj, A.; Müller, H., Selectivity in Analytical Chemistry (Iupac Recommendations 2001). *Pure Appl. Chem.* **2001,** *73* (8), 1381-1386.

191. Short, S. M.; Cogdill, R. P.; Anderson, C. A., Determination of Figures of Merit for near-Infrared and Raman Spectrometry by Net Analyte Signal Analysis for a 4-Component Solid Dosage System. *AAPS PharmSciTech* **2007,** *8* (4), 109-119.

192. Brown, C. D.; Ridder, T. D., Framework for Multivariate Selectivity Analysis, Part I: Theoretical and Practical Merits. *Appl. Spectrosc.* **2005,** *59* (6), 787-803.

193. NCCLS, Interference Testing in Clinical Chemistry. *NCCLS document EP07-A* **2002**.

194. Guideline, I. H. T. In *Validation of Analytical Procedures: Text and Methodology Q2 (R1)*, International Conference on Harmonization, Geneva, Switzerland, 2005; pp 11-12.

195. Feinberg, M., Validation of Analytical Methods Based on Accuracy Profiles. *J. Chromatogr. A* **2007,** *1158* (1-2), 174-83.

196. Long, G. L.; Winefordner, J. D., Limit of Detection a Closer Look at the Iupac Definition. *Anal. Chem.* **1983,** *55* (07), 712A-724A.

197. Faber, K.; Kowalski, B. R., Prediction Error in Least Squares Regression: Further Critique on the Deviation Used in the Unscrambler. *Chemom. Intell. Lab. Syst.* **1996,** *34* (2), 283-292.

198. Fearn, T., Comparing Standard Deviations (Continued). *NIR news* **2009,** *20* (7), 24-25.

199. Hubert, P.; Nguyen-Huu, J. J.; Boulanger, B.; Chapuzet, E.; Chiap, P.; Cohen, N.; Compagnon, P. A.; Dewe, W.; Feinberg, M.; Lallier, M.; Laurentie, M.; Mercier, N.; Muzard, G.; Nivet, C.; Valat, L., Validation of Quantitative Analytical Procedure, Harmonization of Approaches. *S.T.P. Pharma Pratiques* **2003,** *13* (3), 101-138.

200. Mee, R. W., B-Expectation and B-Content Tolerance Limits for Balanced One-Way Anova Random Model. *Technometrics* **1984,** *26* (3), 251-254.

201. Feinberg, M.; Boulanger, B.; Dewé, W.; Hubert, P., New Advances in Method Validation and Measurement Uncertainty Aimed at Improving the Quality of Chemical Data. *Anal. Bioanal. Chem.* **2004,** *380* (3), 502-514.

202. Dobretsov, G. E.; Syrejschikova, T. I.; Smolina, N. V., On Mechanisms of Fluorescence Quenching by Water. *Biophysics* **2014,** *59* (2), 183-188.

203. Farias, M.; Carneiro, R., Simultaneous Quantification of Three Polymorphic Forms of Carbamazepine in the Presence of Excipients Using Raman Spectroscopy. *Molecules (Basel, Switzerland)* **2014,** *19* (9), 14128-14138.

204. Sasic, S.; Ekins, S., *Pharmaceutical Applications of Raman Spectroscopy*. Wiley: 2008.

205. Moser, K.; Kriwet, K.; Naik, A.; Kalia, Y. N.; Guy, R. H., Passive Skin Penetration Enhancement and Its Quantification in Vitro. *Eur. J. Pharm. Biopharm.* **2001,** *52* (2), 103-12.

206. Dudognon, E.; Danede, F.; Descamps, M.; Correia, N. T., Evidence for a New Crystalline Phase of Racemic Ibuprofen. *Pharm. Res.* **2008,** *25* (12), 2853-8.

207. Marsac, P. J.; Konno, H.; Taylor, L. S., A Comparison of the Physical Stability of Amorphous Felodipine and Nifedipine Systems. *Pharm. Res.* **2006,** *23* (10), 2306-16.

208. Prudic, A.; Ji, Y.; Luebbert, C.; Sadowski, G., Influence of Humidity on the Phase Behavior of Api/Polymer Formulations. *Eur. J. Pharm. Biopharm.* **2015,** *94*, 352-362.

209. Crowley, K. J.; Zografi, G., Water Vapor Absorption into Amorphous Hydrophobic Drug/Poly(Vinylpyrrolidone) Dispersions. *J. Pharm. Sci.* **2002,** *91* (10), 2150-2165.

210. Chenevas-Paule, C.; Wolff, H. M.; Ashton, M.; Schubert, M.; Dodou, K., Development of a Predictive Model for the Long-Term Stability Assessment of Drug-in-Adhesive Transdermal Films Using Polar Pressure-Sensitive Adhesives as Carrier/Matrix. *J. Pharm. Sci.* **2017,** *106* (5), 1293-1301.

211. Ulrich, J.; Strege, C., Some Aspects of the Importance of Metastable Zone Width and Nucleation in Industrial Crystallizers. *J. Cryst. Growth* **2002,** *237-239*, 2130-2135.

212. Tung, H.-H., Industrial Perspectives of Parmaceutical Crystallization. *Org. Process Res. Dev.* **2013,** *17* (3), 445-454.